

Master`s Agreement

Faculty	IV - Fakultet for ingeniørvitenskap
Institute	Institutt for energi- og prosessteknikk
Programme code	MTPROD
Course code	194_TEP4905_1

Personal information

Family name, first name	Paulsen, Valdemar Emil Sørli
Date of birth	14.07.1995
Email address	vepaulse@stud.ntnu.no

The Master`s thesis

Starting date	03.09.2019
Submission deadline	28.01.2020
Thesis working title	Student
Thematic description	<p>Deposition of silica particles in turbulent superheated steam: 1. Define particle size distribution, where assumptions are based on previous work on the kinetics of amorphous silica generation in vapor and likely dominant mechanisms. 2. Theoretically evaluate the effect of various factors such as temperature gradient, velocity gradient, as well as particle size, shape and mean density in view of particle agglomeration and deposition. 3. Evaluate ANSYS Fluent / OpenFOAM models to calculate depositional rates for particles of varying sizes onto a surface. 4. Calculate deposition rates based on previous points and compare results from different models for overlapping particle sizes. 5. Evaluate the strengths and weaknesses of utilized models for calculating deposition rates in geothermal supercritical and superheated steam. 6. Provide suggestions for further work. 7. Write a scientific paper on the achievements of the study.</p>

Supervision and co-authors

Supervisor	Erling Næss
Any co-supervisors	Silje Bordvik
Any co-authors	

Preface

This paper is written on behalf of a joint project conducted by the department of Energy and Process engineering for the geothermal deep drilling project on Iceland, IDDP. Much of the work involved in this paper is therefore the result of discussions with the Author and PhD candidate Silje Bordvik. The author thanks her for her continual encouragement and help in grasping much of the theory behind the topics, and wishes her good luck with her thesis. The author also thanks Supervisor Erling Næss. His constant understanding and patience has been of great comfort through the entire study, and his dedication to his master-students is highly appreciated.

Abstrakt

Geotermisk kraftutvinnelse fra reservoarer vel under konvensjonelle boredybder undersøkes på Island. Problemer med rørtettelse og beleggdannelse fra ”silika kolloider” (Silisiumdioksid) ble oppdaget under det første boreprosjektet. Det er dermed ønskelig med en undersøkelse i formasjon og avsettelse av silika-partikler.

I denne avhandlingen presenteres en evaluering av hvordan silika kolloider formeres og de underbyggende mekanismene for silika utskillelse og agglomerering i geotermisk damp. På bakgrunn av denne evalueringen, samt data fra det første boreprosjektet, blir det foreslått en størrelsesfordeling for den agglomererte silika.

Avsettelse av silika partikler med relevante mekanismer er undersøkt for strømning av overopphetet damp. Under forholdene for geotermisk damp er det funnet at de viktigste faktorene for avsettelse av silika er diffusjon fra turbulens, termodiffusjon fra temperaturgradienter og molekylær ”Brownisk” diffusjon. Faktorer som påvirker heftsansynligheten til silika-partikler på veggen er også presentert. Men på bakgrunn av manglende validering av faktorenes innflytelse, og med hensyn til eksperimentelle resultater fra Fridriksson et al. (2015), konkluderes det med en uniform heftsansynlighet i nåværende undersøkelse.

Simuleringer av silika-partiklers avsettelse var gjennomført med et verktøy for numerisk fluiddynamikk, ANSYS FLUENT. Dette verktøyet var valgt etter evaluering av avhandlinger fra Chauhan (2019) og Tandberg (2017). Simuleringen var løst med bruk av RANS-metoden. De høye Reynolds-tallene til stede i geotermiske brønner setter krav på en turbulensmodell for å simulere turbulens nært brønnveggen. Etter anbefaling av ANSYS (2014) ble modellene $\kappa - \omega$ SST og RSM valgt for evaluering. Partiklene var simulert med en diskret-fase modell (DPM) inkludert i FLUENT. ”Brownisk” kraft ble introdusert med bruk av en brukerdefinert function (UDF) som en utvidelse av DPM. Avsettelsene ble lagret i vegg-cellene i en brukerdefinert minne-lokasjon (UDML) som teller antall partikler avsatt i hver celle. Denne utvidelse var også introdusert med en UDF.

Partikkel-avsettelse ble først simulert med parametere lik de i avhandlingen av Tandberg (2017), og resultatene ble sammenliknet med empiriske formler av Papavergos and Hedley (1984) og Ahmadi (1994) for å evaluere turbulensmodellene. Resultatene var manglende med tanke på valg av turbulensmodell.

Flere simuleringer ble utført for høyere hastigheter og for partikler med egenskaper til silika-kolloider, før en komplett simulering av silika-avsettelse i overopphetet damp-strøm ble utført. Geotermiske forhold vises å minske molekylær diffusjon på grunn av høyt trykk, noe som leder til høyere avhengighet av turbulent diffusjon. Resultatene avslører manglende robusthet for begge turbulensmodellene når det kommer til å håndtere veldig høye Reynolds-tall, som de man finner i geotermiske brønner. DPM-metoden risikerer også å undervurdere avsettelse av større partikler i strøm motsatt tyngdekraft.

Det anbefales å modifisere RSM turbulensmodellen for nær-vegg hastighetssvingninger, som foreslått av Tian and Ahmadi (2006). Målet med modifikasjonen er å forbedre nøyaktigheten av turbulente svingninger nær veggen, med mål å forbedre diffusjonsdrevet partikkel-avsettelse.

Abstract

Geothermal power extraction from reservoirs well below conventional drilling depths are being investigated on Iceland. The problem of pipe fouling of colloidal silica particles (Silicon dioxide) have been detected from the first drilling project. An investigation in the formation and deposition of silica particles is therefore desirable.

This study presents an evaluation of the formation of colloidal silica and the underlying mechanisms for precipitation and agglomeration of silica in geothermal steam. Based on this evaluation and data from the first drilling project, a suggested size distribution for agglomerated silica is presented.

Deposition of silica particles with all relevant mechanisms is investigated for a superheated steam flow. Based on the conditions of a geothermal well and the properties of geothermal steam, the most important factors for deposition of silica particles are found to be diffusion by turbulence, thermophoresis by temperature gradients and molecular "Brownian" diffusion. Factors influencing the sticking probability of silica particles onto the wall were also presented. However, lack of sufficient validation of the factors importance, along with the fouling results from experiments performed by Fridriksson et al. (2015) led to a conclusion of uniform sticking probability for the current study.

Simulations of silica particle deposition was conducted with the use of the commercial CFD tool ANSYS FLUENT. This tool was selected based on an evaluation between papers from Chauhan (2019) and Tandberg (2017). The flow was solved using the Reynolds averaged Navier-Stokes equation method (RANS). The high Reynolds numbers present in geothermal wells require a turbulence model for predicting turbulence close to pipe walls. By recommendations of ANSYS (2014), the models $\kappa - \omega$ SST and RSM were selected and evaluated. The particles were simulated with the discrete phase model (DPM) included in FLUENT. The brownian force mechanism was introduced using a user-defined function (UDF) which extended the options of DPM. The depositions were stored at the wall-cells in a user-defined-memory-location (UDML) that holds the number of deposited particles in each cell. This extension was also introduced with a UDF.

Particle deposition was first simulated with parameters in accordance to the thesis of Tandberg (2017), and the results were compared to empirical formulae of Papavergos and Hedley (1984) and Ahmadi (1994) in order to evaluate the turbulence models. The results were inconclusive as far as choice of turbulence model was concerned.

Further simulations were performed for higher velocities and for particles with colloidal silica properties, before a full simulation of silica deposition in hot gas pipe flow was conducted. Geothermal conditions are shown to decrease molecular diffusion due to the higher pressure, leading to higher dependency upon turbulent diffusion. The results reveal a lack in robustness for both turbulence models to handle very high Reynolds numbers, like those that are to be found in geothermal wells. The DPM method also shows risks of underestimating deposition of larger particles in gravitational flows.

It is suggested that the RSM turbulence model should be modified for close wall velocity fluctuations as suggested by Tian and Ahmadi (2006). The goal of the modification is to enhance the accuracy of turbulence fluctuations close to wall, and so enhance diffusion-driven particle deposition.

Contents

1	Introduction	1
2	Theory: Silica precipitation & deposition	3
2.1	Colloidal silica precipitation	3
2.1.1	Process of colloidal silica formation	4
2.2	Silica deposition effects	10
2.2.1	Describing deposition rates	10
2.2.2	Turbulent- & molecular diffusion	13
2.2.3	Thermophoresis	19
2.2.4	Lift	26
2.2.5	Particle deposition description	26
2.2.6	Deposition predictions	28
2.2.7	Electrostatic forces	28
2.2.8	Empirical formulae	29
3	Theory: Flow simulation & Particle tracking	31
3.1	Comparison of software	31
3.1.1	OpenFOAM	31
3.1.2	ANSYS Fluent	31
3.2	Numerical turbulence modeling	32
3.3	Turbulence models & wall functions	32
3.3.1	RANS-equation solution method	34
3.4	Particle deposition modeling	35
3.4.1	Attachment and re-suspension	35
3.4.2	Chauhan	36
3.4.3	Tandberg	39
3.5	Model comparison	40
3.6	Discrete Phase Model	41
3.6.1	Stochastic particle tracking	43
4	Computational alternatives	44
4.1	Meshing & wall cell resolution	44
4.2	User defined functions and initial conditions	45
5	Results & Comparisons	46
5.1	Dimensionless wall distance	46
5.2	Setup	46
5.3	Simulation parameters	50
5.4	Simulation results	52
5.4.1	Long pipe	52
5.4.2	Elongated pipe	59

5.4.3	Gravitational flow	61
5.4.4	Geothermal pipe flow	62
5.4.5	Bend	64
6	Discussion & comparison of results.	66
6.1	Comparison to empirical formulae	66
6.1.1	Turbulence modeling	66
6.1.2	Particle tracking	67
6.1.3	Reynolds number	68
6.1.4	Nanoparticle deposition development	68
6.2	Comparison to experimental results of geothermal wells	69
6.3	Thermophoresis	70
6.3.1	Deceleration of pipe bends	71
6.4	Aging and scaling	71
7	Conclusion & further work	73
7.1	Conclusion	73
7.2	Further work	74
	Bibliography	76
.1	Additional simulation results	81
.1.1	Velocity profile	81
.1.2	Dim. less velocity profile	83
.1.3	Deposition rate comparisons	85
.2	Matlab code	91
.3	C code / FLUENT macros	99

List of Figures

1.1	Illustration of the geothermal wells	1
2.1	Geothermal steam extraction, sketch	3
2.2	Silica solubility diagram	5
2.3	Computed solubility of silica and amorphous silica at saturated water pressure	5
2.4	Phase diagram of H ₂ O	6
2.5	Predicted solubility of silica compared to experimental data, plotted by Bahadori and Vuthaluru (2009)	7
2.6	Nucleation reaction	8
2.7	La Mer diagram	8
2.8	Silica agglomeration development	9
2.9	Particle deposition rate by V_{dep}^+ vs τ^+	12
2.10	Mass transfer in the turbulent boundary layer.	13
2.11	Colloidal particle concentration along wall.	17
2.12	Surface roughness w/ sublayer	18
2.13	Deposition rate influenced by surface roughness, by Guha (2008).	19
2.14	Surface roughness w/ deposition	19
2.15	Kerosene lamp displaying effects of thermophoresis.	20
2.16	Thermophoretic efficiency	22
2.17	Thermal diffusion on deposition rates	23
2.18	Thermophoretic gradient	24
2.19	Amorphous silica conductivity	24
2.20	Thermophoretic force	25
2.21	A particle in a shear flow experiences shear lift (Saffman, 1964)	26
2.22	200 nm particle concentration distribution close to wall. empirical data from Zheng and Silber-Li (2009).	27
2.23	Mass flux across pipe flow	27
2.24	Empirical data of deposition	28
2.25	Empirical formula plots	30
3.1	Turbulence development	32
3.2	Wall function illustration	33
3.3	RANS illustration	34
3.4	IDDP-1 analysis	37
3.5	Deposition velocity plot from Chauhan (2019)	38
3.6	Particle concentration display by Chauhan (2019)	39
3.7	u^+ diagram for properties from Tandberg (2017)	41
3.8	Coupling scheme classification	43
5.1	Channel mesh grid illustration	47
5.2	V_{dep}^+ results for Tandberg (2017) simulation	48

5.3	Particle tracking illustration	49
5.4	Long pipe velocity profile	49
5.5	Particle deposition for 1e-05 diameter particles in a long pipe	52
5.6	Particle V_{dep}^+ integration	53
5.7	Particle deposition for 80 nm	54
5.8	V_{dep}^+ results, high velocity long pipe simulation	54
5.9	Schmidt number for long pipe simulation particles	55
5.10	V_{dep}^+ results for low velocity pipe flow	56
5.11	Schmidt numbers for low velocity profile	57
5.12	Low velocity thermophoretic deposition	58
5.13	Comparison of particle deposition for elongated pipe	59
5.14	Particle deposition of sub-micron particle in elongated pipe	60
5.15	Dimensionless deposition velocity for the elongated pipe	60
5.16	Upward flow pipe simulation	61
5.17	V_{dep}^+ results for geothermal pipe simulation	62
5.18	Geothermal pipe deposition by particle size	63
5.19	Schmidt number profile in geothermal steam	64
5.20	Deposited particles in the pipe bend	65
5.21	Particle tracking in bend.	65
6.1	V_{dep}^+ results from the Tian and Ahmadi (2006) study	67
6.2	Cunningham slip correction factor plot	69
6.3	Rarefied gas effect in geothermal well	70
6.4	Pipe bend from geothermal experiment	71
6.5	Sharp bend flow illustration	71
1	Velocity profile for low velocity pipe simulation	82
2	Velocity profile for elongated pipe simulation	82
3	Velocity profile for geothermal steam simulation	83
4	Dimensionless velocity profile for long pipe, high velocity simulation	84
5	Dimensionless velocity profile for long pipe, low velocity simulation	84
6	Deposition rate and velocity for 4 nm particles in high velocity simulation.	86
7	Deposition rate and velocity for 4 nm particles in geothermal simulation.	87
8	Deposition rate and velocity for for 1 μ m particles in high velocity simulation.	88
9	Deposition rate and velocity for for 1 μ m particles in low velocity simulation.	89
10	Deposition rate and velocity for 4 μ m particles in geothermal simulation.	90

List of Tables

5.1	Turbulence model options	46
5.2	Fluid & particle properties	51

Nomenclature

Abbreviations

AS	Amorphous Silica
avg	Average
CFD	Computational Fluid Dynamics
SSI	Silica Supersaturation Index
UDF	User-Defined-Function

Greek Letters

δ	Boundary layer thickness	m
η	Thermophoretic force coefficient	?
κ	Average roughness height	m
κ^+	Dim. less average roughness height	—
λ	Mean free path	m
λ_f	Moody friction factor	—
μ	Dynamic viscosity	kg/ms
ν	Kinematic viscosity	m^2/s
ω	Turbulent dissipation rate	s^{-1}
Φ	Thermophoretic gradient	—
ρ_f	Fluid density	kg/m^3
ρ_p	Particle density	kg/m^3
τ_p	Particle relaxation time	s
τ_p^+	Dimensionless particle relaxation time	—
τ_ω	Wall shear stress	N/m^2

Latin Letters

\dot{m}_s	Surface mass transfer	kg/m^2s
\vec{u}	Fluid velocity vector	m/s
\vec{v}	Particle velocity vector	m/s
c_0	Bulk flow particle concentrations	kg/m^3

C_c	Cunningham correction factor	–
c_p	Specific heat capacity	J/kgK
D_B	Brownian diffusion coefficient	m^2/s
d_p	Particle diameter	m
D_t	Turbulent diffusion coefficient	m^2/s
F_L	Lift force	N
g	Gravitational acceleration	m/s^2
h	Channel height	m
J	Particle flux	<i>particle/s</i>
k	Turbulent kinetic energy	m^2/s^2
k_B	Boltzmann's constants	$Jm/K \cdot molecule$
Mm	Molecular mass	g/mol
S_L	Stopping distance	m
Sc	Schmidt number ($= \nu/D$)	–
u	Fluid velocity	m/s
u_*	Fluid friction velocity	m/s
U_{avg}	Average fluid free stream	m/s
V_p	Particle velocity magnitude	m/s
V_{dep}	Particle deposition velocity	m/s
V_{dep}^+	Dimensionless deposition velocity	–
y	Distance from surface wall	m
y^+	Dimensionless wall distance	–
c	Particle concentrations	kg/m^3
Kn	Knudsen number ($= \lambda/D_p$)	–
O	Perimeter	m
P	Pressure	kPa
Re	Reynolds number	–
T	Temperature	K or °C

Subscripts

B Brownian

b	bulk
d	Deposition
p	Particle
S	Solubility
s	surface

1. Introduction

In this paper, a study of deposition and behaviour of different size silica particles will be made with the IDDP-2 field of the Icelandic deep drilling project in mind. The project aims to extract superheated geothermal steam from a reservoir in proximity to the "Reykjanes power plant", making this power plant the first in the world to utilize such a deep geothermal power source.

This paper is a continuation of a study started in 2018 (Paulsen, 2018), which is a part of an ongoing study by the department of Energy and process engineering at NTNU (NTNU, 2019), in cooperation with the Icelandic Deep Drilling Project (IDDP, 2019).

The necessity of this study stems from the ongoing problem of fouling in geothermal pipes under test flows of the Icelandic deep drilling project. These experimental wells are much deeper than conventional geothermal wells used in present plants, resulting in the reservoirs holding superheated steam of higher temperature and pressure than that of reservoirs closer to the surface. But the large energy potential of such deep drilled geothermal wells cannot be exploited if the extraction of superheated steam is continually exposed to fouling issues of the scope found in the testing of IDDP-1 steam flow (Karlsdottir et al., 2014).

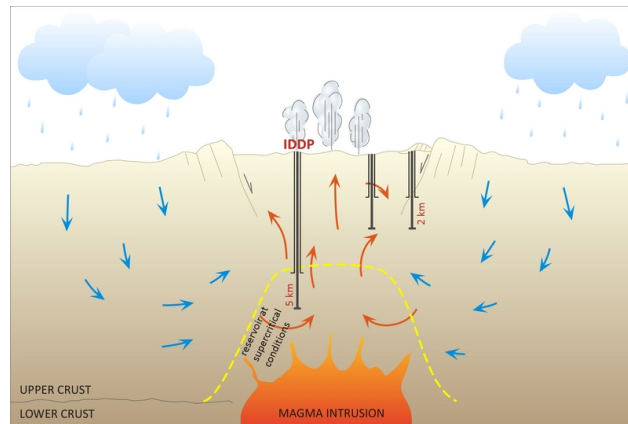


Figure 1.1: Illustration of the geothermal wells, where the IDDP wells contrasts to conventional wells. Picture retrieved from Orkustofnun (2018).

According to Brown (2011), fouling in superheated geothermal steam wells seems to be caused mainly by precipitation of polymerised silica molecules into colloidal silica particles, a process which will invariably occur due to expansion and cooling of the steam as it is extracted.

Esptein (1983) defines fouling as a process consisting of five events:

1. Initiation: Formation of particles which will deposit themselves upon a wall surface can happen in different ways. The polymerisation of suspended silica colloids will be explained in the subsequent chapter.

2. Transport: many different transport mechanisms are noticeable in particulate fouling, and those that are relevant to the present study will be presented in chapter 2.
3. Attachment: For particulate fouling, the sticking probability will greatly depend on the kinetics of the particles in question. Both intensive and extensive properties of the surrounding fluid will also affect the sticking probability.
4. Removal: This process may begin at the same time as attachment, but its magnitude is severely influenced by the conditions of the fluid flow.
5. Ageing: The continued growth of fouling layers will depend on continued mass transport of particulates, but will now be an interaction not between a wall surface and particles, but inter-particle interaction. The properties of the surrounding fluid is again an important factor.

The focus of this study will lie in transport of sub-micron particles onto a solid surface, with estimates for initiation and attachment being presented for the scenario of geothermal flow.

In the rest of this study, the processes and mechanics of colloidal silica precipitation and deposition will be presented, then subsequently implemented into numerical models for running simulations of deposition onto cylinder walls. These models will be a combination of the equation library of the chosen CFD-program and user defined functions introduced during computation. The choice of RANS-equations will be explained, and the different ways of solving the turbulence equation will be discussed. Finally, the results will be analyzed and compared to present deposition theory, and future works will be suggested regarding the numerical models and deposition theory.

2. Theory: Silica precipitation & deposition

2.1 Colloidal silica precipitation

As mentioned above, silica precipitation for the IDDP well is different from that of conventional wells, partly due to the lower pressure range, and partly due to the differences in concentrations of silicic acid and other particles within the solution at well head.

As shallower geothermal reservoirs have a much lower pressure and temperature range, the behaviour of silica precipitation is different from what occurs at a supercritical phase. In conventional wells, flashing separates the geothermal fluid into superheated steam and geothermal brine, resulting in most particles remaining in the geothermal brine, which contains concentration levels well above saturation limits. Therefore, previous studies like that of Kokhanenko (2014), Brown (2011) and Nancy Møller and Weare (1998) have always focused on polymerization and precipitation of colloidal silica in brine. However, the predictions of Fridriksson et al. (2015) enlightens the risk of silica fouling in supercritical steam flow from the IDDP-2 plant, which justifies this study.

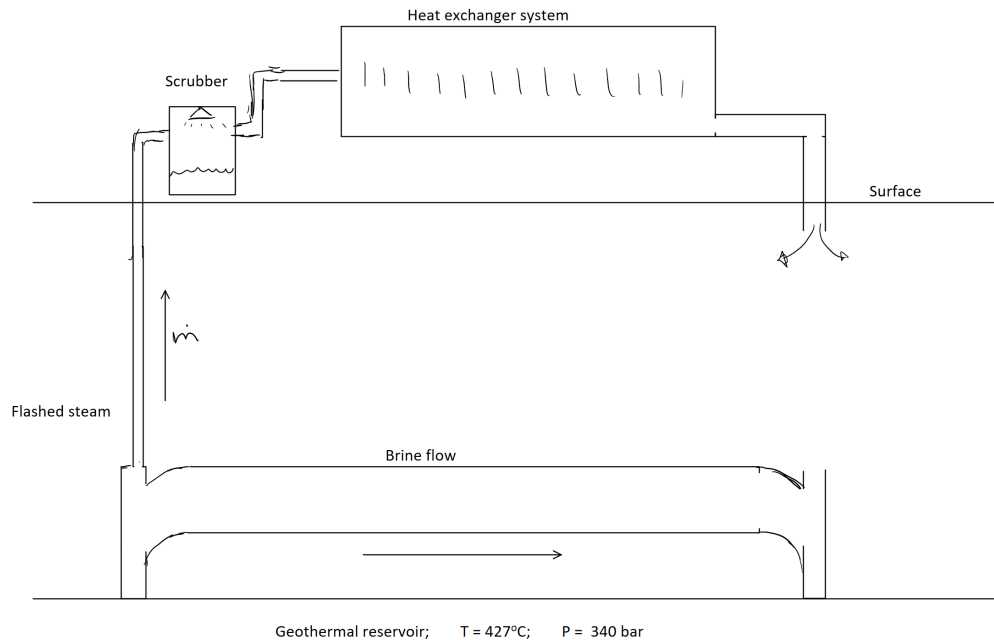


Figure 2.1: Simplified depiction of conventional geothermal steam extraction, where fouling mostly occurs in the brine flow.

Very little research exists on silica precipitation at temperatures present in supercritical reservoir conditions, nor at geothermal pipe flows in gas phase, which is the case for extracting

from such deep reservoirs as IDDP-2. That being said, the kinetics of silica precipitation in superheated steam is expected to be similar to that of geothermal brine.

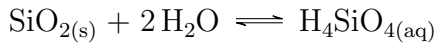
In this chapter, the formation of colloidal silica particles will be presented, along with a short explanation for the size distribution of the colloidal silica. This will justify the assumption for particle sizes and behaviour to be used in the numerical study of silica deposition.

2.1.1 Process of colloidal silica formation

Conditions for oversaturation & precipitation

Before discussing the behaviour of the particles in the fluid flow, it is necessary to take a closer look at the reactions taking place in the extraction and re-injection of the heat transfer fluid.

In the geothermal reservoirs, quartz and other minerals have achieved equilibrium with the superheated waters, resulting in a solution containing silica in its aqueous form:



Here, H_4SiO_4 is a silicic acid and SiO_2 is quartz. For the geothermal waters at high temperature (above 230°C), quartz is considered in equilibrium between the solid and dissolved species.

Robert O. Fournier and Jack J. Rowe (1977) presents an expression of dissolved silica concentration for temperatures between $0 - 250^\circ\text{C}$:

$$\log C = \frac{-1309}{T} + 5.19, \quad (2.1)$$

where C is silica concentration in mg/kg, and T is absolute temperature (K). The lower the temperature, the less able is the silica to dissolve in the fluid.

In equation 2.1, only temperature is accounted for when determining the solubility of dissolved silica. However, in geothermal reservoir, the high pressure also plays a major role in the solubility.

This solubility suggests that the reservoir fluid should contain less dissolved $\text{Si}(\text{OH})_4$, seeing how the oversaturation of silica is already reached. This can be explained by taking into account how other elements will react with silica, creating their own products. Both Karlsdottir et al. (2014) and Fridriksson et al. (2015) presents a composition of elements like fluorine and chlorine in geothermal reservoirs. Through this, the concentration demand of silica increases, and so more of it is dissolved into the reservoir fluid.

The precipitation of quartz is of little interest for geothermal wells, owing to the long time it takes for quartz to develop in over-saturated solutions. The threat of silica concentrations in geothermal fluids primarily arises from amorphous silica, a form of silica that is much more soluble than quartz. In measurements done by Robert O. Fournier and Jack J. Rowe (1977), the solubility of silica at saturated vapour pressure of water is expressed in equation 2.2.

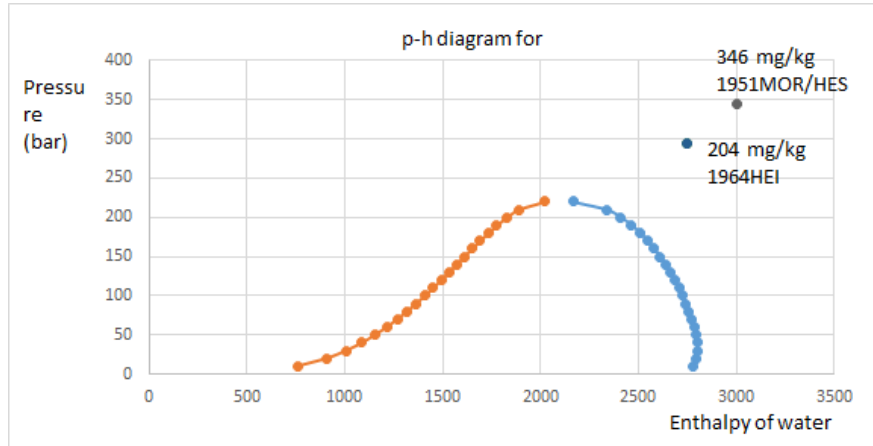


Figure 2.2: Plyasunov has collected solubility data for silica at different temperature and pressure levels. The processing of the data into this graph first presented in Bordvik (2020).

$$\log C = \frac{-731}{T} + 4.52, \tag{2.2}$$

The formula is stated to only be valid for saturated vapor between 0°C and 250°C. Implementation of the formula for the high pressure and high temperature steam of the geothermal system yielded unreasonable values for concentration of amorphous silica. Without exact data on the fluid composition, estimations can therefore only be made from experimental data, like those produced by Plyasunov (2012) and presented in figure 2.2.

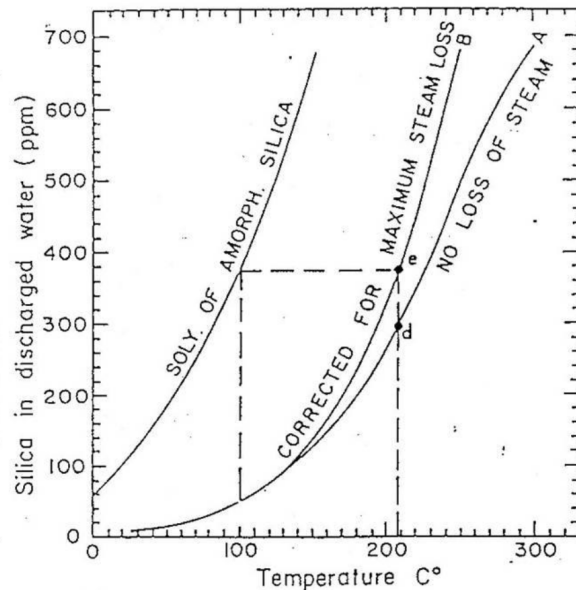


Figure 2.3: Computed solubility of silica and amorphous silica at saturated water pressure

Brown (2011) conceives that an increase in a solutions pH-level can improve the solubility of silica due to the higher ionization:

$$S = C[1 + (10^{pH} \times \frac{K_1}{\gamma(\text{H}_3\text{SiO}_4^-)})], \quad (2.3)$$

where K_1 is a dissociation constant determined as $\log K_1 = \frac{-2549}{T} - 15.36 \times 10^{-6}T^2$.

But as the solvent lies in the supercritical region, solubility behaves differently. At expansion, as water changes from liquid to gaseous behaviour in the supercritical region, the amount hydrogen bonds will reduce, making solubility easier, according to Brown (2011).

Considering the speed of which the steam will flow to the surface, precipitation of quartz, keatite, coesite and other silicon dioxides, and their subsequent deposition is practically impossible. Therefore, their precipitation can be ignored, and will merely function as a control on the amount of amorphous silica that is initially allowed to precipitate.

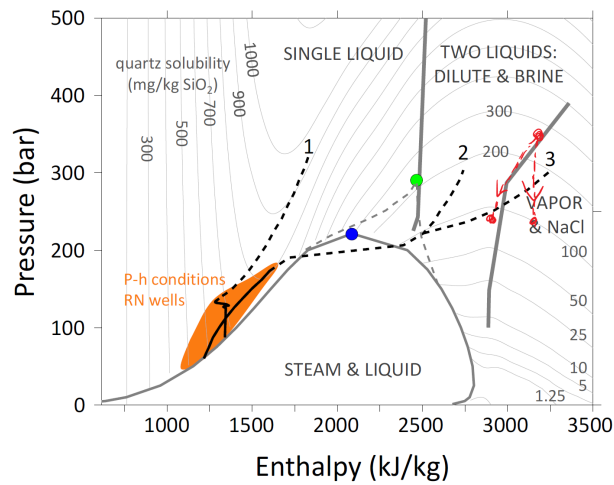


Figure 2.4: Pressure-enthalpy-diagram of water shows three scenarios of how the steam in the geothermal reservoir may have developed. Nr. 3 depicts the supercritical fluid most likely reached in IDDP-2. Retrieved from Fridriksson et al. (2015).

Bahadori and Vuthaluru (2009) presents an empirical formula for calculating silica solubility at high pressure levels in a boiler process, and those results can be read in figure 2.5. The measurements are taken from silica carry-over from water to steam, and Bahadori and Vuthaluru (2009) concludes that high pressure and temperature increases the solubility of silica, as such conditions leads to silica acting like a gas and enters the steam from water in a volatile form:

Many of the principles for silica agglomeration about to be presented have only been analyzed for silica dissolved in liquid, as presented in Brown (2011) and Kokhanenko (2014), but not precipitation of silica in superheated steam. It is important to recognise that some of the effects and conditions which silica agglomeration is dictated by in these theories may be weaker in a gaseous solution.

Based on the equilibrium amorphous silica solubility, the silica saturation index (SSI) has been presented by Brown (2011). The index is defined as ratio of H_4SiO_4 concentrations in

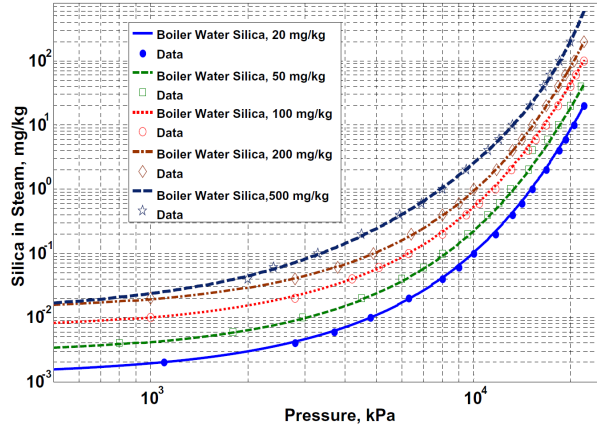


Figure 2.5: Predicted solubility of silica compared to experimental data, plotted by Bahadori and Vuthaluru (2009)

the solvent (the geothermal steam for this problem) divided by the equilibrium at prevailing conditions (solubility measured in mg/kg).

$$SSI = \frac{\text{concentration of silica in solution}}{\text{equilibrium solubility of amorphous silica at prevailing conditions}} \quad (2.4)$$

When the $SSI > 1$, the solution is supersaturated, enabling precipitation of AS and polymerization of colloidal silica. As more and more silica agglomerates, the concentration drops, decreasing SSI.

Research by Manning (1994) reveals that silica can easily dissolve in steam at high temperature and pressure, which makes a high concentration of silica in the geothermal steam very likely.

As the solution enters the well-head, sudden expansion causes a large pressure drop in the supercritical fluid, according to Fridriksson et al. (2015).

This pressure drop causes the silica saturation index (SSI), to increase well above 1, initializing the first stage in colloidal silica polymerisation, nucleation of silicic acid particles into amorphous silica.

Nucleation is the combination of two silicic acid molecules, forming the dimer H_6SiO_4 and H_2O , and is displayed in 2.6. The reaction is catalysed by hydroxyl ions (OH^-), such that by lowering the pH-level to lower the OH^- concentration retards the reaction.

The random bonds formed by nucleation means that the polymer formed by the process have no crystal structure, and as only two molecules are needed to initiate the reaction, this nucleation is considered homogeneous. Brown (2011) explains how the continuation of silica nucleation depends on various factors such as temperature, solution pH and the presence of seed particles. These are particles with which condensation can occur upon, affecting the solubility of the solution. According to Bordvik (2020), at pH levels of 2-3, which is the

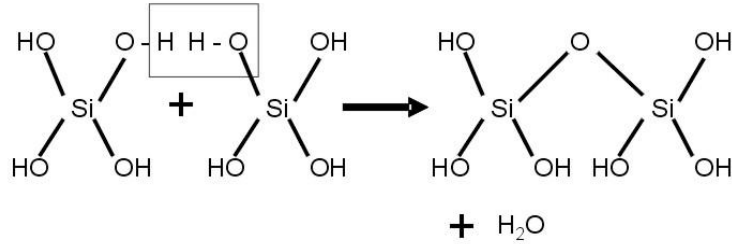


Figure 2.6: Initial molecular reaction of silica colloid formation is nucleation.(Brown, 2011)

range of geothermal waters, the critical radius is reduced such that silica particles of 2 - 4 nm emerge.

As equation 2.2 presents, increasing the temperature will increase the solubility and subsequently lower the SSI. This means that a higher temperature steam will have a shorter nucleation period.

At a certain point enough silica have fused together so that the energy demanded to continue nucleation is higher than the energy required to precipitate onto surfaces. At this metastable state, any silica particle below a critical radius will dissolve and precipitate onto larger colloidal silica. Brown (2011) titles this process "Ostwald ripening", which will depend on pH levels and concentration of silica particles in the solution. This particle polymerization will continue as long as the supersaturation index is above 1, i.e. as long as the concentration of AS in the solution exceeds the solubility of AS in the solution. Therefore an important factor is the rate at which the solution reaches oversaturation. The faster SSI crosses 1, the more nuclei are formed. Nucleation of more molecules will leave less monomeric silica in the solvent. This decreases heterogeneous condensation of monomeric silica onto nuclei, which in turn will prevent large colloidal growth.

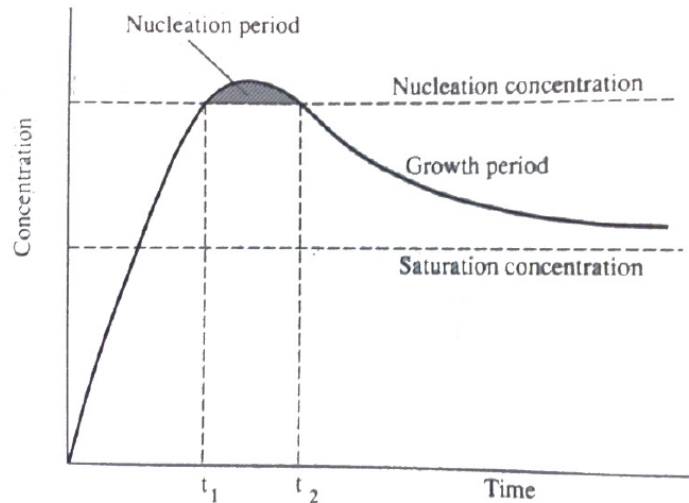


Figure 2.7: The La Mer diagram displays the window when nucleation is possible by concentration of amorphous silica, presented by Kokhanenko (2014).

Regardless of the temperature, the biggest contribution to the nucleation period is the rate at which the solution reaches oversaturation. The faster SSI crosses 1, the more nuclei are formed. Nucleation of more molecules will leave less monomeric silica in the solvent. This decreases heterogeneous condensation of monomeric silica onto nuclei, which will in turn prevent large colloidal growth.

Ionization and pH effects on precipitation

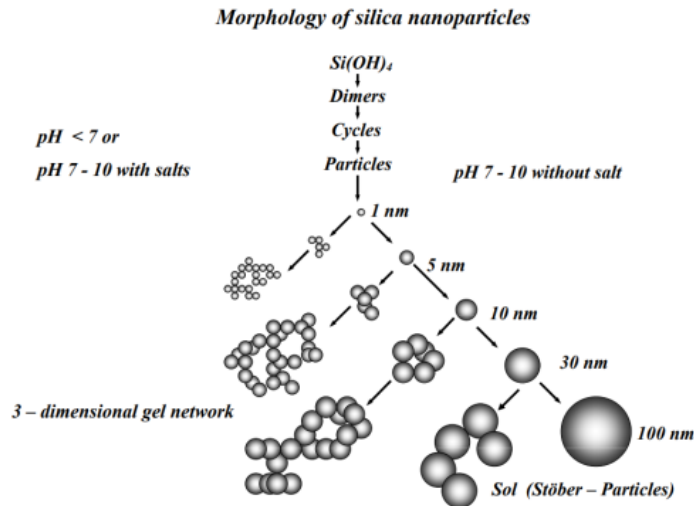


Figure 2.8: The figure shows the agglomeration of precipitated amorphous silica varying with pH levels of the solution. Provided by Bordvik (2020)

Colloidal silica has a natural negative surface charge, which repulses other silica particles. This works as a negative factor on agglomeration. The presence of salts in the solution will decrease the negative surface charge of silica particles when in contact with them, which increases the odds of further agglomeration

Lowering the pH of the fluid also leads to lowered silica precipitation. Experiments by Fleming (1986) shows a proportionality between solution pH and silica polymerization rate in NaCl solutions. As the surface charge of the silica particles are dependent on the pH of its surroundings, lowering the pH will consequently lower the silica's ability to further polymerize.

As the steam is expected to be over-saturated once expanded, making the oversaturation rate very rapid, nucleation will dominate the polymerization process.

As the SSI reaches the meta-stable region ($SSI > 1$), any nuclei below a critical size will dissolve, and the freed silica molecules will only be able to precipitate through growth of the remaining nuclei. Thus, the rate of supersaturation $\frac{dSSI}{dt}$ also affects the size range of colloidal silica.

2.2 Silica deposition effects

The rate of which colloidal silica deposits onto a surface is closely linked to the size distribution of the particles, and many different effects will have various impact upon the particle trajectory, sticking probability and removal probability.

Much of this chapter is retrieved from the previous project work by Paulsen (2018). Certain effects are of less importance due to the assumed lower particle size distribution anticipated in this study compared to that of the previous project.

The deposition of colloidal silica particles in superheated turbulent steam flow will now be discussed. This process of particle deposition involves many different effects. Certain initial conditions and boundaries must be determined to make the calculation practical.

The initial distribution of silica particles will be even at inlet, in accordance with turbulence theory.

The chapter will begin by describing how deposition of particles are measured, and presenting the theoretical regions where deposition is governed by different mechanisms. The remaining chapter is reserved for presenting the different mechanisms and their effects on particle motion.

2.2.1 Describing deposition rates

When comparing particle deposition, it is useful to depict it by nondimensional deposition velocity, V_{dep}^+ , vs nondimensional particle relaxation time, τ^+ .

The deposition velocity is determined as mass transfer rate on the surface by bulk particle density:

$$V_{dep} = \frac{\dot{m}_s}{\rho_{p,m}} \quad (2.5)$$

The particle relaxation time describes particle inertia as the time scale with which any slip velocity between particles and the fluid is equilibrated.

Initially, the particle relaxation time from the inertia of the fluid flow can be determined as

$$\tau_l = \frac{\rho_p d_p^2}{18\mu}, \quad (2.6)$$

where ρ_p is the particle density, μ is the dynamic viscosity of the surrounding fluid and d_p is the particle diameter.

However, as particles decrease in size, the decreased particle collision leads to a lower particle drag effect on the tracked particles. Guha (2008) defines this effect as the "rarefied gas effect", which can be accounted for by adding the Cunningham slip correction factor to the particle relaxation rate.

$$C_c = 1 + 2Kn[1.257 + 0.4 \exp -0.55Kn^{-1}]. \quad (2.7)$$

Here, Kn is the Knudsen number defined as the ratio of molecular mean free path and particle size, $Kn = \frac{l_0}{2r}$, where l_0 is the mean free path of the surrounding fluid flow and r is the particle radius. The proportionality of the Knudsen number clearly shows that a smaller particle will have a greater rarefied gas effect. Thus, the resulting particle relaxation rate becomes:

$$\tau_p = \tau_l * C_c = \frac{\rho_p d_p^2}{18\mu} * C_c \quad (2.8)$$

Another way to think about τ_p is that particle relaxation time can be multiplied with the current particle velocity to yield its stopping distance:

$$S_L = V_p * \tau_p \quad (2.9)$$

Both parameters are made dimensionless with help of the fluid friction velocity, defined as the ratio of the wall shear stress and fluid density: $u_* = \sqrt{\frac{\text{shear stress}}{\text{fluid density}}}$:

$$V_{dep}^+ = \frac{V_{dep}}{u_*} \quad (2.10)$$

$$\tau_p^+ = \frac{\tau u_*^2}{\nu}, \quad (2.11)$$

where ν is the kinematic fluid viscosity.

Ayse Altunbas (2002) presents a way of expressing frictional velocity by mean velocity in equation 2.12.

$$u_* = \sqrt{\frac{\tau_w}{\rho_f}} = \frac{0.2V_m}{Re^{\frac{1}{8}}} \quad (2.12)$$

An expression for shear stress τ_w in a fully developed flow through a pipe has been presented by Schlichting (1968) in equation 2.13

$$\tau_w = \frac{1}{8} \lambda_f \rho_f V_m^2, \quad (2.13)$$

, where V_m^2 is the mean fluid velocity in the pipe, and λ_f is the moody friction factor, which for $2.1 \times 10^3 < Re < 10^5$ can be estimated from the Blasius equation 2.14.

$$\lambda_f = \frac{0.3164}{Re^{\frac{1}{4}}} \quad (2.14)$$

In conventional fouling theory, deposition rates and applicable mechanisms have been divided into three regions depending on the particle size and subsequent relaxation time. Guha (1997) Presents a unified deposition chart over relaxation time. (figure 2.9)

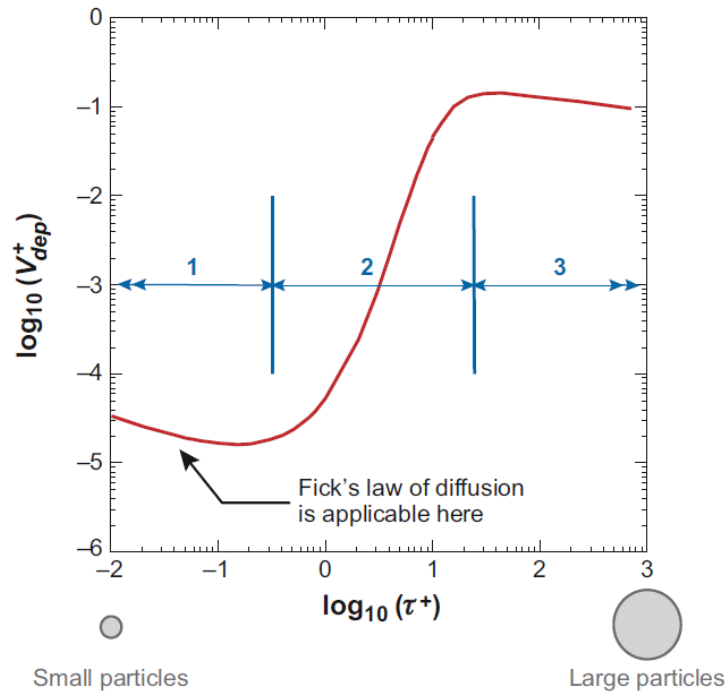


Figure 2.9: Variations in measured deposition velocity of silica in water with particle relaxation time in a fully developed pipe flow. (Guha, 2008)

1. The first regime is governed by turbulent and molecular diffusion. An increase in particle size and / or decrease in temperature will decrease these mechanisms.
2. The eddy diffusion-impaction regime is where particles grow large enough for eddies to impart momentum onto them when transferring from the turbulent boundary layer to the viscous sublayer, greatly increasing V_{dep}^+ with d_p .
3. In the particle inertia moderated regime, where V_{dep}^+ decreases slightly as particles are growing too inert for turbulence to successfully impart momentum.

It is worth noting that, as the deposition in this problem consists of particulates suspended in a turbulent gas instead of liquid, any comparison with deposition velocities by Guha (2008) or Kokhanenko (2014) must take the decreased viscosity into account. As has been pointed out in the Cunningham equation 2.7, smaller particulates interact very easily with turbulent eddies in the solvent flow, and the more violent these eddies are, the faster the particles will move (Esptein, 1983). It is therefore expected that deposition velocity for geothermal flows may be several exponents higher than those of Guha (2008). It also opens for the possibility that deposition velocity will increase exponentially with Reynolds number, as both diffusion and imparted momentum are proportional to its value.

Regions of influence

Before discussing the effects on particle deposition, the different boundaries in which the effects are to be introduced should be further determined. Kokhanenko (2014) presents a description of turbulent boundary layers.

Looking at a small section of a potential turbulent flow over a heat exchanger surface, Kokhanenko (2014) defines four regions of which are of interest for particle deposition.

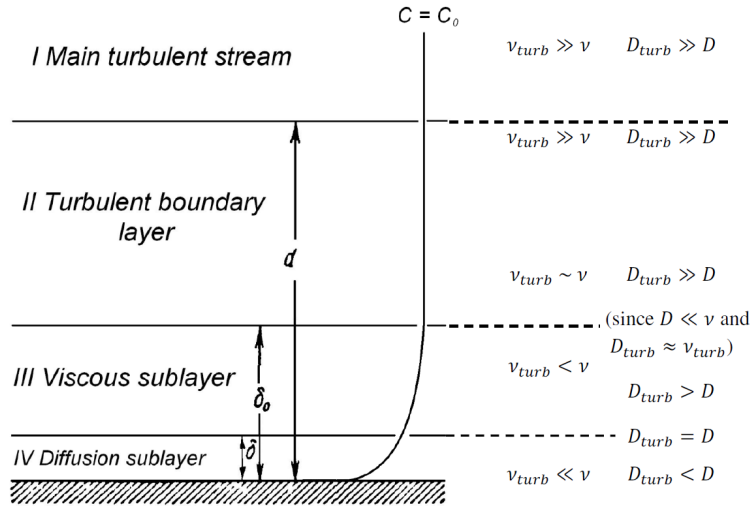


Figure 2.10: Mass transfer in the turbulent boundary layer.

Approaching the surface interface, the concentration enters the turbulent boundary layer, of which turbulent diffusion still dominates. The next conventional layer is the viscous sublayer, at which viscous dissipation generated by the laminar flow may halt particulates of reaching the wall surface. For larger particles, momentum imparted to them from the turbulent flow may carry them through this layer onto the surface, but for smaller particles, dissipation is certain without aid from other transport mechanisms. Finally, figure 2.10 displays a fourth layer, at which any turbulence diffusion becomes negligible due to viscous dissipation, even for larger particles. Other diffusive mechanisms will then govern the sticking probability of the particulates. It is worth noting that this definition is retrieved for colloid deposition in liquid flow, particularly geothermal brine with particulates of varying sizes (Kokhanenko, 2014).

Any mass transport can therefore be divided between the turbulence governing region (requiring only a turbulent transport equation) and a near-wall particle diffusion - dominated region.

2.2.2 Turbulent- & molecular diffusion

The mass transfer mechanisms that define particulate fouling can be divided into two categories. The first mechanism is mass convection as bulk transport of particle, while the second is particle diffusion, determined by turbulence and temperature.

The relevance of either mechanism can be determined by the value of the Schmidt number

$$Sc = \frac{\nu}{D} \quad (2.15)$$

where ν is kinematic fluid viscosity and D is a diffusion coefficient.

For a turbulent pipe flow, the mass transfer by diffusion will be made up of turbulent diffusion and the Brownian diffusion coefficient, D_B . Named after physicist Robert Brown and forwarded by Albert Einstein and Marian Smoluchowski, this phenomenon describes the random movement of nuclear particles in motion due to high internal energy.

Guha (1997) defines the molecular Brownian diffusion with the Einstein equation.

$$D_B = \left(\frac{kT}{6\pi\mu r}\right)C_c, \quad (2.16)$$

where k is the Boltzmann constant, T is absolute temperature and the Cunningham slip correction factor is described in equation 2.7. Again the Knudsen number $Kn = \frac{\text{mean free path}}{\text{particle size}}$ is an important factor for particle motion. It shows that smaller particles will be more susceptible to molecular diffusion. As different studies uses different constants for the slip correction factor and Knudsen numbers, the mean free path of the fluid compound must be analyzed in order to choose the correct definition for turbulent fluid flow with geothermal conditions.

Multiple expressions for molecular collision mean free path have been presented over time. The average distance a molecule travels before collision with another molecule will naturally depend on the concentration of molecules in the given volume, i.e. l is inversely proportional to a number of molecules N in a given volume. The other big factor is the size of the cross-section of the particle, which for spherical particles in gases are determined as $\sigma_c = \pi d$, i.e. the smaller the cross-section, the longer the particle can travel.

Mills (2001) Presents the most conventional expression for the collision mean free path:

$$l_0 = \frac{1}{\sqrt{2}\sigma_c N}, \quad (2.17)$$

where N is the the molecule number density in $1/\text{m}^3$ and expressed as

$$N = \frac{P}{k_B T}. \quad (2.18)$$

For the standard conditions of air at 1 bar and 20° the mean free path is presented as $l_{0ref} = 0.0664\mu\text{m}$ in Crowe (2006), and can be adapted for pressure and temperature with the following formula:

$$l_0 = l_{0ref} \left(\frac{101}{P}\right) \left(\frac{T}{293}\right) \left(\frac{1 + 110/293}{1 + 110/T}\right), \quad (2.19)$$

where pressure is scaled to kPa.

Besides standard kinetic theory, other expressions for the mean free path have been suggested, where mean free path relates to macroscopic properties like viscosity:

$$l_0 = \nu \times \sqrt{\frac{\pi Mm}{2RT}}, \quad (2.20)$$

where Mm is the molecular mass of the suspended fluid. The composition of the geothermal steam is not yet determined sufficiently in order to express an accurate mean molecular weight, but this formula can be used to study particle deposition when air flow is assumed.

Guha (1997) also suggests this expression:

$$l_0 = \mu \frac{\sqrt{2\pi RT}}{2P} \quad (2.21)$$

Equation 2.21 does account for an increase in overall fluid pressure, an important factor for geothermal conditions. The correlation of these equations, and the consequences for further computations will be addressed in chapter 4.

Considering how very small particles will move relatively small distances in comparison to the whole system, it may be expected that the diffusive coefficients of the silica be quite small in a suspended flow, which means the Schmidt number will be very large. Kokhanenko (2014) computes Schmidt numbers for a turbulent pipe flow of geothermal brine; $Sc_{Si\ monomer} \approx 10^3$ and $Sc_{Si\ colloid} \approx 10^6$ for monomeric and colloidal silica respectively (Kokhanenko, 2014). However, by considering the dependencies of pressure and temperature of mean free path, the conditions of geothermal flow (high temperature and pressure) causes quite large diffusive coefficients, simultaneously lowering the Schmidt number. These will be computed in chapter 4.

The regions of diffusion mechanisms influence are depicted in the figure of turbulent boundary layers [figure 2.10, chapter 2.2.1]. The thickness of this diffusion boundary layer δ is determined by the Schmidt number and the dynamic profile of the flow. In the case of laminar flow over a flat plate, the thickness is found from

$$\delta \approx 0.6 * \left(\frac{1}{Sc}\right)^{\frac{1}{3}} d_l, \quad (2.22)$$

where d_l is the thickness of the hydrodynamic boundary layer. Turbulent boundary layer theory offers many alternatives, one of which is presented by Prandtl:

$$\frac{\delta}{x} \approx \frac{0.37}{Re_x^{1/5}} \quad (2.23)$$

, but it should be noted that all these formulas are based upon empirical research, and are therefore circumstantial.

For a turbulent flow, the momentum- and mass transfer provided by violent velocity changes is determined by the turbulent viscosity of the flow ($\frac{\nu}{\nu_{turb}} \approx \frac{1}{Re}$). This turbulent diffusion

will naturally be much larger than molecular diffusion everywhere but for a thin layer (δ_0) at the surface (figure 2.10), called the viscous sublayer.

Thus, the diffusion is defined as

$$D_{turb} \approx \nu_{turb} \sim \nu \frac{y^4}{\delta_0}. \quad (2.24)$$

Studying figure 2.10 for a turbulent flow, the mass transfer mechanisms become clearer. In the core flow (region 1), the fully developed turbulence causes constant average velocity, a dominant eddy turbulence, and therefore a flat silica concentration across the free stream cross area, and a large particle diffusion towards the wall. When entering the turbulent boundary layer, the average velocity decreases, although the continued dominance of turbulent diffusivity means silica concentration remains nearly constant. In the viscous sublayer (region 3), the fluctuations from turbulence still have a much bigger impact than molecular diffusion, so that only the innermost part of the viscous sublayer (region 4) have a molecular diffusion larger than D_{turb} .

$$D_{turb}^y = \delta = 10\nu \left(\frac{\delta}{\delta_0}\right)^4 = D \quad (2.25)$$

The crossing of the concentration from the turbulent flow into the laminar sublayer at a stopping distance S marks the point of which momentum imparted by turbulence seizes to transport the imparted particles. Now other mechanisms, which will be presented in subsequent sections, must be considered. Kokhanenko (2014) determines the thickness of the diffusion sublayer by equation 2.15 and 2.25:

$$\delta = \frac{\delta_0}{Sc^{\frac{1}{4}} \sqrt{10}} \quad (2.26)$$

When looking at the rate of diffusion mass transfer, it can be determined by the corresponding diffusion coefficient and local concentration gradient, C_0 , which is explained to be inversely proportional to the viscous boundary layer thickness:

$$J_{diff} = \frac{DC_0}{\delta}. \quad (2.27)$$

In conventional fouling theory, this equation is a modified version of Fick's law of diffusion (Philibert, 2005). Guha (2008) presents another version which separates the turbulent diffusion from the Brownian diffusion:

$$J_{diff} = -(D_B + D_t) \frac{d\rho_p}{dy}, \quad (2.28)$$

where $\frac{d\rho_p}{dy}$ is the gradient of particle partial density along the perpendicular distance y of the surface.

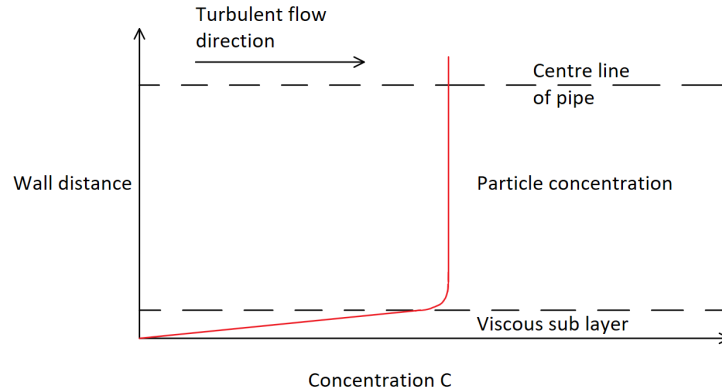


Figure 2.11: Due to turbulent diffusion, the concentration of colloidal particles is nearly constant at all levels except close to the wall, where particle deposition is governed by molecular diffusion and thermophoresis.

Interpreting these formulas, it is clear that Fick's law has deposition velocity decrease with increasing relaxation time (As D_B is inversely proportional to particle radius), which explains the first region of figure 2.9. Brown (2011) illustrates the mechanism by stating that colloidal particles, larger and with lower diffusivity than amorphous silica, have higher scaling rates than amorphous silica. This doesn't explain the sharp increase of region 2 however, directly opposing Fick's theory. This region must therefore be dominated by the inertia which the fluid imparts upon the suspended particles.

Silica deposition layer and surface charge

One of the great challenges of simulating this scenario arises in the deposition behaviour of colloidal silica onto already deposited silica film. From empirical data, it is clear that the initial deposition of silica onto pipe surface has deposition probability of near 1, creating an initial layer of silica film immediately after opening the well head. As mentioned in chapter 2.1.1, the negative surface charge ensuring the stability of colloidal silica suspended in the fluid now acts as a retardant against further colloidal deposition, as particles approaching the silica film must overcome the negative charge before Van der Waal forces fuse the particles together. The near perfect deposition taking place initially between the particulates and the surface wall may therefore dissipate, a phenomenon which has been proven by Bowen and Epstein (1978).

In order to take into account the effects of particle interaction with a charged film layer, the method of tracking the particle deposition would become more complex, and outside the scope of this study. Tian and Ahmadi (2006) and Hewett and Sellier (2015) presents transient simulation methods for building deposition layers onto surface walls, but these methods are not yet validated. Therefore, the author has opted for only tracking particles onto a pipe wall surface, assuming a uniform sticking probability.

Surface Roughness & Turbulence

An important point to make when talking about silica deposition in turbulent flow is that the interaction is not purely between the colloids and the surface area. Due to the high velocity and saturation of the pipe flow, a small amount of silica will deposit nearly instantly onto the surface, and is so far impossible to account for in deposition rate analysis. Their interaction with further deposited particulates can and must therefore be taken into account when discussing the mechanisms.

No surface is completely smooth, and so the real geometry of a surface should in theory always be accounted for in hydrodynamic boundaries. Surface roughness can affect even laminar flow, but the effect of the roughness increases the lower the laminar sublayer, i.e. with increasing Reynolds number.

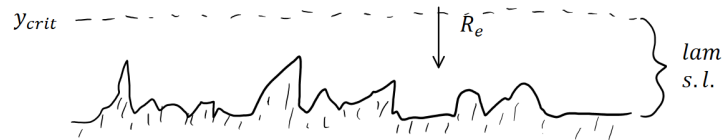


Figure 2.12: As the laminar sublayer decreases, the heights of the surface will penetrate the velocity interface.

The roughness is an important factor in the 1st and 2nd region of Guhas' deposition velocity diagram 2.9. For particles of varying sizes, there is a chance for particles to get "stuck" onto roughness heights when meeting the right criteria. This mechanism has been given the name "Interception" and depends of the walls effective roughness height k_s and particle radius. The roughness will shift the origin of velocity profile, e ($e = f(k_s)$), and the criterion for particles risking interception is to reach the roughness height, that is, reaching a distance $b = k_s - e = k_s - f(k_s)$. The particle is assumed to be intercepted when its center is at a distance r away from the effective roughness height, where r matches particle radius.

This effect is crucial in explaining the initial surface layer of silica film, the assumption being a complete sticking probability of 1 initially, but is important to recognize that surface roughness will alter continually as a fouling layer builds upon a wall surface. For this reason it becomes difficult to account for surface roughness in the simulations of the present study.

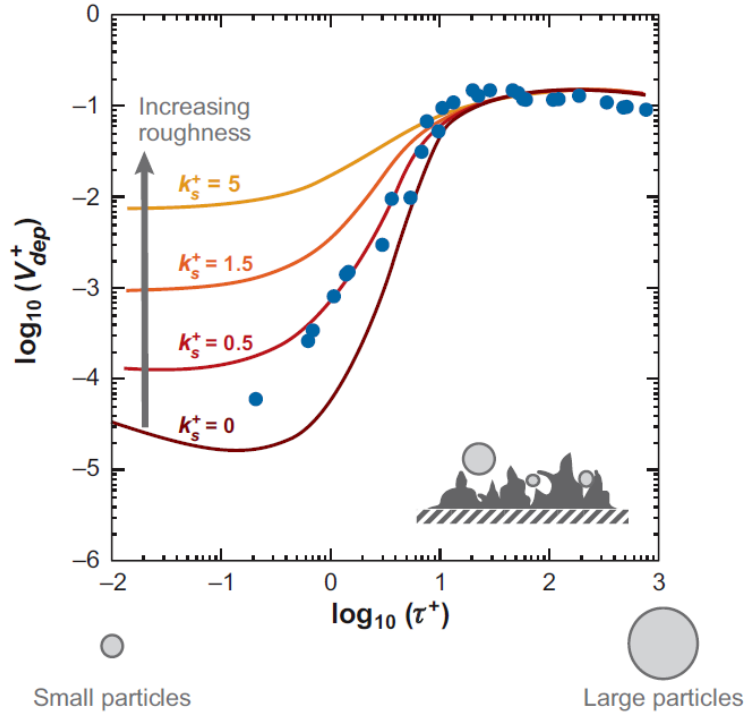


Figure 2.13: Deposition rate influenced by surface roughness, by Guha (2008).

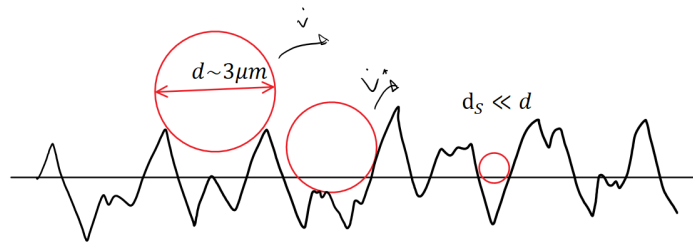


Figure 2.14: Depending on particle size, the colloidal silica may hitch itself onto the rough surface.

2.2.3 Thermophoresis

Due to the molecular size of the silica colloids, one reasonable effect to consider when looking at the deposition, is thermophoresis. The term points to the phenomena of suspended particles' behaviour to the force of a temperature gradient. Normally, particles suspended in a fluid will be moved by this force in the opposite direction of the temperature gradient, i.e. away from the heat source.

Thermophoresis can be witnessed by looking at a kerosene lamp. The soot particle suspended in the glass will over time stick to the glass, having moved away from the fire.

Research done by Talbot et al. (1980) gives us a sufficient definition on the force influencing the particles and the resulting velocity vector.

Within the heated boundary layer, the sum of forces on the suspended particles can be



Figure 2.15: The soot layer covering the glass of an old kerosene lamp can be attributed to thermophoretic diffusion from the flame in the lamp.

described as

$$F = F_V + F_T \quad (2.29)$$

where F_V represent the slip correction for Stokes viscous drag formula, and F_T is the thermophoretic force on the particles.

A recent study by Helden et al. (2015) highlights the effects of thermophoresis for a single colloid. Looking at the phenomenon through the Fokker-Planck equation:

$$\frac{\partial p}{\partial t} + \nabla J = 0, \quad (2.30)$$

where $p(x,y,z,t)$ defines particle probability density and J defines the probability current, we can focus the effects of thermophoresis perpendicular with the surface by integrating for x and y :

$$\frac{\partial p}{\partial t} + \nabla J_z = 0, \quad (2.31)$$

where $p = p(z, t)$ and $\frac{\partial J_z}{\partial z} \Big|_{z=0} = \frac{\partial J_z}{\partial z} \Big|_{z=L} = 0$.

Now we can write the probability current J_z along the temperature gradient as

$$J_z = \frac{f}{\gamma} p - p D_T \frac{\partial T}{\partial z} - D \frac{\partial p}{\partial z}. \quad (2.32)$$

In equation 2.32, the first term on the right hand side represents all particle wall interactions, while the second term describes the effect of thermophoretic drift proportional with the temperature gradient D_T . The third term represents thermal diffusion, based on Einstein's diffusion constant $D = \frac{k_B T}{\gamma}$.

For turbulent flow over a heat transfer surface, temperature, like flow concentration, will be nearly constant over most of the flow cross-section.

Combined with research by Guha (2008), the following force definition was reached:

$$F_T = \left(\frac{\eta}{m}\right) \nabla \ln T, \quad (2.33)$$

where the thermophoretic force coefficient is determined as

$$\eta = \frac{2.34(6\pi\mu\nu r)(\lambda_r + 4.36Kn)}{(1 + 6.84Kn)(1 + 8.72Kn + 2\lambda_r)}, \quad (2.34)$$

where λ_r is the ratio of thermal conductivity for fluid and particles ($\lambda_r = \frac{\lambda}{\lambda_p}$).

In order to implement the thermal force with deposition velocity of Ficks law, the temperature diffusion coefficient can be defined as:

$$D_T = D_B \left(1 + \frac{\eta}{kT}\right). \quad (2.35)$$

The behaviour of the suspended particles in view of a thermophoretic force is inertial, which means the effect of thermophoresis is proportional with the size of the suspended particles. As the effect rises quickly with decreasing particle radius, adding this mechanism to the deposition diagram 2.9 explains the swift rise of V_{dep}^+ at region 1 and 2 of figure 2.9. Im and Chung (1983) Has presented collection efficiency of deposited particles due to thermophoresis in comparison to experimental data in figure 2.16.

Viewing the thermophoretic force and its contribution to mass transfer (equation 2.33), it is clear that thermal diffusivity aids the deposition velocity for higher temperature gradients. For a system like this scenario presents, where the temperature difference between the pipe wall and bulk temperature can easily reach 50 K, this effect will clearly contribute to deposition velocity and potential silica scaling.

U.S. Kleinhans (2015) presents a non-dimensional function for a thermophoretic gradient dependent on the thermal conductivity ratio of the particles and solution, Φ (figure 2.18).

$$\frac{F_{th}\rho_g}{\mu_g^2} = \Phi \frac{d_p \nabla T_g}{2T_g} \quad (2.36)$$

, where ρ_g, μ_g, T_g are density, dynamic viscosity and temperature of gas-phase solution.

The temperature gradient of the gas solution is normally three-dimensional. Φ is a function of the Knudsen number and thermal conductivity ratio: $\Phi = \Phi(Kn, \Lambda)$. For such particles

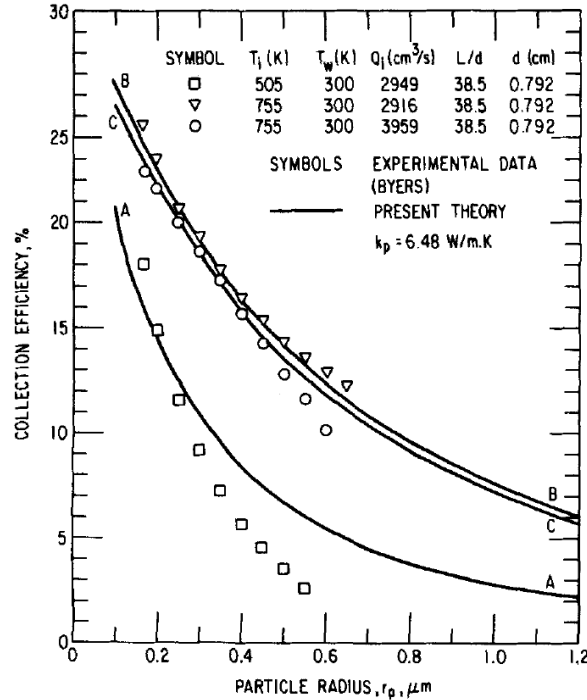


Figure 2.16: Thermophoretic efficiency with respect to particle size and temperature difference. Figure retrieved from Im and Chung (1983).

Gao and Jelle (2019) presents empirical data for thermal conductivity and mean-free paths for amorphous silica particles, providing useful parameters for further simulations.

It should be noted how the effect of thermophoresis per mass concentration of particles decrease with increasing Knudsen number. This will initially seem incorrect, as smaller particles will be more influenced by thermophoretic force. However, at extremely small particles, such as nanoparticles and smaller, figure 2.18 implies that diffusion will not operate the same way as usual for free stream particles. Thermal conductivity is presented for particles from > 1 to 500 nm in figure 2.19.

While it clearly shows a decrease in conductivity with decreasing particle size, the decrease is rather small (only 3.75 %). This could be related to the very small phonon mean free path of amorphous silica ($l_0 = 0.59 \text{ nm}$), such that the size effect would only become dominant for particles below 1 nm. Gao and Jelle (2019) presents a thermal conductivity of $0.539 \text{ W m}^{-1} \text{ K}^{-1}$, actual for a surface roughness of $p = 0.4$.

It is important to differ between the conductivity of dispersed nanoparticles and other structures such as silica aggregations. Appropriate for the current studies, silica aerogels will have an overall thermal conductivity of about 0.012 to $0.018 \text{ W m}^{-1} \text{ K}^{-1}$ according to Koebel and Rigacci (2011). The particles can be similar to aluminosilicates Al–Si investigated by U.S. Kleinhans (2015). These particles have a conductivity of 0.5 to $1.5 \text{ W m}^{-1} \text{ K}^{-1}$ at temperatures around 1000°C . U.S. Kleinhans (2015) plots the thermophoretic force as a function of particle diameters for a particle conductivity of $1 \text{ W m}^{-1} \text{ K}^{-1}$:

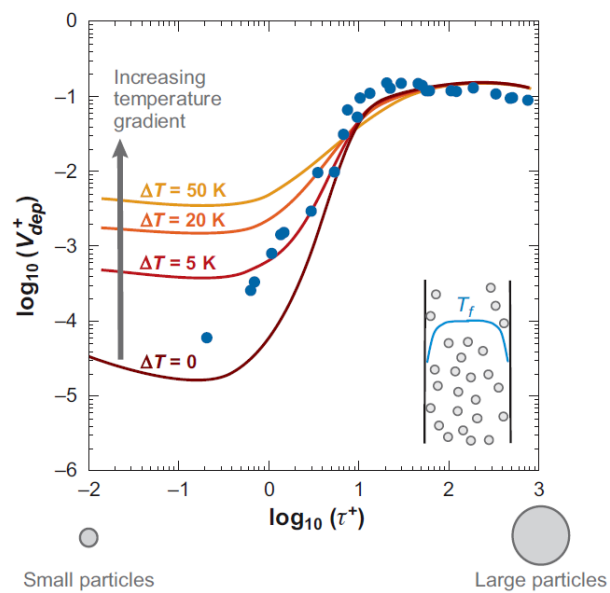


Figure 2.17: Effects of thermal diffusion on deposition rates, depicted by Guha (1997) and compared to results of Liu and Agarwal (1974)

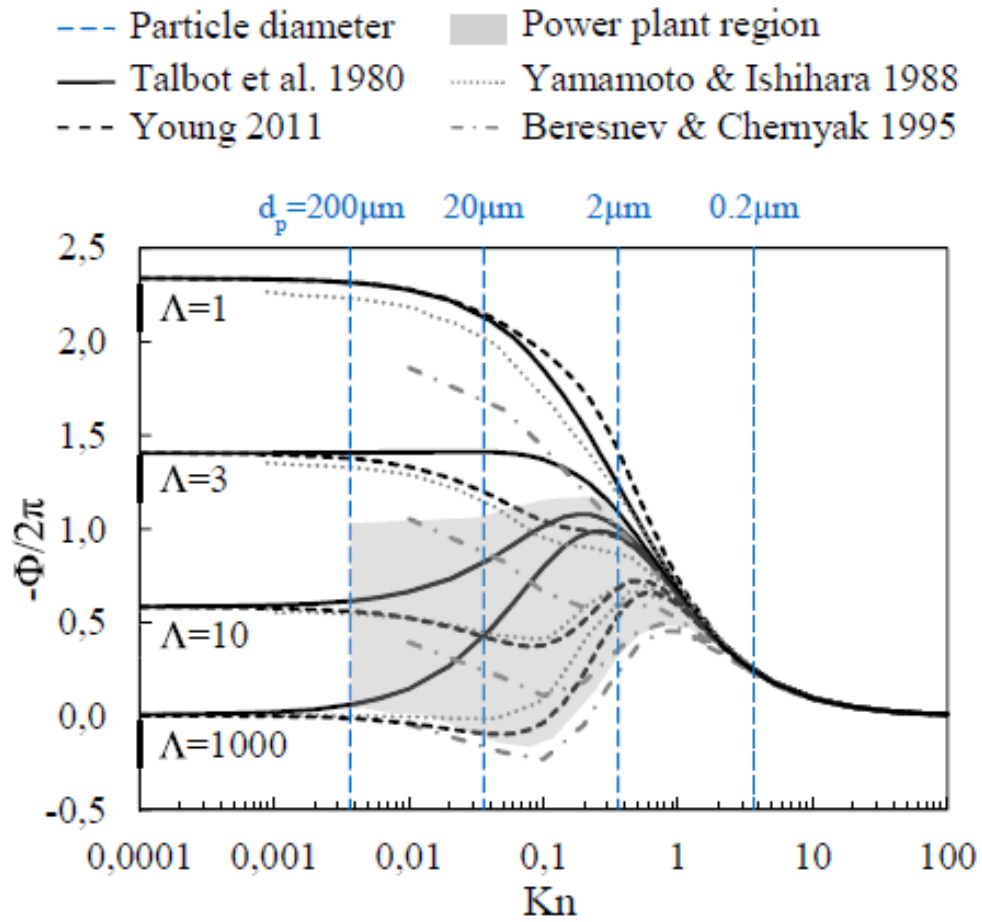


Figure 2.18: The expression of equation 2.36 for typical particle diameters and Kn numbers found in power plants, computed for $T_g = 1000^\circ\text{C}$. Retrieved from U.S. Kleinhans (2015)

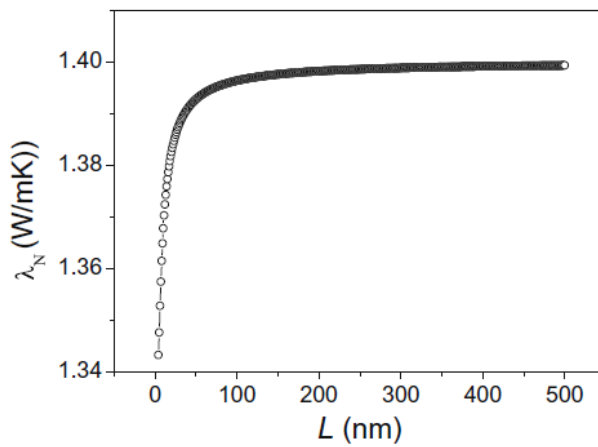


Figure 2.19: Thermal conductivity of amorphous silica nanoparticles with smooth surfaces ($p=1$), varying with particle size (eg. diameter), as presented in Gao and Jelle (2019).

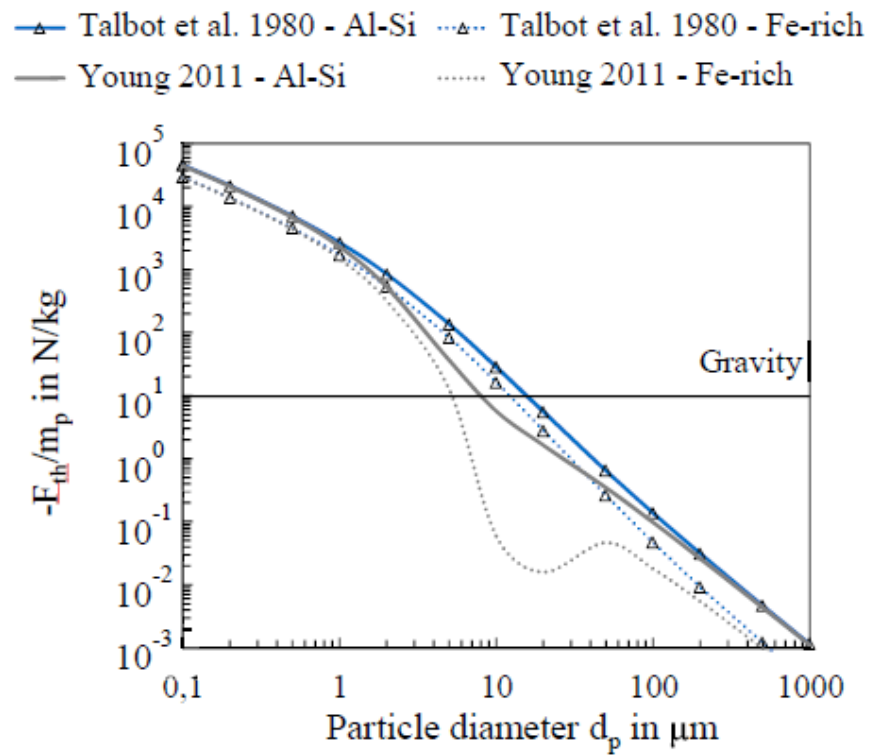


Figure 2.20: Thermophoretic force as a function of particle diameter, in comparison with data from Talbot et al. (1980) and Young (2011).

2.2.4 Lift

Saffman (1964) introduces the effects of lift force caused by shear flow onto spherical particles. A short description: The higher velocity across the particle surface causes a pressure drop, yielding momentum onto the particle, its direction proportional to the positive velocity gradient.

Zheng and Silber-Li (2009) presents empirical data for lift forces influencing nanoparticle concentration close to wall in a low-Re flow. The resulting distribution of particle concentration hints to lift force driving the majority of particles into the free flow region when no other forces are considered. As the effect of lift force onto particles act as drag, larger particles will experience a larger impact.

$$F_L = K\mu V r^2 \left(\frac{\dot{\gamma}}{\nu}\right)^{\frac{1}{2}} \quad (2.37)$$

, where $K = 81.2$, $V = u_f - u_p$ is relative velocity, $\dot{\gamma}$ is the shear rate.

While data provided by Zheng and Silber-Li (2009) isolates the lift force, the fraction of the lift force effect in a turbulent channel flow is negligible for nanoparticles.

2.2.5 Particle deposition description

As the simulation is considered steady flow, a deposition rate must be determined without use of time-parameters. Kallio and Reeks (1989) presents a most useful definition of dimensionless deposition velocity for a 2D channel flow:

$$V_d^+ = \frac{hU_{avg}}{2u_*\Delta x} \log \frac{N_{inn}}{N_{out}} \quad (2.38)$$

, where h is the channel height, Δx is the channel increment and N_{inn} and N_{out} is the particle number at the inlet and outlet of the increment, respectively.

Tandberg (2017) derives the function with that of a simple model for deposition flux from Esptein (1983):

$$G_p = V_d(\overline{C_b} - C_w) \quad (2.39)$$

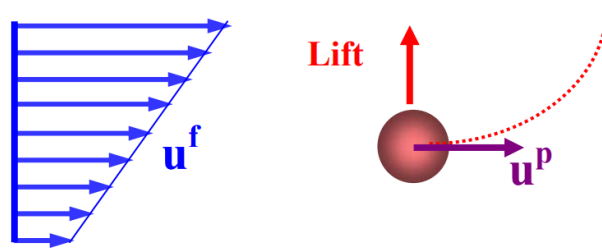


Figure 2.21: A particle in a shear flow experiences shear lift (Saffman, 1964)

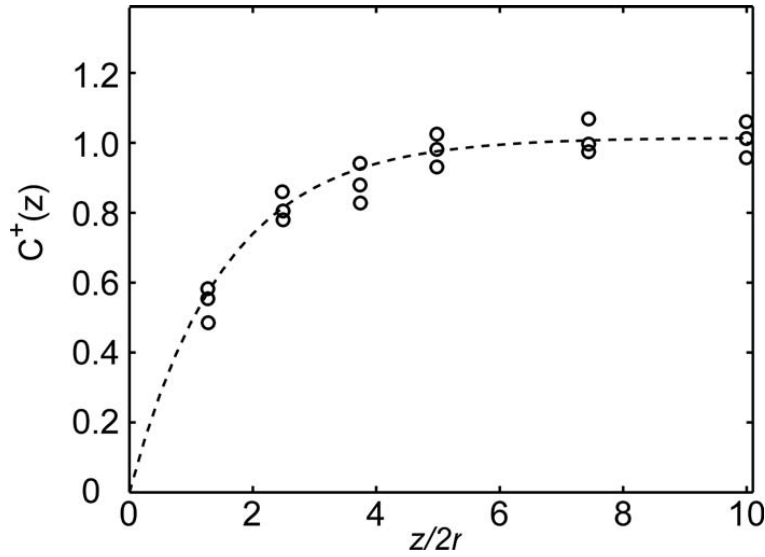


Figure 2.22: 200 nm particle concentration distribution close to wall. empirical data from Zheng and Silber-Li (2009).

, where \bar{C}_b and C_w are particle concentrations in bulk flow and on surface wall, respectively, deposition velocity defined as the ratio of concentration flux over average concentration throughout the flow. By assuming zero concentration at wall, the equation is reduced to $G_p = V_d \bar{C}_b$.

By considering an increment of a steady flow channel, the relation

$$\frac{A}{O} \frac{d\dot{m}_p''}{dx} = -G_p = -V_d \bar{C}_b \quad (2.40)$$

, where A and O is cross sectional area and perimeter of channel, respectively, while \dot{m}_p'' is the particle mass flux.

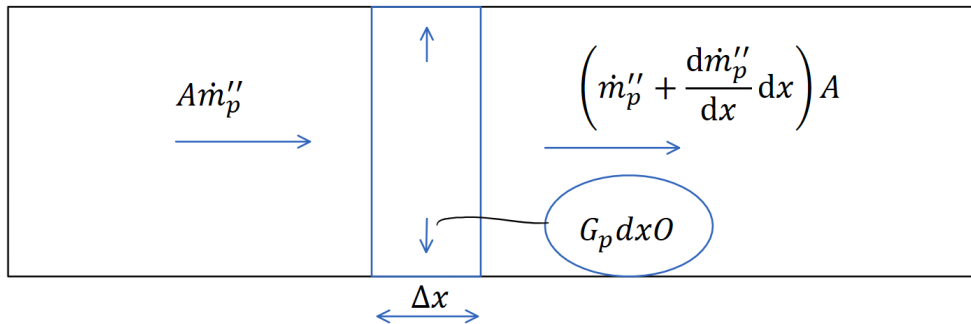


Figure 2.23: Mass transfer over an increment of a pipe can be integrated across the entire pipe length to represent the deposition velocity of the entire pipe flow. Sketch inspired by Tandberg (2017).

$$V_d = \frac{AU_{avg}}{O\Delta x} \log \frac{N_{inn}}{N_{out}} \quad (2.41)$$

Two-dimensional channel can be assumed for a channel of infinite width, which reduces the area to perimeter ratio to $\frac{A}{O} = \frac{h}{2}$.

2.2.6 Deposition predictions

Earlier experiments from studies by Liu and Agarwal (1974) and Papavergos and Hedley (1984) depict particle deposition for larger particles, non-dimensional.

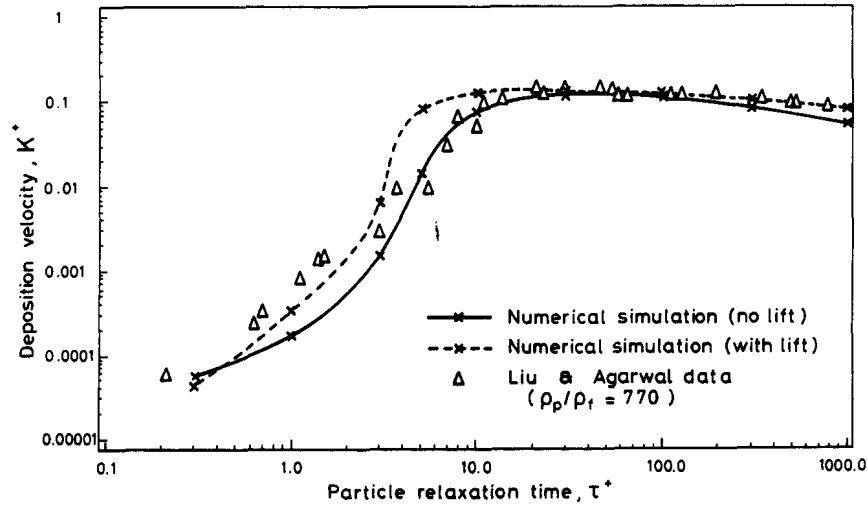


Figure 2.24: Comparison of numerical predictions with Liu and Agarwal (1974) experimental deposition velocity data as a function of particle relaxation time.

2.2.7 Electrostatic forces

Due to the structure of colloidal silica, the particles have a negative surface charge. This aids in stabilizing the particles in free stream, but also resists particle collision and film building, meaning this negative attraction must be overcome in order to achieve silica fouling.

Hesketh (1977) presents an equation for particle surface charge for smaller particles.

$$q_{max} = 2000 \times (1.6 \times 10^{-19}) \left(\frac{r}{10^{-6}} \right)^2. \quad (2.42)$$

Electrostatic surface charges will by itself repulse silica colloids from one another. As hinted to in chapter 2.1.1, the charges can be decreased by alteration of pH-levels and / or interaction of metal particles (Fe) and saline particles (NaCl). As smaller particles have low inertia, which would dominate such forces, electrostatics bears a stronger impact on deposition rates for nanoparticles. It is suspected by the author that the largest factor of these surface charges lie in the sticking probability of colloidal silica onto silica film. Due to relatively complex models necessary for accounting for this interaction, electrostatic forces are not accounted for in the deposition simulations of this study.

2.2.8 Empirical formulae

There have been several attempts at an empirical formula which can accurately predict deposition velocity based on experimental data.

The earliest still in use is presented by Papavergos and Hedley (1984), which is based on an assortment of empirical data from previous experiments.

The formula only accounts for the dominating effects in each of the regions as discussed earlier, where the region below $\tau_p^+ = 0.2$ is governed by the mass diffusion and the inertial region only governed inertial relaxation time.

$$\begin{aligned} V_d^+ &= 0.18 & \tau_p^+ > 20 \\ V_d^+ &= 3.5 * 10^{-4} \tau_p^{+2} & 0.2 < \tau_p^+ < 20 \\ V_d^+ &= 0.065 * S_c^{-\frac{2}{3}} & \tau_p^+ < 0.2 \end{aligned} \quad (2.43)$$

, where the diffusion region is negatively proportional the Schmidt number, the ratio of momentum diffusivity (kinematic viscosity) and mass diffusivity for the fluid.

Ahmadi (1994) presents a more detailed formula, adding the effects of gravity if present:

$$u_d^+ = \begin{cases} 0.084 S_c^{-\frac{2}{3}} + \frac{1}{2} \left[\frac{(0.64 \kappa^+ + \frac{1}{2} D_p^+)^2 + \frac{\tau_p^+ g^+ L_1^+}{0.01085(1 + \tau_p^{+2} L_1^+)}}{3.42 + (\tau_p^{+2} g^+ L_1^+) / (0.01085(1 + \tau_p^{+2} L_1^+))} \right]^{\frac{1}{1 + \tau_p^{+2} L_1^+}} & \text{if } u_d^+ < 0.14 \\ \times [1 + 8 \exp -(\tau_p^+ - 10)^2 / 32] \frac{0.037}{1 - \tau_p^{+2} L_1^+ (1 + (g^+ / 0.037))} & \\ 0.14 & \text{Otherwise} \end{cases} \quad (2.44)$$

Here, $L_1^+ = \frac{3.08 * \rho_f}{\rho_p * D_p^+}$ and $g^+ = \frac{\nu}{u_\tau^3}$. The dimensionless particle diameter D_p^+ is determined with the ratio of shear velocity and dynamic fluid viscosity:

$$D_p^+ = D_p * \frac{u_*}{\mu} \quad (2.45)$$

The dimensionless gravity is similarly defined:

$$g^+ = g * \frac{\nu}{u_*^3} \quad (2.46)$$

κ^+ is the dimensionless surface roughness. Without exact properties of the geothermal well pipe, smooth surface is assumed, setting the roughness to zero.

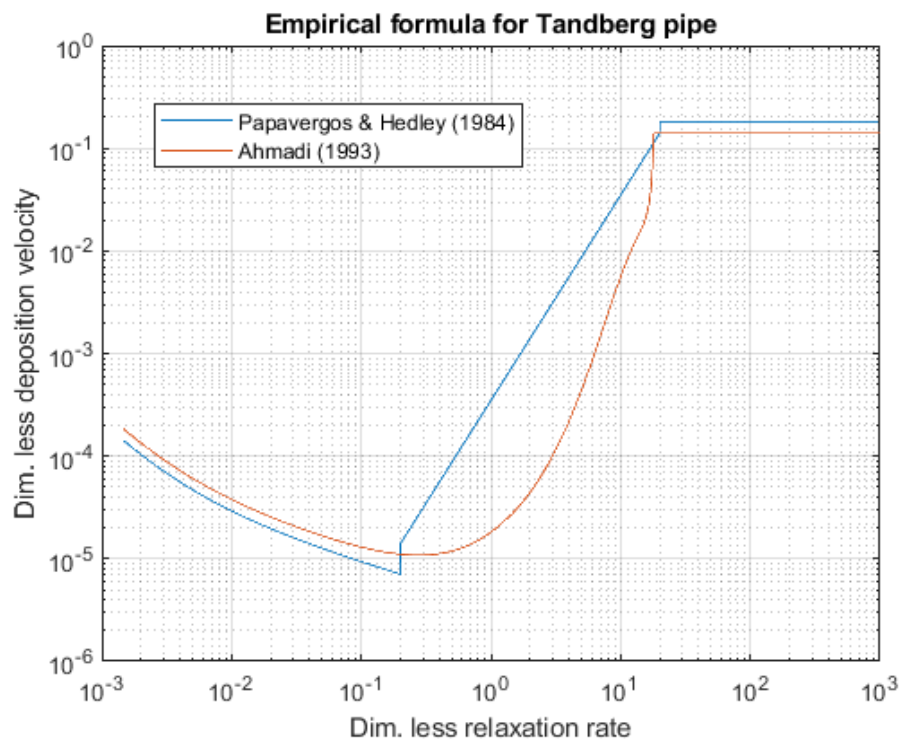


Figure 2.25: The empirical formula of Ahmadi (1994) has a more complex computation of deposition velocity in 1st and 2nd region of relaxation time, which results in a more realistic plot in comparison to that of Papavergos and Hedley (1984).

3. Theory: Flow simulation & Particle tracking

In order to predict fouling in a typical steam well pipe, the deposition theory presented in 2 will be implemented in OpenFOAM in order to create a numerical simulation, so that to simulate the gradual fouling of cylinder walls.

Numerical simulation of particles in turbulent flows is widely researched, and numerous solutions have been created and published for further use. Stability of simulation becomes challenging when considering incompressible, turbulent flows. The codes often limit the specifics of different effects such as Brownian diffusion and thermophoresis. Two prominent papers for the current scenario is given by Tian and Ahmadi (2006) and Chauhan (2019). Each of these papers document the tracking of particles onto surfaces from turbulent gas flows, where one uses the numerical program OpenFOAM and the other uses ANSYS Fluent. These two programs have very different structure, and both will be evaluated for this study.

3.1 Comparison of software

3.1.1 OpenFOAM

OpenFOAM is an open source software numerical simulator. The open source feature makes this program much more widespread than other subscription programs like Matlab and ANSYS Fluent, and as users themselves make and distribute the different solvers and codes for the software, it has a much larger solver library than that of other software. This allows for much more specific solvers which prioritizes different criteria and effects that are important to the simulation. While the library is larger than other programs, this also means that many of the solvers have little to no support or examples other than what is provided by the OpenFOAM community. This makes the experience with the program critical in order to compare the solvers and correctly set up the wanted simulation. Furthermore, despite the large library, more complex CFD codes take a longer time to be implemented, in part due to software like ANSYS Fluent being tailored for CFD, leading more research and software development to be conducted for ANSYS.

OpenFOAM has no initial graphical menu, and so any generated models to be used in deposition simulations must be read by a third party program in order to be viewed. This makes it more difficult to continually check your model or simulation while tweaking your code.

3.1.2 ANSYS Fluent

ANSYS Fluent is the fluid dynamics specified simulator program provided by ANSYS, EDRMedeso TM. This program is a combination of modeling, simulation and display of

flow simulations in and around meshed objects, and comes equipped with detailed menus for choice of fluid characteristics, surrounding factors and data input and output.

The advanced display module allows for easy 3D modelling meshing of complex geometries, as well as allowing for constant feedback from the simulation while running it. This user-friendly display module allows for easy meshing of any figure. It also becomes easy to refine mesh grids at any locations for more accurate simulations, for example close to walls or bends in channels.

As this software is subscription based, access is limited, but many universities and companies utilize the software due to dedicated support and custom tailored interface for CFD-analysis.

3.2 Numerical turbulence modeling

Turbulent flow simulations are, by the nature of turbulent internal flow, never 100 % correct. AS explained in chapter 2, the flow changes from turbulent to nearly laminar close to the wall, and the mixed region in between is difficult to accurately predict.

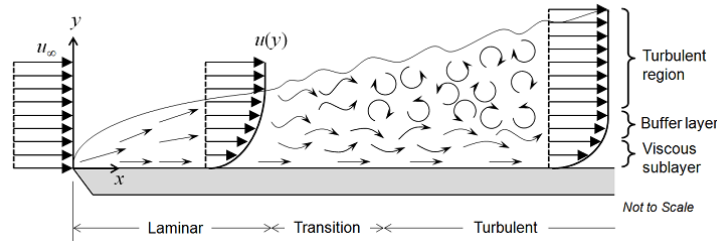


Figure 3.1: The viscous sublayer is proportional to Reynolds number, decreasing with increasing Re . Figure from Mills (2001).

This section can be attempted predicted in two different ways, either by integrating the turbulence model for internal flow all the way onto the wall or by implementing wall functions to solve the flow between the no-slip wall and the fully turbulent region.

3.3 Turbulence models & wall functions

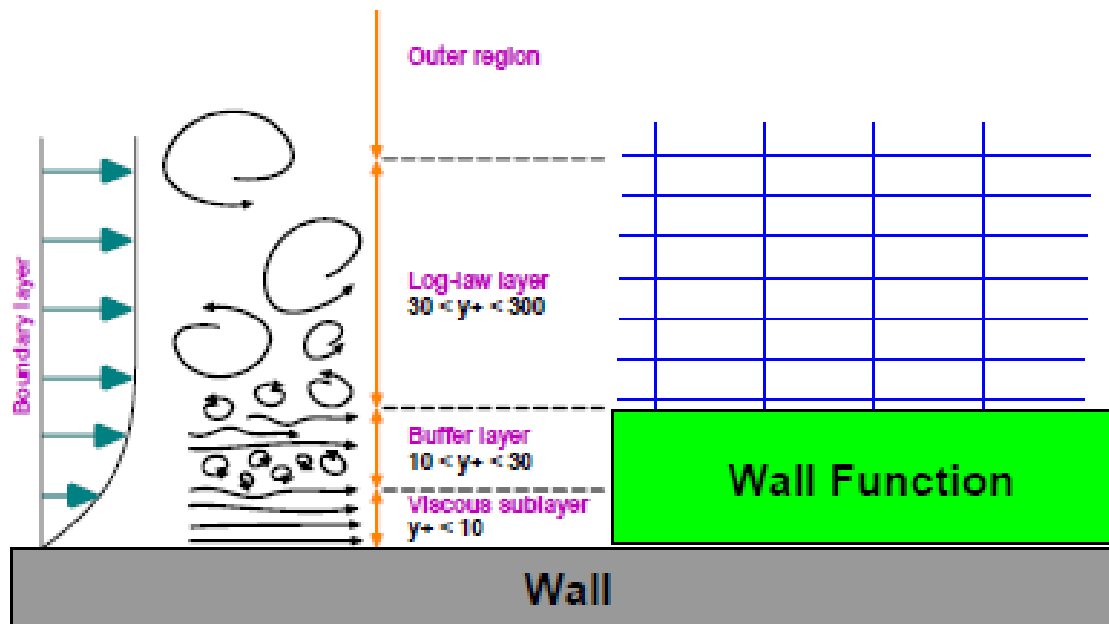
The importance of turbophoresis makes direct numerical simulation very attractive for the computation of particle deposition, as the dependencies of eddies directing larger colloidal silica particles towards the wall is a key factor in particulate deposition rates. This will naturally require simulation in 3D, as all spatial scales of turbulence must be computed in order to be a realistic representation. In order to do so, the resolution requirements states that the number of points N in a mesh-direction of a certain increment must be larger than the integral scale for turbulence. Compensating for three dimensions results in a requirement of:

$$N^3 > Re^{\frac{9}{4}}, \quad (3.1)$$

according to Orzag (1970)

Thus, necessary resolution drastically increases with the Reynolds number of the flow, leaving the method unpractical for large simulations with high Reynolds numbers.

The goal of wall functions is to adequately interpret incoming flow and predict the outcome of turbulent stresses on mass, momentum and energy transfer. This will spare the simulation of processing time needed to directly simulate turbulence for each cell in this region.



Wall-functions (high-RE)

Figure 3.2: This principle sketch from Guerrero (2019) shows what section of the mesh is no longer simulated when using a wall function.

The turbulence models previously utilized for particle deposition include but are not limited to:

- Standard $\kappa - \epsilon$ method
- $\kappa - \omega$ method
- Shear-stress transport (SST) $\kappa - \omega$ method
- Reynolds' stress method (RSM)

For the present study, the SST $\kappa - \omega$ method and RSM method will be considered, their advantages and disadvantages discussed. These models have been elected on the basis of the works of Tian and Ahmadi (2006), Tandberg (2017) and Franziska Greifzu (2015). And for initial simulations of particle deposition their results will be compared for recommendation for future use.

3.3.1 RANS-equation solution method

In simulating particle deposition, computation of fluid motion is done by solving the Navier-Stokes equation. As explained previously, direct simulation of the equation becomes exponentially more costly. Therefore, practical computation of NS-equation uses certain simplifications in order to diminish the computational cost. The most common method for simplifying direct numerical simulation is time-averaging components of the NS-equation into a mean (time-averaged) component and a fluctuating component, as in:

$$u = \bar{u} + u' \quad (3.2)$$

, where \bar{u} is the mean velocity and u' is the fluctuating velocity.

This develops the instantaneous NS-equation into the Reynolds-averaged NS-equation.

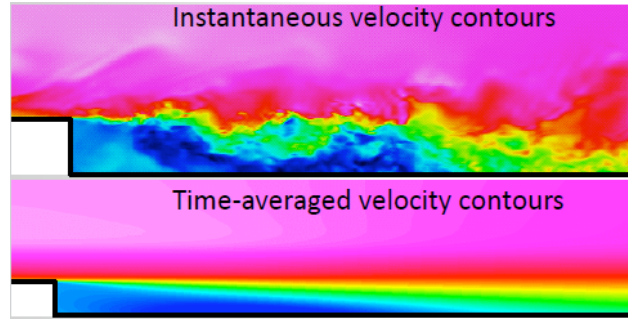


Figure 3.3: Example of how time-averaged velocity and intensity of turbulent fluctuations will be depicted in ANSYS. (ANSYS, 2014)

All turbulence models have as goal to solve the RANS-equation, their differences lying in the approach in which it is solved.

$$\frac{\partial \rho}{\partial t} + \frac{\partial(\rho u_i)}{\partial x_i} = 0 \quad (3.3)$$

$$\frac{\partial(\rho u_i)}{\partial t} + \frac{\partial[\rho u_i u_j]}{\partial x_j} = -\frac{\partial p}{\partial x_i} + \frac{\partial \tau_{ij}}{\partial x_j} + \rho f_i \quad (3.4)$$

$$\frac{\partial(\rho e)}{\partial t} + (\rho e + p) \frac{\partial u_i}{\partial x_i} = \frac{\partial(\tau_{ij} u_j)}{\partial x_i} + \rho f_i u_i + \frac{\partial(\dot{q}_i)}{\partial x_i} + r \quad (3.5)$$

Equation 3.3, 3.4 and 3.5 represent the continuity, momentum and energy equation, respectively.

The stresses τ_{ij} of equation 3.4 represent the Reynolds stress tensor $Re_{ij} = -\overline{\rho u'_i u'_j}$. There are two ways in which this stress tensor can be resolved. Firstly it can be directly solved via transport equations, in where certain spatial dependent stresses such as pressure strain ϕ_{ij} must be modeled in order to predict the stress direction. While still considering such variables as time-averaged, the directional stresses provides an advantage when simulating

for complex geometries or strong swirl. The RSM method solves the RANS-equations in this manner.

$$\begin{aligned}
& \frac{\partial}{\partial t}(\overline{\rho u'_i u'_j}) + \frac{\partial}{\partial x_k}(\overline{\rho u_k u'_i u'_j}) = -\frac{\partial}{\partial x_k}[\overline{\rho u'_i u'_j u'_k} + \overline{p(\delta_{kj} u'_i + \delta_{ik} u'_j)}] \\
& + \frac{\partial}{\partial x_k}[\mu \frac{\partial}{\partial x_k}(\overline{u'_i u'_j})] - \rho(\overline{u'_i u'_k} \frac{\partial u_j}{\partial x_k} + \overline{u'_j u'_k} \frac{\partial u_i}{\partial x_k}) - \rho\beta(\overline{g_i u'_j \phi} + \overline{g_j u'_i \phi}) \\
& + p(\frac{\partial u'_i}{\partial x_j} + \frac{\partial u'_j}{\partial x_i}) - 2\mu \frac{\partial u'_i}{\partial x_k} \frac{\partial u'_j}{\partial x_k} - 2\rho\Omega_k(\overline{u'_j u'_m \varepsilon_{ikm}} + \overline{u'_i u'_m \varepsilon_{jkm}}) + S
\end{aligned} \tag{3.6}$$

This equation can be suppressed into holding an Reynolds stress production term, diffusive term, dissipation term and a pressure-strain correlation. For full implementation into FLUENT, the reader is referred to the theory guide of ANSYS [®] (2019).

Another option is to model the stresses with a turbulent viscosity μ_T , which only requires two equations, that of turbulent kinetic energy κ and of either turbulent dissipation rate ϵ or specific dissipation rate ω . Solving the two transport equations offers no directional stresses, yielding the method less suitable for advanced flows or complex geometries, but the method has held an adequate standard for simple flow simulations when investigating standard anomalies such as convection and flow separation.

$$\frac{\partial}{\partial t}(\rho\kappa) + \frac{\partial}{\partial x_i}(\rho\kappa u_i) = \frac{\partial}{\partial x_j}(\Gamma_\kappa \frac{\partial \kappa}{\partial x_j}) + \tilde{G}_\kappa - Y_\kappa + S_\kappa \tag{3.7}$$

$$\frac{\partial}{\partial t}(\rho\omega) + \frac{\partial}{\partial x_i}(\rho\omega u_i) = \frac{\partial}{\partial x_j}(\Gamma_\omega \frac{\partial \omega}{\partial x_j}) + G_\omega - Y_\omega + D_\omega + S_\omega \tag{3.8}$$

3.4 Particle deposition modeling

There exist a plethora of methods for simulating particle flow in fluent, as the nature of suspended particle flow varies greatly with both intensive and extensive properties of the particles. For example, condensation clouds within pipe flow might hardly affect the bulk fluid flow, while high density particles above a certain size can disrupt and hamper bulk fluid flow.

Simplification of near wall simulation is recommended as often as possible. It is therefore possible and indeed advisable to begin deposition modeling of particles onto the surface wall with the built-in method from ANSYS, that is, selecting a trap boundary condition for the channel walls.

3.4.1 Attachment and re-suspension

Particle interaction with a wall and with each other is complicated to execute properly in a numerical model. Of the mechanisms listed in 2, not all are formally available for particle

physics in single phase modeling, either by not being optional for turbulent steady flow, or by not being introduced at all. Features like Brownian diffusion and wall surface roughness must be introduced externally in turbulent steady flow in order to function properly in the simulation.

These mechanisms must be implemented through user defined functions (UDF). These functions will compute a value for whatever variable is desired based on values retrieved from the FLUENT simulation, and will then feed the value back into the suitable cell. For the simulation of the scenario from Tandberg (2017), UDFs from that papers Appendix was retrieved and put to use. The UDFs are presented in the appendix, with the ones retrieved from Tandberg (2017) pointed out. The rest are formed by the author.

A question arises when the simulated particle reaches a surface cell in how the particle will react to the surface. As proven by Gao and Jelle (2019), a silica particle reaching the wall surface in a superheated pipe will nearly always attach itself, leading to complete surface wall coverage in a short amount of time. Any subsequent particle deposition will then become an interaction between single particles and particle film. The issue is further complicated by other particles affecting the surface charge and structure of the agglomerated silica colloids. To account for these factors will require complex particle-particle interaction, which is processor heavy and time consuming, and beyond the scopes of this study. A simplified solution to this would be to compute an attachment ratio and feed that into a depositoin simulation with a UDF. Based on Kemia and Landsvirkjun (2019), the deposited silica shows clear size distribution intermingled with other elements such as iron or salts, rendering uniform simulations of a single particle inaccurate. However, as inter-molecular reactions between nano-particles is impractical to simulate for the given case, uniform particle tracking will have to remain adequate.

In support of this practice is the mentioned stability of colloidal silica particles, which once the saturation in the solution has sufficiently decreased, will remain stable and therefore not interact with other precipitated silica in free stream, justifying the simplification of no particle-particle interaction in the stream. This statement is supported by the Brown (2011), as the deposited silica layer consists of linked but independent particles of various size and shape.

Having described several mechanisms that numerical simulations must neglect for the sake of practicality, an examination of the most relevant simulations for the given scenario will be given, highlighting potential assumptions and errors which can have affected the results of said simulation.

3.4.2 Chauhan

In light of the findings from the Krafla test well, PhD Chauhan (2019) attempts to explain the severe silica fouling of the IDDP-1 test well.

Chauhan (2019) performs numerical simulations of silica deposition using OpenFOAM and compares these results with deposition results from a laboratory experiment. The data is then compared to empirical formulae from Papavergos and Hedley (1984) and Ahmadi (1994)

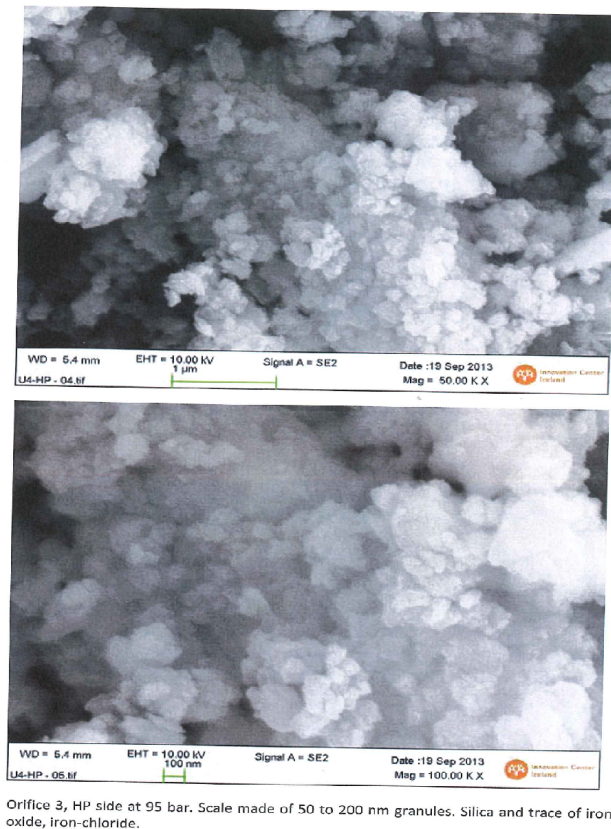


Figure 3.4: Microscopic analysis made of the exploratory geothermal well at IDDP-1, provided by Kemia and Landsvirkjun (2019).

in order to validate the simulation method and experimental setup..

Initially, Chauhan (2019) starts by presenting a size distribution for amorphous silica for different pressure and temperature, reasoning that simulations at a determined pressure and temperature should be conducted with the matching particle diameter. His source for the size distribution is based on solubility studies by Pavel Karasek (2013) for fused silica. An alternative study on the solubility of amorphous silica has been conducted by Plyasunov (2012). The resulting deposition velocity diagram is compared to empirical data by Liu and Agarwal (1974).

The comparison reveals a large diversion in the 1st and 2nd regime of particle relaxation time (approximately between τ^+ of 0.1 and 4.). At the most, the deposition velocity diverges with 10^2 .

Chauhan (2019) assumes complete absorption of particles at the wall, which will result in optimal deposition velocity. The validity of this statement should be questioned due to the composition of a geothermal steam flow, but without any clear empirical data for the effect of different content in the geothermal steam, such as iron or different pH on the agglomeration and deposition of colloidal silica, such effects on the sticking probability for the pipe flow scenario cannot be accurately estimated.

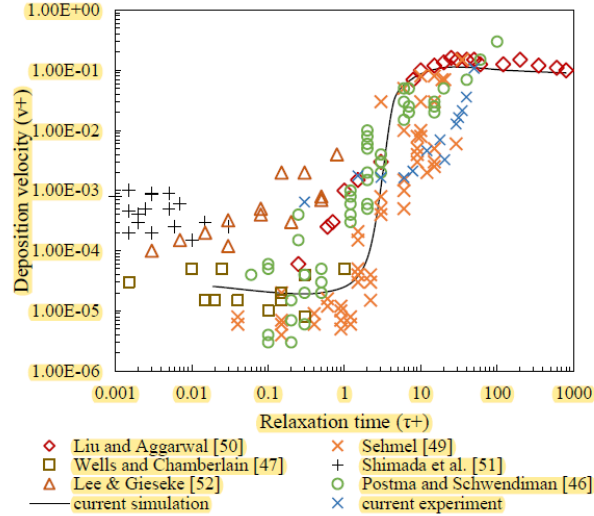


Figure 3.5: The simulated deposition velocity for silica in superheated steam by Chauhan (2019) is compared to particle deposition in air by Liu and Agarwal (1974)

A transient 2D flow simulation was conducted at different particle relaxation times and the resulting concentration profiles were displayed as results.

The resulting 2D simulation shows a clear peak in particle concentration at walls for particle relaxation times of the second regime. While the larger particles shows a high deposition velocity when looking at the results at 3.5, the low wall deposition can be explained by the high inertia of the particles making the turbulent diffusion ineffective in transferring them towards the wall. Chauhan (2019) explains that the larger concentration of such particles in the middle of the stream is due to lift force being the most effective convective mechanism onto the silica particles, in which the higher velocity of the center stream lifts the particles away from the no-slip wall. Theory by Guha (2008) supports this explanation.

The main concerns from Chauhan (2019) can be summarized as:

- Chauhan (2019) does not add the Cunningham correction factor to the particle relaxation factor, and does therefore not account for the rarefied gas effect, an important factor for sub-micron particles..
- A uniform particle size through each simulation, which is not realistic in a geothermal well stream. Difficulties in simulating with different sized particles should be addressed.
- Attachment rate of 1 neglects effects of electrostatic forces between particles and film. Additionally no re-entrainment method of probability was discussed, which would be of importance when discussing potential de-fouling of the pipe walls.
- Thermophoretic force is not accounted for in particle motion.
- Assumption of one-way coupling removes any effects for particle-particle interaction during flow simulations.

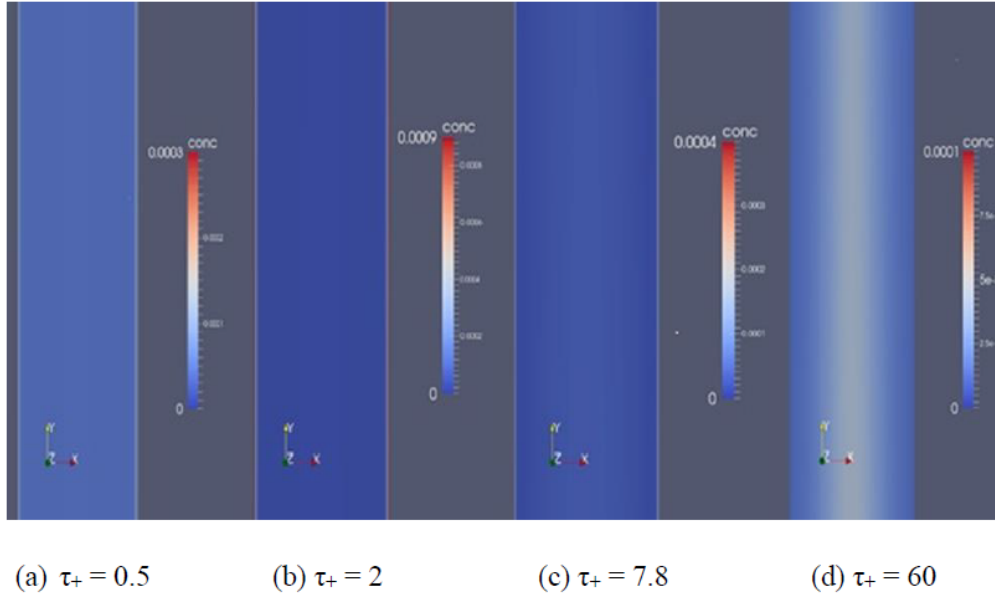


Figure 3.6: Particle concentrations at respective relaxation times. The largest particles display the lowest concentration at the walls despite having the highest deposition velocity.

A larger problem regarding the fouling experiment of Chauhan is using pre-precipitated colloidal silica particles injected into flow stream as the only concentration of silica. While this method ensures a specific parameter for particle size distribution, it also neglects the precipitation process effect on particle morphology and particle properties. The continued presence of silica condensation in the free stream is, as explained in 2, crucial for both the stability of colloidal silica and the sticking probability of such colloids onto silica "film" with similar negative surface charge.

3.4.3 Tandberg

The multitude of effects involved in particle deposition at different levels of viscosity has made accurately predicting fouling a very challenging practise. Additionally, the multiphase nature of the growing fouling film / layer will add to the complexity of any simulation or model.

In the Tandberg (2017) thesis, an attempt was made to find a compromise between deposition through particle tracking in flow simulations and theoretical deposition models for given flow conditions. His method involved simulating the turbulent flow of a fluid over a flat plate, using discrete phase modeling to track particles through the free stream region and down to the diffusive layer of the near-wall region. Here, data of the forces and motions of fluid and particles at the wall boundary was transferred by user defined functions from the simulation program (in this case ANSYS) to be read by MATLAB, where rates of attachment, rebound and re-surfacing was computed and matched with the number of particles in contact with the boundary. This resulted in a computed deposition rate which partly agrees with previous literature and empirical data on dimensionless deposition velocity.

By initially simulating for pipe flow, Tandberg (2017) elected the $k - \omega$ SST and RSM

turbulence models as candidates for particle deposition simulations.

The simulation of turbulent flow with use of wall models will never be completely accurate, but will often be of satisfying enough for studies of heat transfer through pipe flow.

However, in this case the most noticeable effects in determining particle deposition is turbophoresis and thermophoresis, as proven by Tandberg (2017) and Guha (1997).

The choice of inlet velocity ensures turbulence, and for larger particles will be substantial enough to allow for larger particles to distribute along a wide range of particle relaxation rates.

Plyasunov (2012) suggests that the largest silica particles to be expected in the IDDP2-well will have a diameter of 100 nm. Electing such a size parameter into equation 2.6 and 2.10 results in rates as low as $\tau^+ = 10^{-9}$ for a simulation similar to that of Tandberg (2017). Such low rates have no empirical data, and it is doubtful that current theory corresponds to such parameters. Therefore, higher velocity is implemented in order to elate the relaxation rate to more suitable parameters.

The adapted model is analysed with the empirical deposition equation from Papavergos and Hedley (1984), particles simulating silica particles of size parameter $5 * 10^{-8}$ to $2.5 * 10^{-5}$, resulting in a relaxation rate parameter of 0.04 to 10^3 .

3.5 Model comparison

Validation of the turbulence models used in pipe flow simulation is best achieved by comparing results of simulations of the same setup with different turbulence models. Correlating results will testify to correct simulation of physics while divergence will signify errors and ineptitude of the models. By comparing the dimensionless velocity profile for the different turbulence model simulations under equal conditions, the correlation to DNS parameters (Tian and Ahmadi, 2006) will determine which model to progress with further.

The law of the wall is used to express the dimensionless velocity profiles.

$$u^+ = \frac{1}{k} \ln y^+ + C^+ \quad (3.9)$$

, with

$$y^+ = \frac{yu_\tau}{\nu}, \quad u_\tau = \sqrt{\frac{\tau_\omega}{\rho}}, \quad u^+ = \frac{u}{u_\tau}$$

, where u_τ is the shear velocity provided from

$$u_\tau = \sqrt{\frac{\tau_\omega}{\rho_f}} \quad (3.10)$$

, where the shear stress

$$\tau_{\omega} = \mu \left(\frac{\partial u}{\partial dy} \right)_{y=0} \quad (3.11)$$

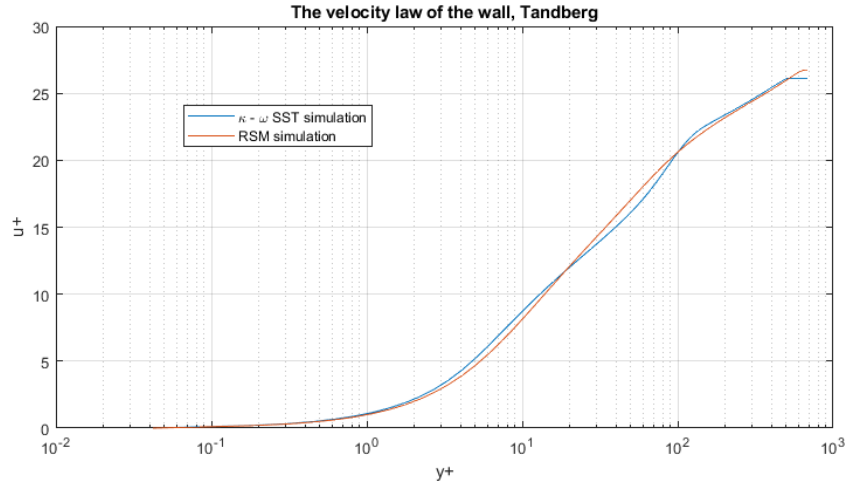


Figure 3.7: Dimensionless velocity profile close to wall of the two turbulence models when simulated for the conditions of the Tandberg (2017) thesis.

As figure 3.7 shows, both the RSM- and SST-method show good correlation with that of Coles' parameters with DNS-simulations (Tian and Ahmadi, 2006). This promises well for deposition effects to be simulated of particle deposition. Further on, the velocity profiles deviate from DNS, the RSM-method over-estimating the velocity while the SST-method underestimates the velocity. While the deviation only becomes measurable late in the buffer layer ($y^+ > 20$), this will affect the particle deposition from velocity fluctuations.

It would be in the interest of this study to simulate deposition for the highest possible fouling rate. From this disposition, the results will predict the worst-case scenario for fouling in superheated steam flows. The RSM-method is therefore initially preferable, as the over-estimation of velocity close to wall will aid the deposition velocity.

3.6 Discrete Phase Model

Tracking particle deposition in ANSYS is made simple with a tool known as "Discrete Phase Model". ANSYS (®) (2019) describes how to instill the model, and what its limitations are:

This method allows simulation of a set amount of particles to be affected by the fluid flow and with each other, provided that the volume fraction of the particles in the flow is no higher than 10 %.

By choosing an injection over a surface, the selected material is divided in a selected number of particles across the surface. Choosing of particle distribution can either be made linear or by following the Rossin-Rammler stochastic distribution, which randomizes the size distribution for each injection.

Choice of material is fetched from the ANSYS fluent database. Creating a new material will allow for the closest simulation possible to that of the colloidal silica deposition from the deep drill well. The values utilized in the constant volume flow simulations for air are identical to those used by Tandberg (2017).

Injecting the particles at a set distance into the channel, the channel walls after this section is given a UDF boundary condition which traps and logs particles when connecting to the wall. For 1 m before this boundary condition, the wall is set to reflect, such as to allow for a more natural distribution of particles in the flow before they deposit themselves onto the surface.

When modelling the discrete phase, the choice of which effects should determine the particle direction is crucial. Drag-forces should always be enabled, as this determines the initial flux of particles towards the wall surface. Thermophoretic force can be toggled on and off so as to determine the effect of the force upon the deposition velocity for different sized particles. Other forces, such as electrophoresis, can also be toggled on should they be considered anything other than negligible.

Should particle-particle interaction be necessary to compute, this must be toggled on in the DPM GUI. Initially, fluid-flow is not interacted upon with the discrete phase particles. Should the volume fraction α_p of the particles be large enough, this dependence can be toggled on in the GUI. S. Elghobashi (1994) gives a description of determining the choice of coupling scheme dependent on particle relaxation rate τ_p , Kolmogorov time scale $\tau_k = (\frac{\nu}{\epsilon})^2$ and the volume fraction of particles.

By default, ANSYS only enables brownian diffusion for sub-micron particles in a laminar flow, based on the assumption of turbophoresis dominating particle diffusion in turbulent flow. In order to activate this body force for discrete phase modelling in turbulent flow, a UDF must be introduced. Tandberg (2017) introduces the definition of Brownian diffusion as defined by Temu (1998).

The body force from brownian diffusion is defined as a product of brownian motion, absolute velocity difference and brownian diffusion similar to that of equation 2.16:

$$F_B = \frac{3C_d\rho_f}{4D_p\rho_p C_C} |\vec{u} - \vec{v}| v_B \quad (3.12)$$

Smaller particles are more difficult to track, at worst resulting in an incomplete tracking. This may be countered with an increase in tracking iterations.

There is a risk in how well current deposition theory predicts the effects of the different contributing forces onto nanoparticles. As the particles in question grow more similar in characteristics to that of molecules, many of the deposition mechanisms have not, and possibly cannot be properly measured, thus rendering further reliance on empirical deposition equations inaccurate. This is also suggested by, among others, Tandberg (2017) and Tian and Ahmadi (2006).

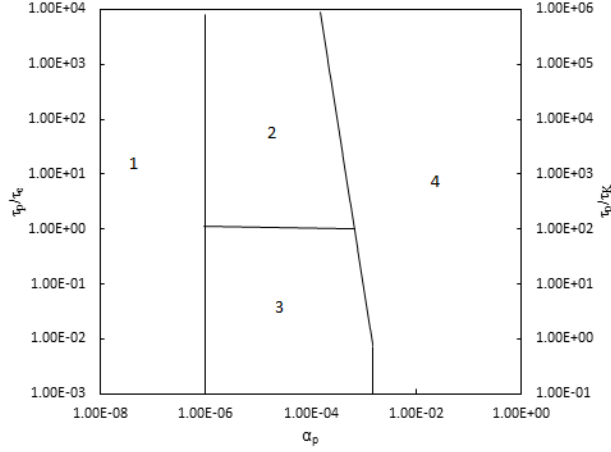


Figure 3.8: Classification of coupling schemes and interaction by S. Elghobashi (1994): (1) one-way coupling, (2) two-way coupling with particles enhance turbulence production, (3) two-way coupling with particles enhance turbulence dissipation, (4) four-way coupling.

3.6.1 Stochastic particle tracking

In order to include the effects of turbulence on particle dispersion, stochastic particle tracking must be selected for the DPM-method (ANSYS $\text{\textcircled{R}}$, 2019). This stochastic tracking (random walk) model will include the effect of instantaneous turbulent velocity fluctuations onto the particle trajectory, even while using the RANS-equation method. The value of these fluctuating velocity components are kept constant over an interval of time dependent on the characteristic lifetime of the eddies (τ_ϵ) in the flow. This time is proportional to the turbulent dissipation rate ($\omega = \frac{\kappa}{\epsilon}$) of the flow.

$$\tau_\epsilon = 2 * C_L * \omega \quad (3.13)$$

, where C_L is a constant equal to 0.15 (or 0.3 for RSM-method).

The lifetime can also be randomized by switching the above-mentioned model to

$$\tau_\epsilon = -C_L * \omega * \log r \quad (3.14)$$

, where r is a uniform random number between 0 and 1.

ANSYS $\text{\textcircled{R}}$ (2019) claims that the option of random calculation of eddy lifetime yields a more realistic description of the velocity correlation function for fluctuating velocity components, but offers little description into how or for what circumstances. An analysis of the different options revealed that the option for random eddy lifetime resulted in less correlation between simulated deposition velocities and the empirical data of Papavergos and Hedley (1984).

4. Computational alternatives

Now that the methods for fluid flow modelling and particle tracking have been presented, it remains to define the flow simulation properties and form a pipe mesh after such properties. In this chapter, the model for choosing wall cell resolution is presented. Then follows a short explanation of how UDFs are implemented into the system.

4.1 Meshing & wall cell resolution

By choosing the SST-turbulence model, simulations close to the wall takes the form of $k - \omega$. According to Guerrero (2019), this model requires a very fine resolution close to wall. Computing the dimensionless wall distance y^+ is done through the following equation:

As the RSM-turbulence method is to be evaluated, a high resolution is required to capture the motion of fluid and particles as close to the wall as desired. Guerrero (2019) explains how this criteria stems from the method of solving the stress tensors, as explained in chapter 3.3.

Guerrero (2019) goes on to describe how the initial cell distance to wall is defined by the mean velocity and viscosity of the fluid flow.

$$y^+ = \frac{\rho * U_\tau * y}{\mu}, \quad (4.1)$$

where y is the distance to the first cell center normal to the wall, ρ and μ are fluid density and dynamic viscosity, respectively, and U_τ is the friction velocity defined as

$$U_\tau = \frac{\tau_w}{\rho} \quad (4.2)$$

At the advise of ANSYS [®] (2019), high Reynolds number flow simulated with the RSM-method should be meshed with $y^+ = 1$ yo $y^+ < 1$.

In order to circumvent unnecessary processing of fluid flow, the internal pipe flow is only simulated for half of the pipe. The axis in the center of the pipe flow is then defined as an symmetric boundary, resulting in the full pipe flow being simulated by only half of the geometry. This method should prove realistic, as internal pipe flows should be identical normal to the center axis. Halving the simulation also proved more reliable approach than complete simulation. When a full geometry of pipe was simulated for turbulent flow, the resulting velocity profile became unstable, preventing the full channel simulation from being useful for particle deposition.

4.2 User defined functions and initial conditions

FLUENT cannot produce the position along a wall surface where particles have deposited themselves without the intervention of an external command. Deposited particles are simply changed from active to trapped, and DPM method no longer records its movement. In order to determine the position at which the particles are deposited, a UDF by Tandberg (2017) is presented.

In order to achieve a faster development of the turbulent velocity profile, Tandberg (2017) introduces initial conditions for velocity, temperature, turbulent kinetic energy and dissipation rate as follows:

$$\begin{aligned} V(x) &= \frac{8V_{avg}}{7} * \left(\frac{0.5h+x}{0.5h}\right)^{\frac{1}{7}} \quad \text{for } x < 0 \\ V(x) &= \frac{8V_{avg}}{7} * \left(\frac{0.5h-x}{0.5h}\right)^{\frac{1}{7}} \quad \text{for } x > 0 \end{aligned} \quad (4.3)$$

, where V_{avg} is the average flow velocity in the pipe, h is the width of the pipe channel and x is the radial distance from the center of the channel.

$$\begin{aligned} T(x) &= \frac{8(T_{avg} - T_w)}{7} * \left(\frac{0.5h+x}{0.5h}\right)^{\frac{1}{7}} + T_w \quad \text{for } x < 0 \\ T(x) &= \frac{8(T_{avg} - T_w)}{7} * \left(\frac{0.5h-x}{0.5h}\right)^{\frac{1}{7}} + T_w \quad \text{for } x > 0 \end{aligned} \quad (4.4)$$

, where T_{avg} and T_w is the average flow temperature and the channel wall temperature, respectively.

$$\begin{aligned} k(x) &= 0.002V_{avg}^2 + \frac{x}{0.5h} \left(0.002V_{avg}^2 - \frac{\tau_w}{\rho_f \sqrt{C_\mu}}\right) \quad \text{for } x < 0 \\ k(x) &= 0.002V_{avg}^2 - \frac{x}{0.5h} \left(0.002V_{avg}^2 - \frac{\tau_w}{\rho_f \sqrt{C_\mu}}\right) \quad \text{for } x > 0 \end{aligned} \quad (4.5)$$

, where τ_w, ρ_f, C_μ is wall shear stress, fluid density and turbulence model closure coefficient.

5. Results & Comparisons

5.1 Dimensionless wall distance

5.2 Setup

Particle deposition was simulated with the same input parameters as Tandberg (2017) simulations. The goal of the simulation was to evaluate the accuracy of the two potential turbulence models for particle deposition. The dimensionless deposition velocity is plotted against the dimensionless relaxation rate proportional to the particle diameter and flow Reynolds number.

Simulations performed according to the parameters used Tandberg (2017) must be meshed so that the lowest cell distance agrees with a dimensionless wall distance $y^+ < 0.1$. This criteria is to best accommodate the RSM turbulence model. Following the equations of chapter 2, a channel like the one used in Tandberg (2017) demands a first cell distance from the wall surface:

$$y = \frac{\mu * y^+}{\rho_f * U_\tau} \quad (5.1)$$

, where y^+ is set as preferred by figure 3.8.

$$y = 1.5 * 10^{-5} \quad (5.2)$$

The deposition rates of the Tandberg (2017) scenario was replicated for the zero-gravity flow without thermophoresis.

The chosen turbulence models have the following options chosen in ANSYS Fluent:

Turbulence models	$\kappa - \omega$ SST	RSM
Near-wall treatment	-	Enhanced Wall Treatment
Options	Production limiter	Wall BC from k Equations

Table 5.1

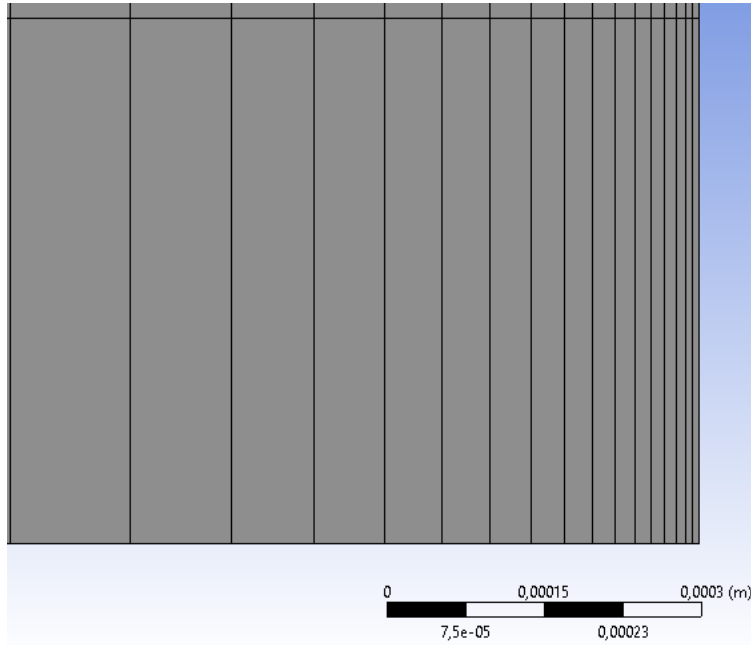


Figure 5.1: Mesh grid for the channel, the cell space growth from $1.1e - 6$.

Both turbulence models yield similar deposition velocities of particles of all relaxation rates. Choice of turbulence model can not be on the basis of best correlation to empirical data.

In order to assess the robustness of the simulation, an expanded channel is investigated using the same turbulence models. The resulting wall distance the becomes:

$$y = 1.1 * 10^{-6} \quad (5.3)$$

Pipe models were meshed for this wall distance, but the flow parameters remained similar to those used in Tandberg (2017). With an average cell size of 1 mm, the long pipe model has a cell count of 830083. The elongated pipe of 15 m is meshed in similar fashion, resulting in a cell count of 1245085.

The Long channel is modeled so that three different regions of the pipe wall can be given different boundary conditions. The purpose of this is to allow for the pipe flow to develop before introducing particles for deposition.

For the long pipe simulation, the initial 4 meters of the pipe is given a thermal boundary condition of heat flux $q'' = 0W/m^2$, allowing the flow to be fully developed. The subsequent length of pipe wall is given a constant temperature in order for the flow to develop thermally. At the same position, the particles that are to be tracked are injected linearly scattered across the pipe cross section. For the first 1 meter however, the pipe wall is not allowed to capture the particles. This has the purpose of developing the stream of particles within the flow, such that once the capture boundary condition is activated, the particles will be scattered in a more realistic way. From pipe length $L = 5m$, particulate deposition is possible.

The longer channel requires a higher velocity in order to adapt the relaxation time parameter

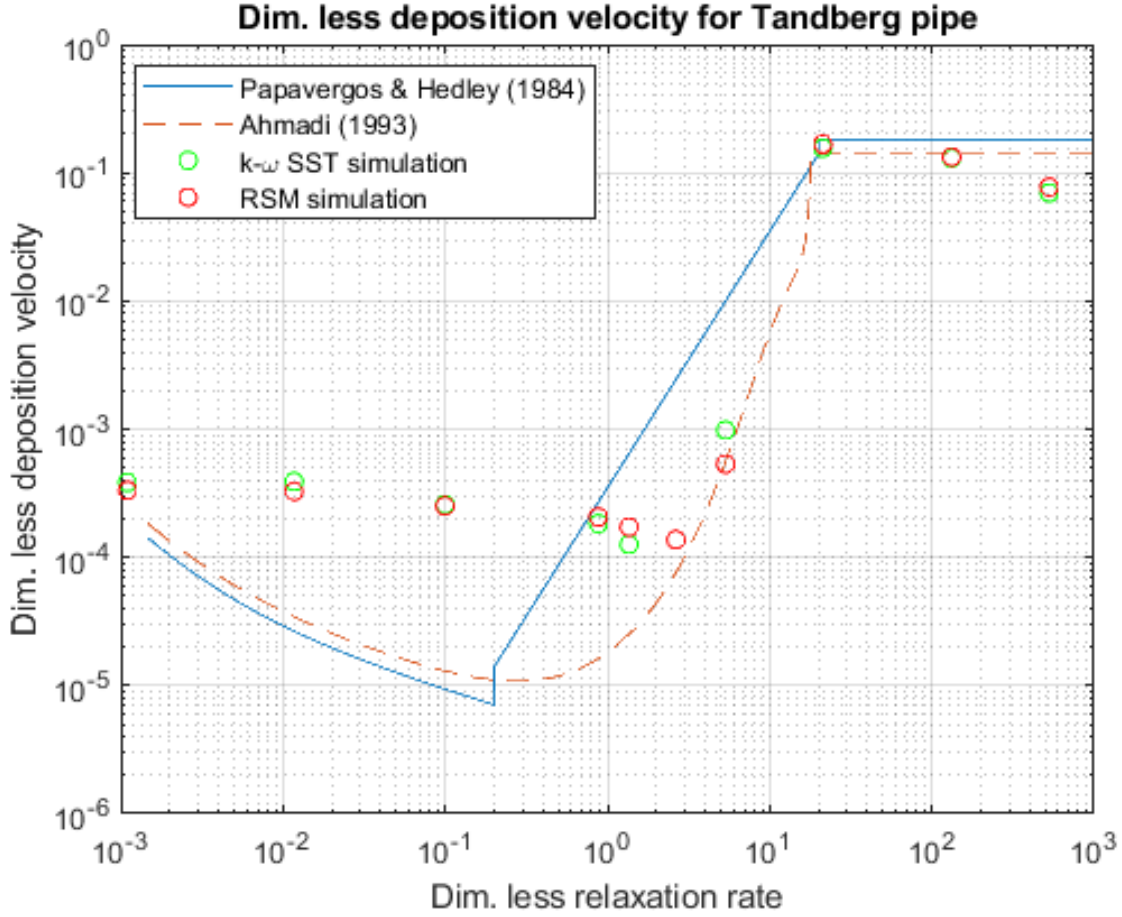


Figure 5.2: Simulation results according to the parameters of the Tandberg (2017) thesis.

to accommodate smaller particles relevant to the deposition of geothermal wells, and has therefore been given an inlet velocity of 50m/s . After development, the mean velocity at the length of particle deposition is $\sim 48\text{m s}^{-1}$. While the velocity continues to decrease along the pipe length after this, the decrease is sufficiently small to allow for this to be set as the mean velocity for the entire length of deposition, and so to be the mean velocity of the empirical formula upon comparison. The resulting flow Reynolds number is therefore:

$$Re_f = \frac{\rho_f U_{avg} D}{\mu_f} = 302518 \quad (5.4)$$

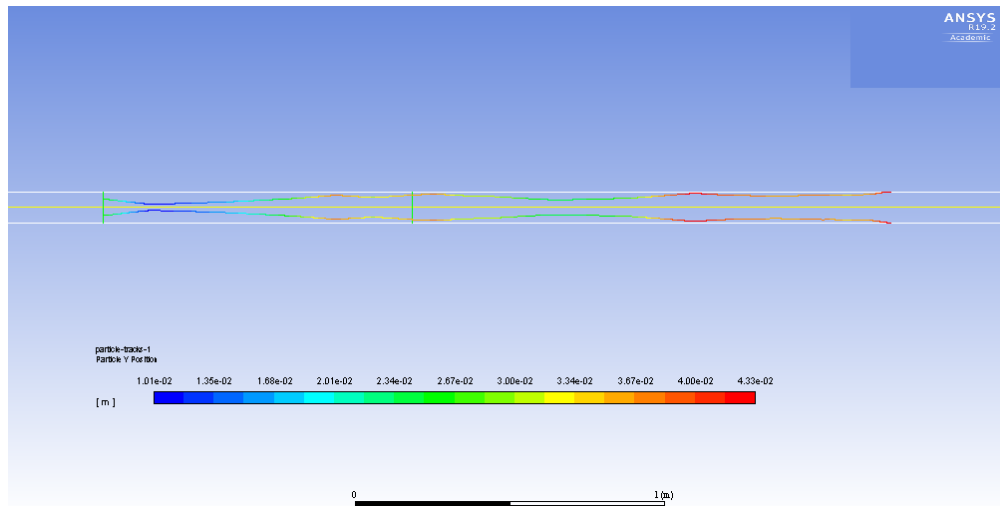


Figure 5.3: Particles are released after the flow has travelled 4 m, and after 1 m for development of particle suspension, the particles may deposit themselves. The presented particle was deposited after roughly 3 m

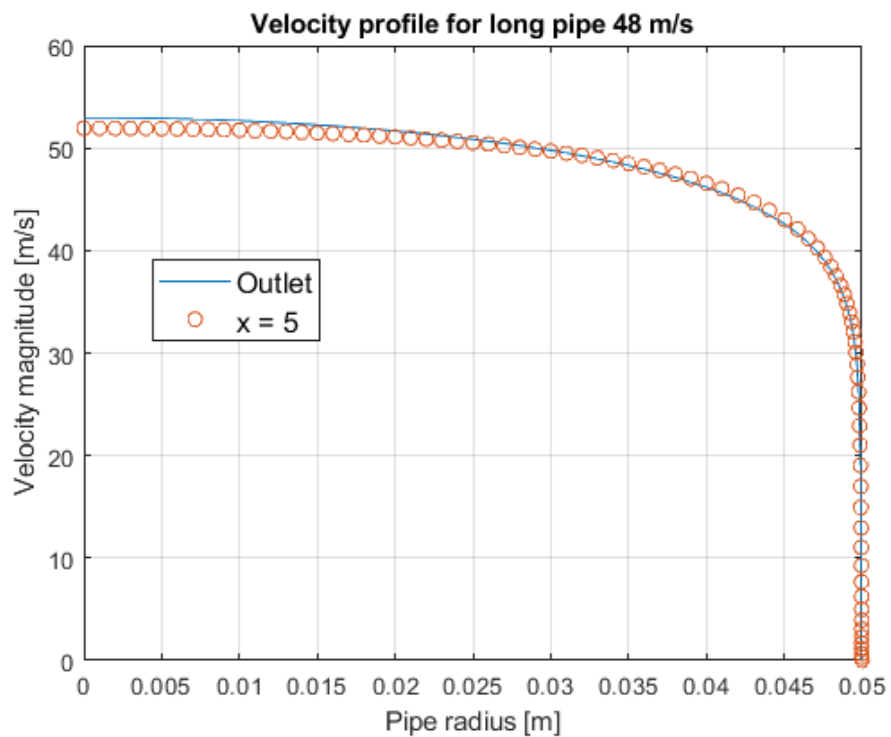


Figure 5.4: Notice how the 5 m and 10 m profiles are nearly identical.

5.3 Simulation parameters

Pipe flow simulations analyzed in this work uses the following parameters for fluid and particle data. Further simulations are performed with simulated colloidal silica particles.

DPM Aluminium-Oxide			
Properties	Values	SI Unit	Note
Density	3750	kg/m^3	Tandberg (2017)
Particle Diameter	0.5 - 100	μm	
Specific heat	775	J/kgK	Tandberg (2017)
Thermal conductivity	35	W/mK	Tandberg (2017)
Young's modulus	410	GPa	Tandberg (2017)
Poisson ratio	0.27	-	Tandberg (2017)
DPM SiO ₂			
Density	2000	kg/m^3	Plyasunov (2012)
Particle Diameter	0.001 - 25	μm	
Specific heat	44.24	J/kgK	Plyasunov (2012)
Thermal conductivity	1.4	W/mK	Plyasunov (2012)
Fluid data, air			
Density	1.16	kg/m^3	Tandberg (2017)
Temperature	373	K	Tandberg (2017)
Wall temperature	323	K	Tandberg (2017)
Specific heat capacity	1007	J/kgK	Tandberg (2017)
Thermal conductivity	0.026	W/mK	Tandberg (2017)
Viscosity	$1.589 * 10^{-5}$	m^2/s	Tandberg (2017)
Fluid data, water wapor			
Density	0.5542	kg/m^3	ANSYS ® (2019)
Temperature	700	K	
Wall temperature	650	K	
Specific heat capacity	2014	J/kgK	ANSYS ® (2019)
Thermal conductivity	0.0261	W/mK	ANSYS ® (2019)
Viscosity	$1.34e - 05$	m^2/s	ANSYS ® (2019)
Pressure loss	3	bar	
Fluid data, steam, hot case			
Density	144.25	kg/m^3	Toolbox (2018)
Temperature	773.16	K	
Wall temperature	723.16	K	
Specific heat capacity	2128.75	J/kgK	Toolbox (2018)
Thermal conductivity	0.66	W/mK	Toolbox (2018)
Viscosity	$3.5 * 10^{-5}$	kg/ms	Toolbox (2018)
Pressure at inlet	350	bar	
Pressure at outlet	342	bar	

Table 5.2

5.4 Simulation results

5.4.1 Long pipe

Simulation of silica particle deposition in a long pipe was conducted in order to study the deposition of nanoparticles. The smaller particles requires a higher Reynolds number in order for the particles to fit the relaxation rate parameters like those investigated in previous studies, and for which empirical formulae are available (Ahmadi, 1994).

In analyzing the concentration of deposited particles along the surface wall of the pipe length, the deposition behaviour of the particles can be interpreted for any particle size.

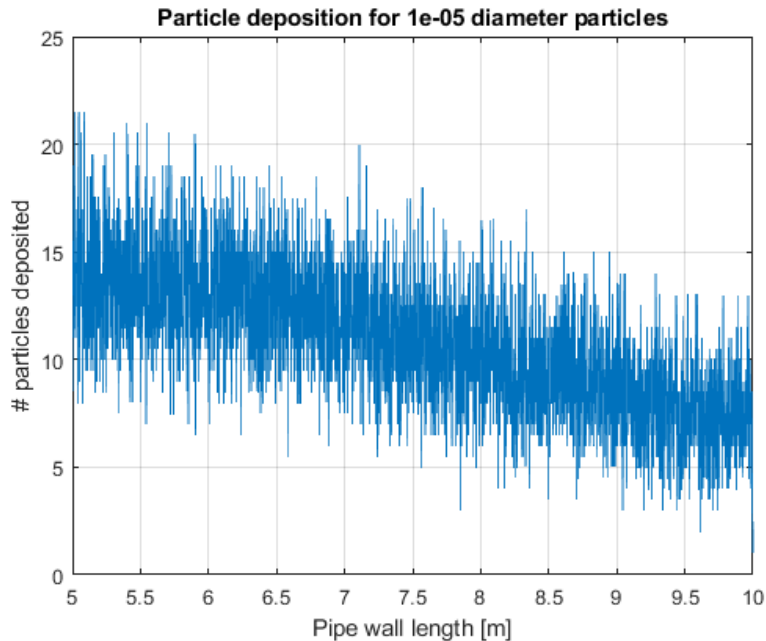


Figure 5.5: The particles detected onto the wall surface are displayed for the region in which the particles are allowed to deposit themselves

The resulting plots reveals that particles of lower relaxation rate (in the region governed by turbulent and molecular diffusion) mostly deposits later in the pipe flow than that of the higher relaxation rates. By integrating the deposited particles per pipe length increment the deposition velocity per length can be plotted. The results show that for larger particles with high deposition rates, the dimensionless deposition velocity remains nearly constant throughout the pipe flow, as the amount of deposited particles decrease in tandem with decreasing particle concentration.

At lower relaxation rates (for the current Reynolds number, particles of 80 nm corresponds to a dim. less relaxation time of 0.0191) particle deposition increases further down the pipe, which also increases the dimensionless deposition velocity due to the low concentration being deposited. The implication that there is an increase in V_{dep}^+ with increasing pipe wall position gives a strong incentive to repeat the simulation for an elongated pipe model.

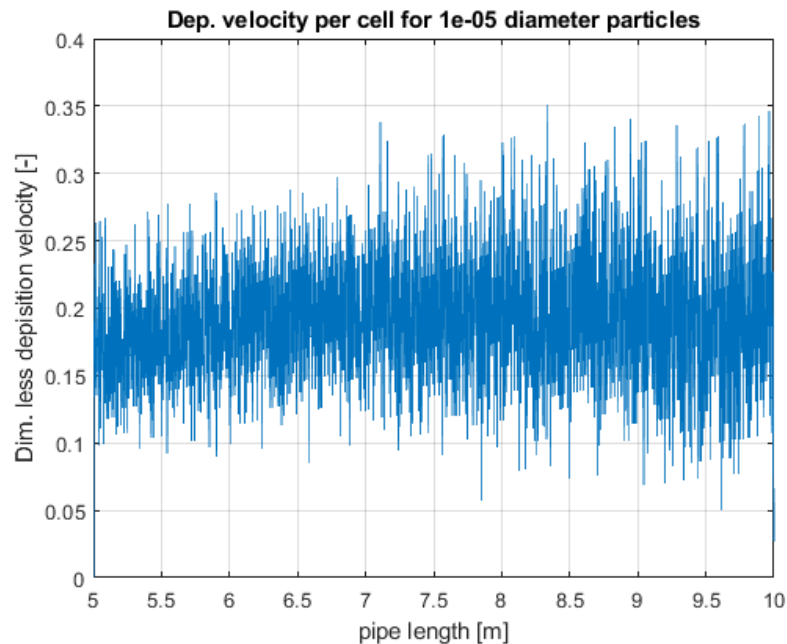


Figure 5.6: Dimensionless deposition velocity is plotted by dividing particle difference across each cell. Integrating this plot yields the average deposition velocity visible in the deposition chart shown in figure 5.8

Figure 5.8 shows that for lower relaxation rates (which implies smaller particle diameters), the deposition velocity is higher than what empirical formula suggests. The region in which this increase in V_{dep}^+ applies both in the molecular diffusion region and the lower half of the inertia-driven region. The over-estimation of deposition velocity begins for sub-micron sized particles for the set Reynolds number.

The Schmidt number is also plotted for the varied particle diameters.

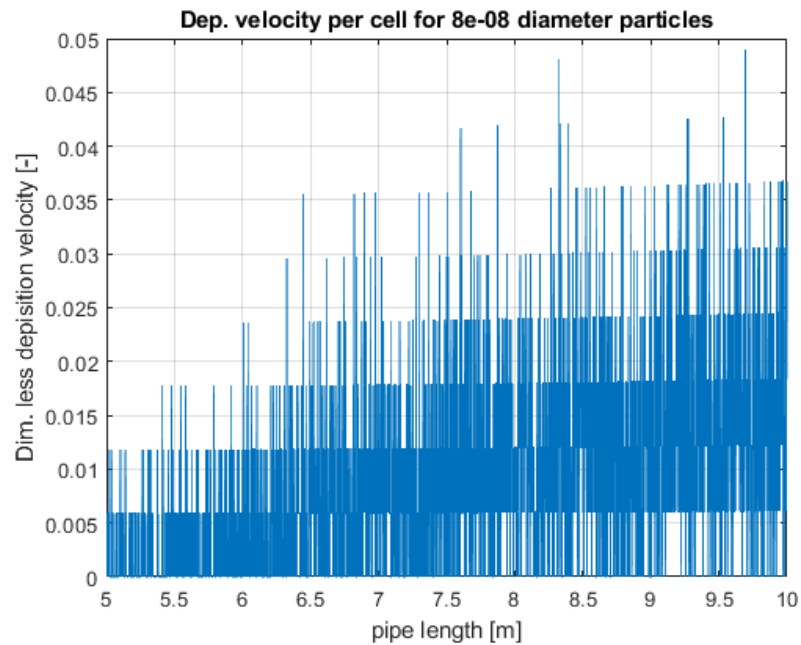


Figure 5.7: Number of deposited particles increases further down the pipe for smaller particles.

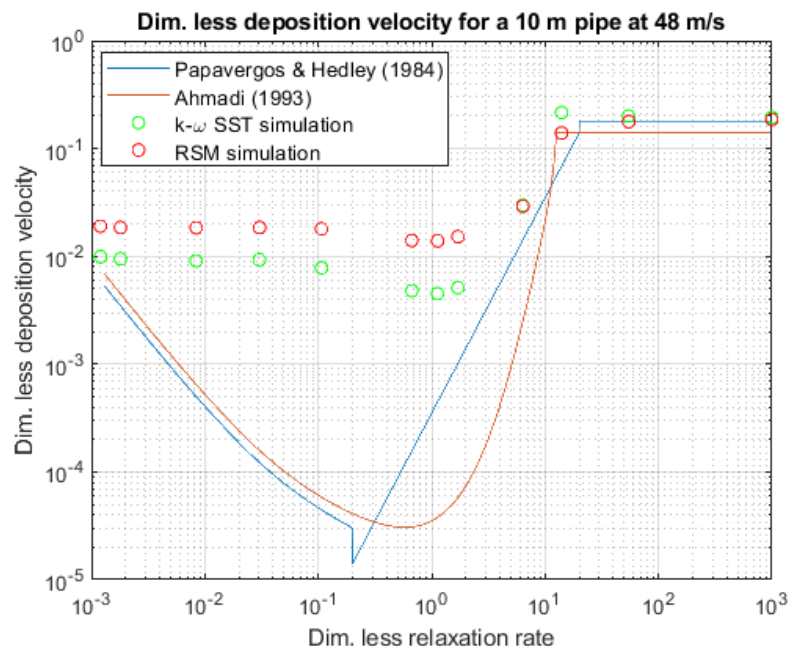


Figure 5.8: Dim. less deposition velocity compared to the empirical formula of Papavergos and Hedley (1984) and Ahmadi (1994).

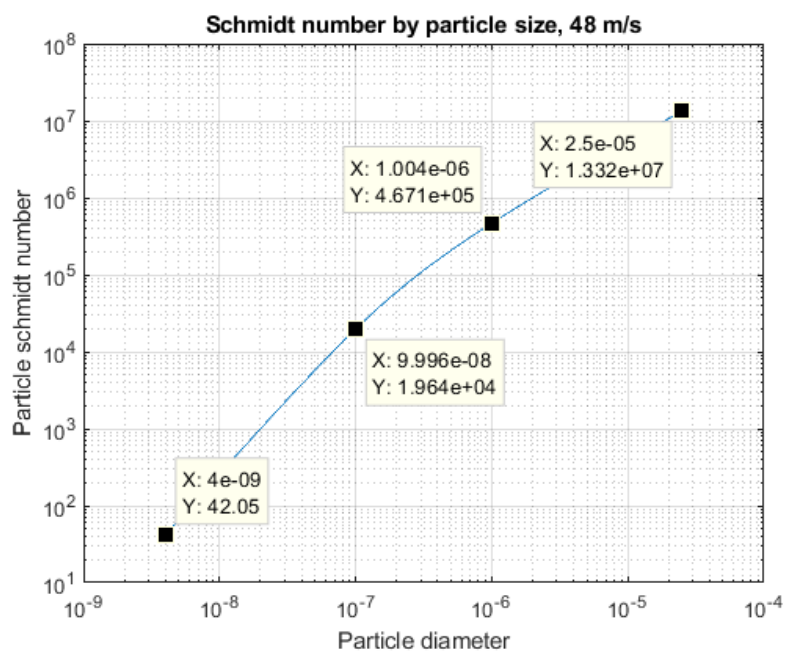


Figure 5.9: For simulation of air flow with the conditions utilized by Tandberg (2017), the value is observed to vary drastically between particles of nanometres and micrometres. The smallest particles have Schmidt numbers in the exponent of 10^2

Low velocity pipe

In order to investigate the effects of higher Reynolds number on particle deposition, the same 10 m pipe was simulated with an inlet velocity of only 10 m s^{-1} , resulting in a mean velocity across deposition section of 9.8 m s^{-1} . This lowers the pipe Reynolds number from 302518 to 61683, and will also shift the particle relaxation time parameter upwards, such that sub-micron particles are only associated with a dimensionless relaxation time $\tau_p^+ < 10^{-2}$.

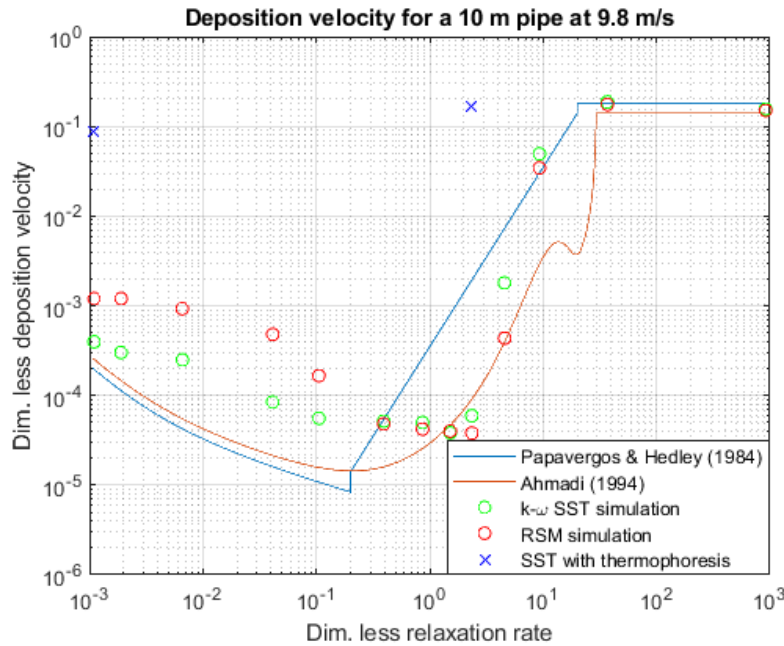


Figure 5.10: Dimensionless particle deposition correlates better with empirical formula of Ahmadi (1994), the Reynolds number now only 61×10^3 .

The resulting dimensionless deposition velocity correlates very well with the empirical data of Ahmadi (1994).

Thermophoresis

The effects of turbophoresis are observed to not be very noticeable for higher Reynolds numbers, such that the effects of thermophoresis won't be very visible for the high velocity flow simulations. Adding thermophoretic forces onto particles in the low-velocity simulation allows for analyzing the effects on smaller particles more accurately, as the deposition velocity differences between particle sizes are much greater for the low Reynolds numbers than for the higher ones.

As expected, the deposition velocity of diffusion-driven particles increase by several exponents. The resulting deposition velocity is at most three exponents higher than that of the same simulation without thermophoresis. It is observed that most of the particles are deposited immediately after the capture boundary condition is activated. This implies that particles have diffused towards the wall in large scale, which is also suspected for other particles of similar size. The absence of similar deposition numbers at this position for the same

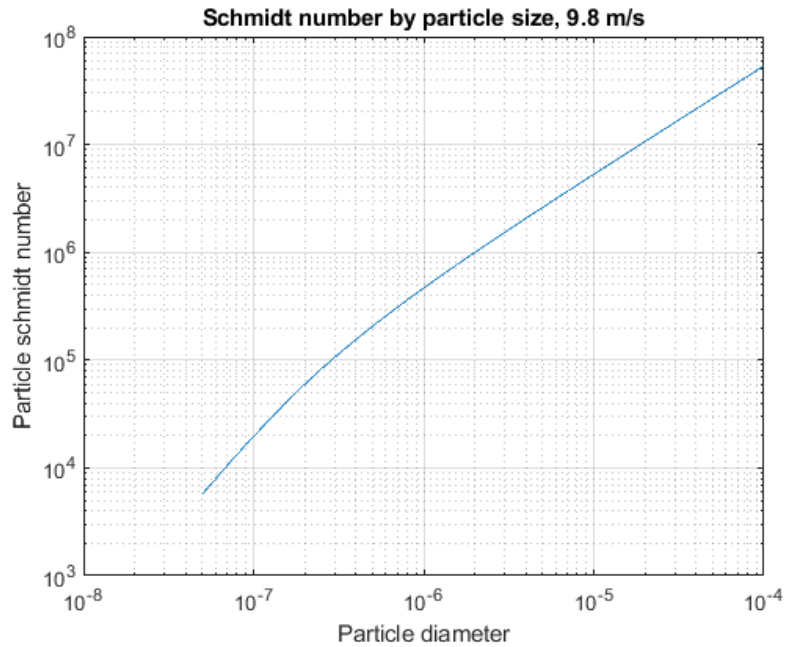


Figure 5.11: It is observed that even for low relaxation times, i.e. small particle diameters, the Schmidt number is still above 10^3 .

simulation without thermophoresis suggests that the thermal gradient yields a strong enough thermophoretic force to diffuse the near-wall particles onto the surface wall.

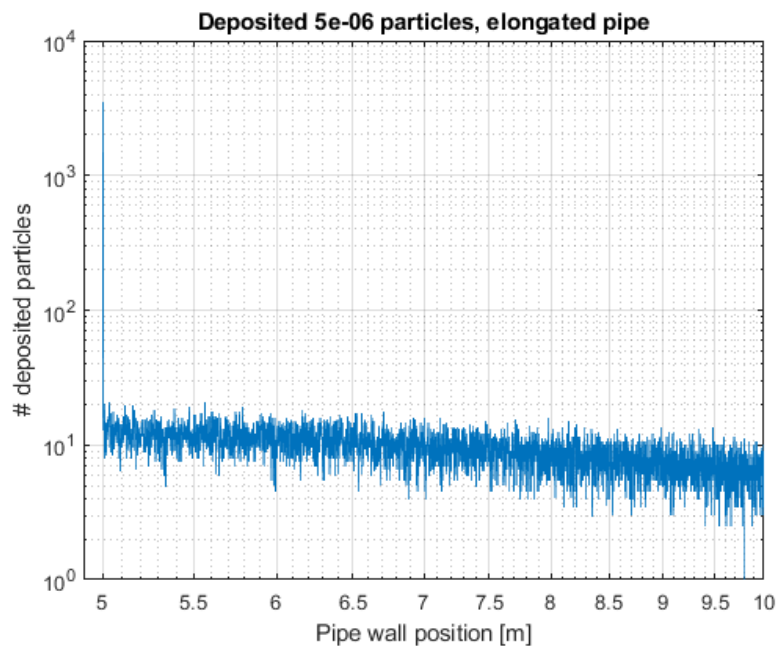


Figure 5.12: Particles between the relaxation time region 1 and 2 deposits nearly uniformly the moment the surface is given the trap boundary condition at pipe length $L = 5m$.

5.4.2 Elongated pipe

Due to the results of the long pipe simulations implying a concentration increase of sub-micron particles in proximity to the pipe wall further down the pipe length, an elongated pipe flow was simulated in order to study the durability of this deposition rate increase and how it handles further deposition.

The deposition rate of the elongated length was first investigated for the length of the original simulation. Figure 5.13 shows that the results between both simulation are reasonably similar. This lends credit to the elongated mesh having the same deposition behaviour as the long pipe simulation.

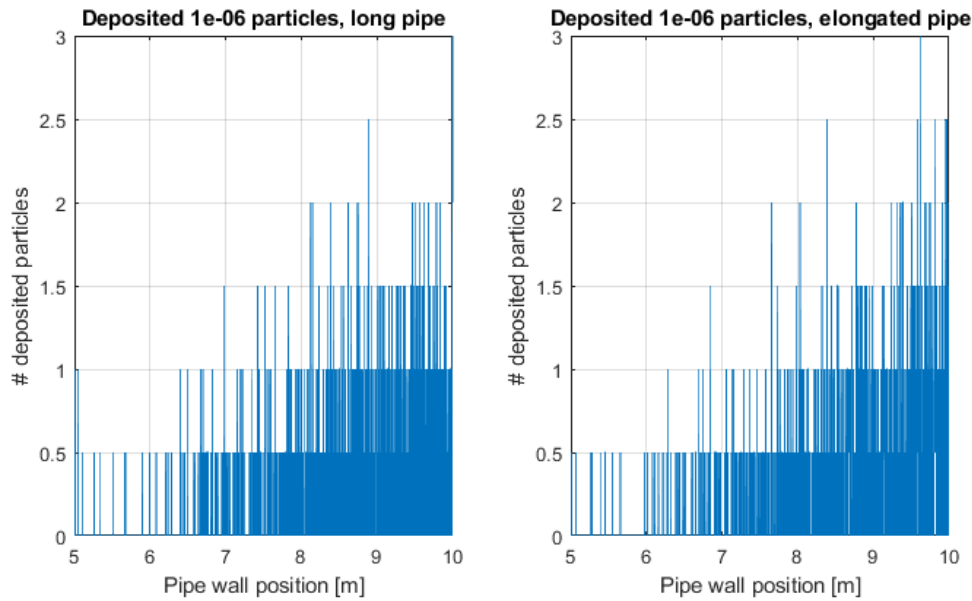


Figure 5.13: Particle deposition in the 15 m long pipe with doubled deposition increment seems to match the behaviour of the 10 m pipe fairly well.

The results of elongating the pipe shows a similar deposition velocity for smaller particles, and when comparing the amount of deposited particles along the pipe to the remaining amount of particles in the flow, a semi-linear increase of deposition rates can be found for particles below $0.1 \mu\text{m}$.

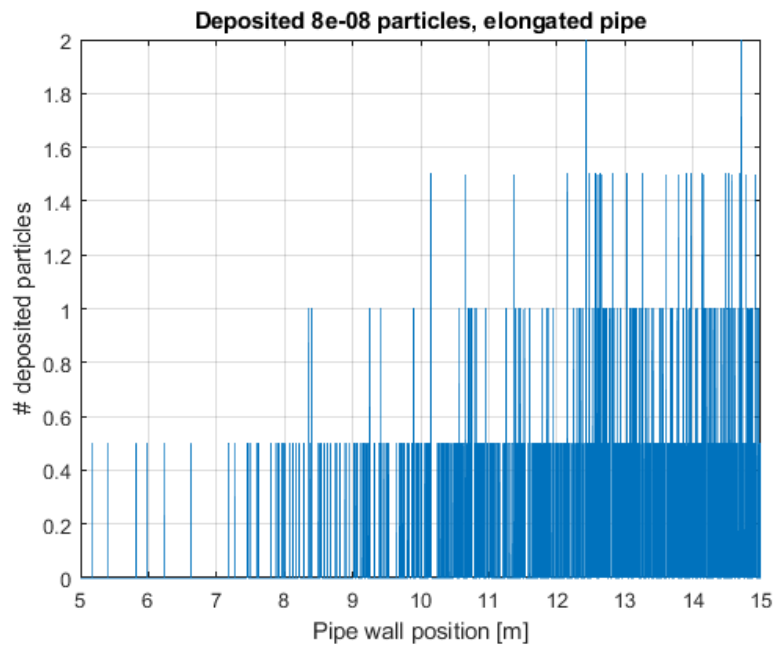


Figure 5.14: Sub-micron particles deposit themselves with increasing frequency until the rate evens out after ~ 12 m.

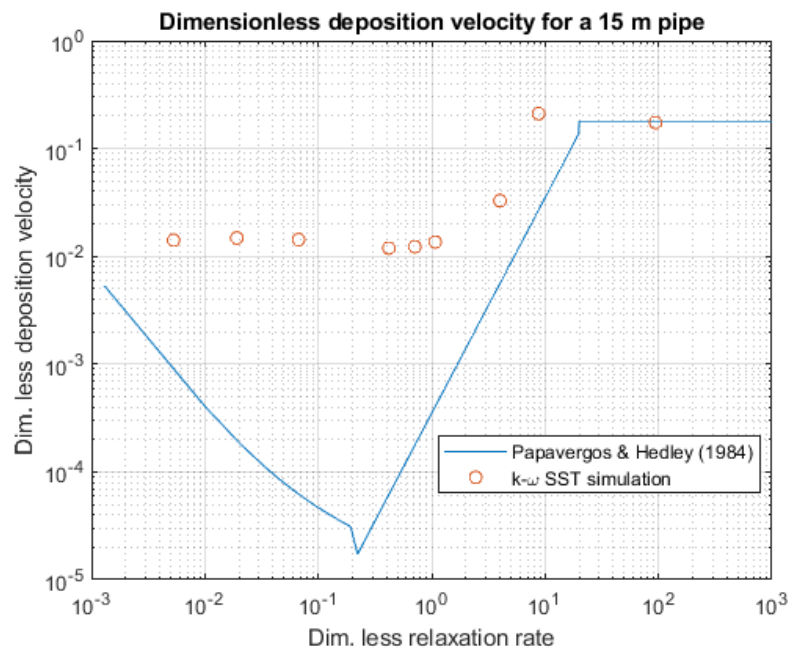


Figure 5.15: The deposition velocity for smaller particles with lower relaxation rates does not correlate with Papavergos and Hedley (1984).

5.4.3 Gravitational flow

Another simulation was performed for particle deposition, this time for heated water vapor with standard fluid properties provided by FLUENT. In this simulation, gravity was also introduced in order to investigate its effect on larger particles in turbulent flow.

It should be noted that by altering the fluid mass flow and average velocity to fit that of water vapor, the size distribution of particles was altered in order to fit the particle relaxation from water vapor conditions.

The pipe was simulated for a pressure drop of 3 from inlet to outlet, resulting in a mean flow velocity of $\sim 24.4m/s$, which translates to a Reynolds number of 100930.

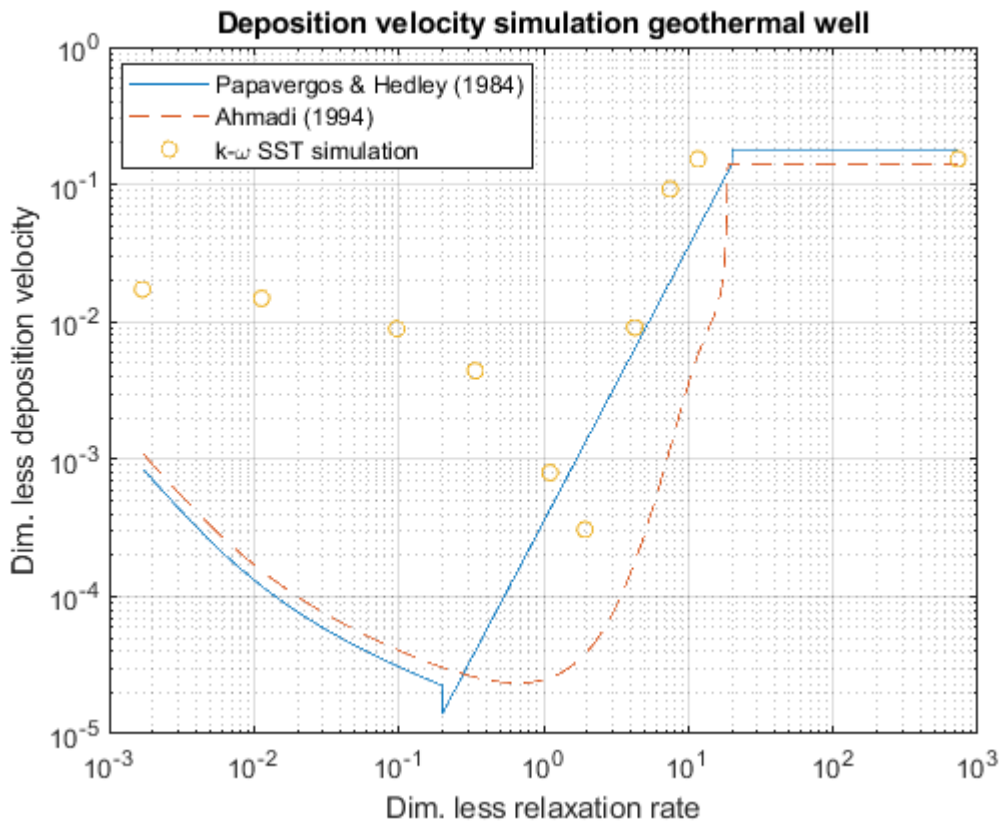


Figure 5.16: The deposition velocity for upward pipe flow is similar to the other results of high turbulence flow simulations. The 2nd region appears to have shifted towards higher relaxation times.

It is observed that the deposition velocity for smaller particles yielded by the simulation is noticeably higher than that of empirical formulae. Compared to the results of higher Reynolds number flow, the deposition rate behaves similar in the 1st region (governed by diffusion). In the second region the deposition velocity decreases more rapidly than from previous simulations of high Reynolds numbers. The decrease and subsequent increase in deposition velocity, recognized as the inertial impact region, appears to have shifted to the right, beginning for higher relaxation times than for previous simulations.

5.4.4 Geothermal pipe flow

Final simulations of particle deposition were made for the conditions predicted in the geothermal well according Fridriksson et al. (2015). The properties were retrieved from Toolbox (2018) using the pressure and temperature ranges from Fridriksson et al. (2015) and Bordvik (2020). Gravity is also introduced, making the pipe flow an upward flow.

It should be noted that by altering the fluid mass flow and average velocity to fit that of a realistic geothermal well, the parameters set for previous simulations in order to compare results with that of Tandberg (2017) will no longer be followed, as the priority is to study deposition behaviour of particles of a set size parameter.

Simulations were conducted with an inlet pressure of 350 bar. Due to convergence issues, the pressure at outlet was set to 342 bar, which yields a low fluid velocity and a high fluid pressure. The high pressure of the fluid was accounted for in determining the mean free path in this instance, and so equation 2.21 was utilized instead of equation 2.20. Mainly due to the high density of pressurised steam, the particle relaxation times for sub-micron particles becomes several exponents lower than for previous simulations. A silica particle of 4 nm is computed to have a relaxation time of $\tau_p^+ = 5.4352e - 09$. Only when particles reach 3 μm in size are they within the scope of previously measured deposition velocities.

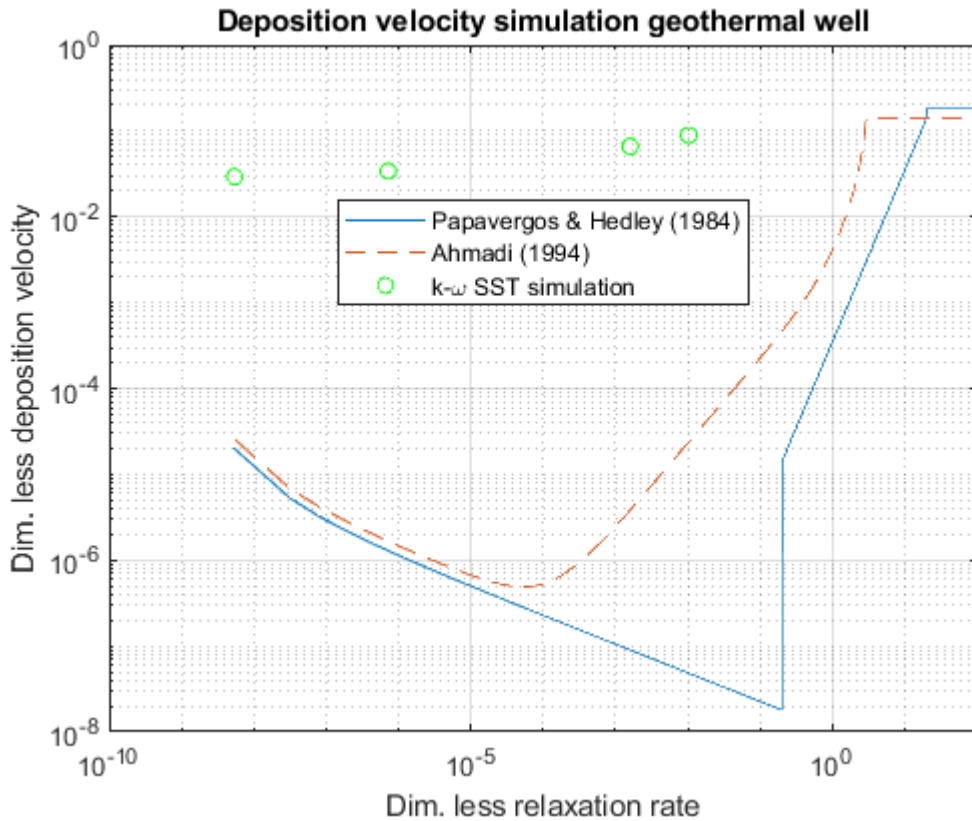


Figure 5.17: Despite terribly low particle relaxation times, the deposition velocities of particles are rather high.

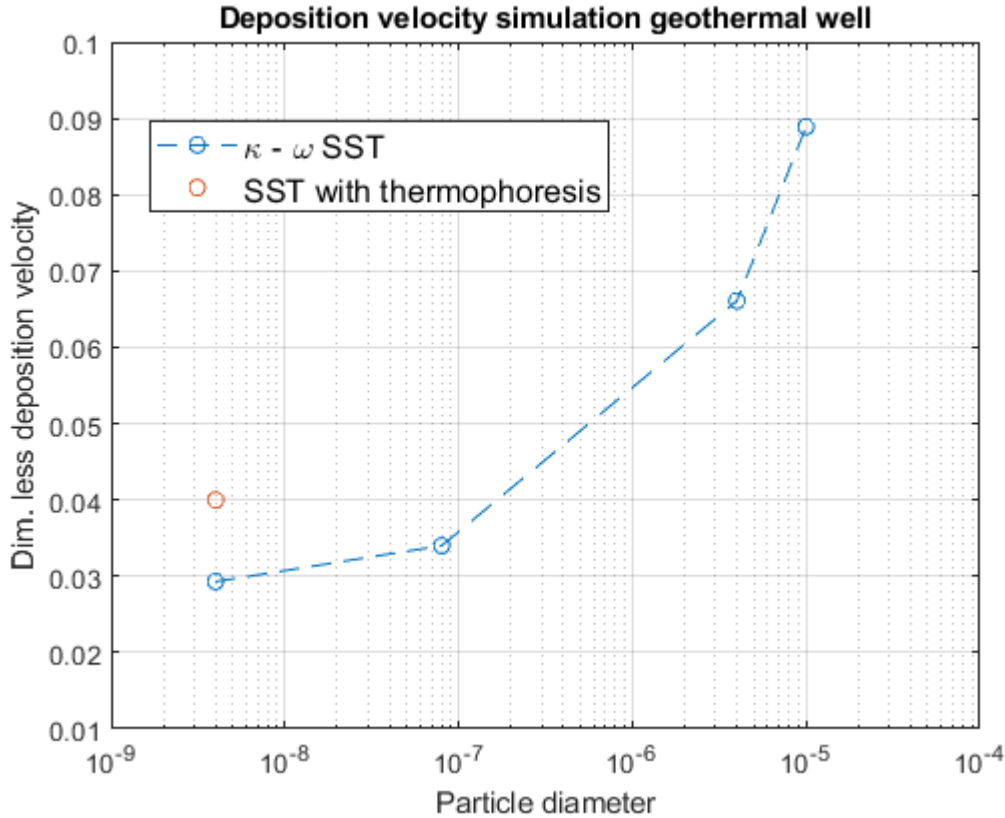


Figure 5.18: Deposition velocity for smaller particles are shown to increase slightly with thermophoresis.

The lowest measured particle size is 4 nm, and the results show a deposition velocity of ~ 0.03 . Compared to the previous simulations does this high deposition velocity normally belong to particles larger than 1 μm .

It is observed that the deposition velocity for smaller particles yielded by the simulation is noticeably higher than that of empirical formulae. Compared to the results of higher Reynolds number flow, the deposition rate behaves similar in the 1st region (governed by diffusion). In the second region the deposition velocity decreases more rapidly than from previous simulations of high Reynolds numbers. The decrease and subsequent increase in deposition velocity, recognized as the inertial impact region, appears to have shifted to the right, beginning for higher relaxation times than for previous simulations.

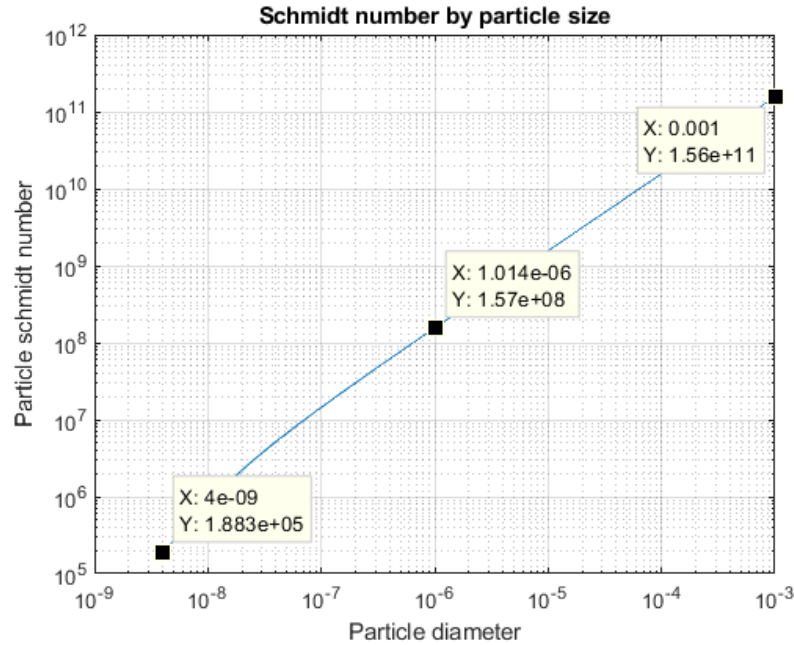


Figure 5.19: Even particles of 4 nm diameter have a Schmidt number above 10^5 for geothermal conditions.

5.4.5 Bend

A relevant scenario to be investigated for silica deposition is a pipe bend, common in most plants. Due to the nonparallel geometry of this scenario, the potential for concentrated particle deposition may be high, as observed during Karlsdottir et al. (2014).

The results show that a majority of depositions appear in the bend of the geothermal pipe. The contour plot figure 5.21 shows that all particles that deposit in the bend tends to exit the mean flow and turn around in the outer part of the bend. The particles then register as trapped onto the wall surface.

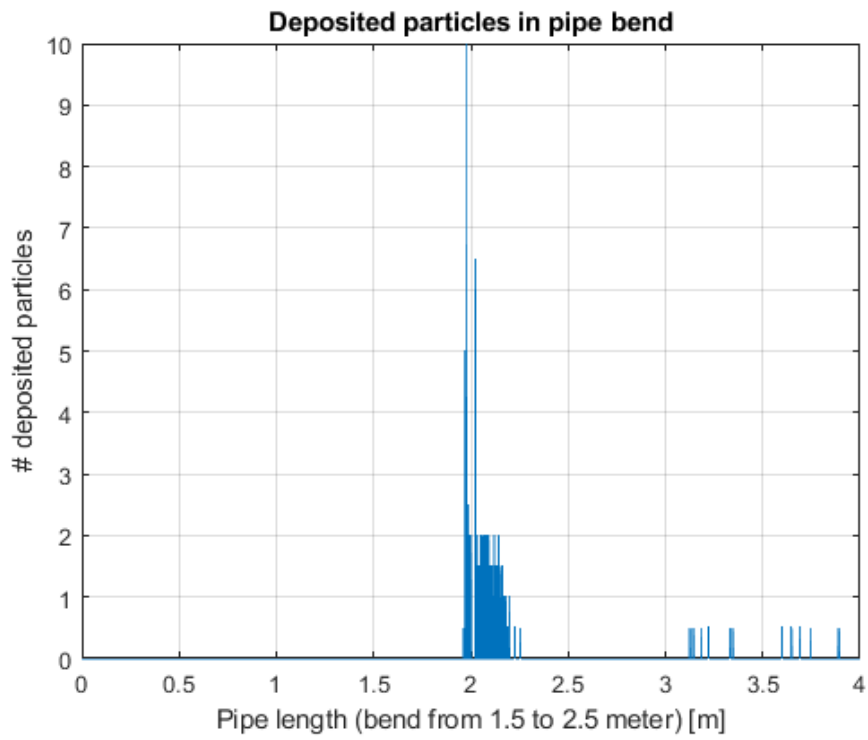


Figure 5.20: Deposited particles in the pipe bend



Figure 5.21: Particle tracking shows deposition of 1 μm diameter silica particles, as it separates from the free stream and reverses onto the outer wall.

6. Discussion & comparison of results.

6.1 Comparison to empirical formulae

While the deposition rates of Tandberg (2017) are slightly higher than theory implies, such increased rates are pointed out in chapter 3.4.3

Even higher rates are however recorded in the present simulations with increased Reynolds number. The higher deposition rates are noticed as particle sizes becomes sub-micron in scale, or rather, as the dimensionless particle relaxation rate drops below 1.

As the most recent empirical formula, Ahmadi (1994) have taken into account more effects than that of Papavergos and Hedley (1984), and is therefore in better correlation with experimental data for low Reynolds numbers.

6.1.1 Turbulence modeling

The difference in deposition velocity between simulations for the two elected turbulence models must be discussed. As expressed in 3, the two-equation turbulence model like the $\kappa-\omega$ model assumes the turbulence to be isotropic, which can lead to higher normal fluctuation. Both models are described in ANSYS [®] (2019).

The results are show a higher correlation between the SST-model results to empirical formula than that of the RSM-model results, particularly in the diffusion governed region of the relaxation time parameter. As the turbulent diffusion of particles is key to the deposition velocities of smaller particles, a divergence in results were to be expected to take place here, if there was to be a divergence.

The results of the low-velocity simulation of the 10 m pipe in particular shows that the present standard RSM turbulence model leads to a more rapid increase of deposition velocity as particles become smaller. While the SST turbulence model yields an deposition velocity within the same exponent of the empirical models and experimental data of Wells and Chamberlain (1967), the RSM model yields results of one exponent larger than these. When compared to experimental data of lower Reynolds numbers yet turbulent flow from Shimada and Okuyama (1993), both models yield results within the deposition velocity range.

Tian and Ahmadi (2006) explains that the RSM turbulence fluctuation normal to the wall follows a quadratic variation, which is not accounted for in the standard RSM model. This implies that the vertical fluctuation velocity will vary with square of the distance from wall within four wall distance units. Due to the linear nature of the interpolation scheme, the use of this scheme within even within very short distances of the wall can yield high values of vertical velocity fluctuations, which leads to higher deposition rates for low relaxation time particles. A correction for this quadratic variation is therefore presented, which should fix the turbulence fluctuation error close to the wall in RSM model simulations:

$$\begin{aligned} \sqrt{v'^2} &\propto y^2 \quad \text{as } y \rightarrow 0. \\ v^{+'} &= Ay^{+2} \quad \text{for } y^+ < 4, \end{aligned} \quad (6.1)$$

where the fluctuation $v^{+'} = \sqrt{v'^2}/u_*$.

The resulting change in deposition rate is very noticeable in figure 6.1. Introducing this equation to the ANSYS program would most likely improve the particle deposition rate for the higher turbulence simulations of the RSM-model in ANSYS.

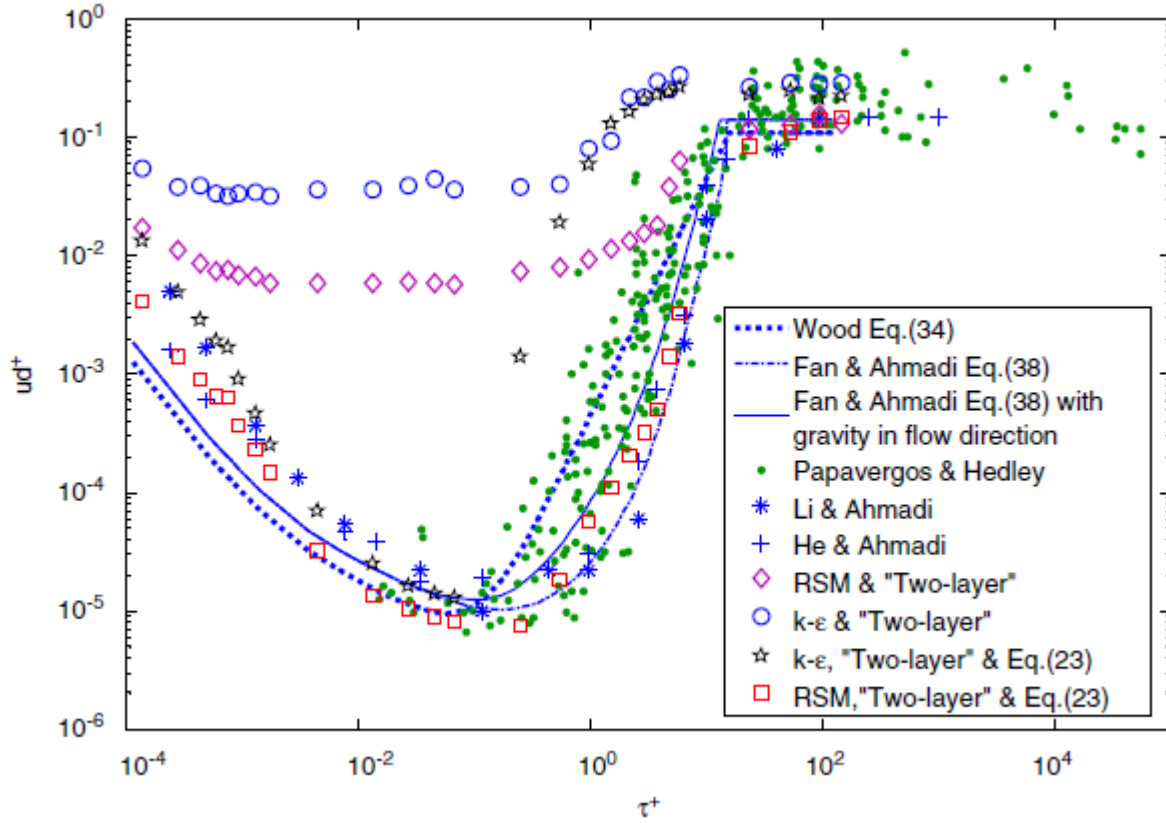


Figure 6.1: The introduction of equation 6.1 can be seen to clearly correct the RSM model prediction of 1st and 2nd region particle deposition velocity, leading to good correlation with empirical formula and experimental data. Plot from Tian and Ahmadi (2006).

6.1.2 Particle tracking

The integral time scale utilized for controlling the time spent in turbulent motion is determined by equation 3.13, where the constant C_L is suggested by ANSYS [®] (2019). The increase of the constant from 0.15 to 0.3 when switching from two-equation models like $\kappa - \omega$ SST to the RSM model is however not justified, and the results yielded with this doubling of C_L are further away from correlation with both the SST model results and that of empirical formulae.

The treatment of particulate deposition in FLUENT also comes into question when evaluating FLUENTs treatment of particles. As was noted in figure 5.16, the inertial impaction region of the deposition velocity seems to have shifted towards larger relaxation times, i.e. larger particles. This shift may be attributed to gravitational acceleration, as argued for by Tandberg (2017). Tandberg (2017) explains that FLUENT treats a particle as a point with mass, and so it will only hit the wall when the center of mass hits the wall, i.e. the distance to wall becomes lower than r_p . In the distance close to r_p the particle is suspended in a low velocity region due to the no slip condition. Here the lift forces may be overrated, and an upward flow will increase the lift force on the particle away from the wall, leading to artificially lower deposition rates.

6.1.3 Reynolds number

It is noteworthy that most empirical data for particle deposition in pipe flow has been investigated for much lower Reynolds numbers than what will be present in geothermal steam pipes, and lower than what is simulated for the current study.

This higher Reynolds number indicates a greater turbulence than that of other pipe flows. In view of the low relaxation time of the colloidal silica particles, which makes the particles follow the fluid stream for greater momentum, a greater turbulence should lead to greater dispersion and flux of particles onto the viscous sublayer close to the wall. For particles with too low relaxation times such that inertia impacted by turbulence only deposit them into the viscous sublayer, this increased turbulence will increase the concentration of particles in said sublayer. Such an increase in particle concentration along the pipe wall may explain the results of increased amount of deposited particles along the pipe, as is displayed by the elongated pipe flow simulation 5.7.

Referring back to the empirical formula of Papavergos and Hedley (1984), there is no accounting for the increased dispersion of particles in free stream with increasing turbulence, which can be viewed as a weakness of the formula. The same can be said for that of Ahmadi (1994).

6.1.4 Nanoparticle deposition development

The smallest particle size which is accounted for in the high Reynolds number simulations of 10 and 15m pipes were at 4 nm, which translates to a dimensionless relaxation time of 10^{-3} . Both empirical models of Papavergos and Hedley (1984) and Ahmadi (1994) display an increase of deposition velocity of about 10^2 from $\tau_p^+ = 0.1$ to the low relaxation time of nanoparticles. This rather sharp increase in deposition velocity is, according to diffusion theory (Esptein, 1983), attributed to the increase in the Schmidt number. The increase is proportional to the Cunningham correction slip factor, which reaches a value of ~ 50 for the smallest particles measured.

Alternative definitions of the Knudsen number as only the ratio of the mean free path and particle radius instead of diameter is utilized by Tandberg (2017) and Tian and Ahmadi (2006), but it seems this condition comes with altered constants for the Cunningham slip

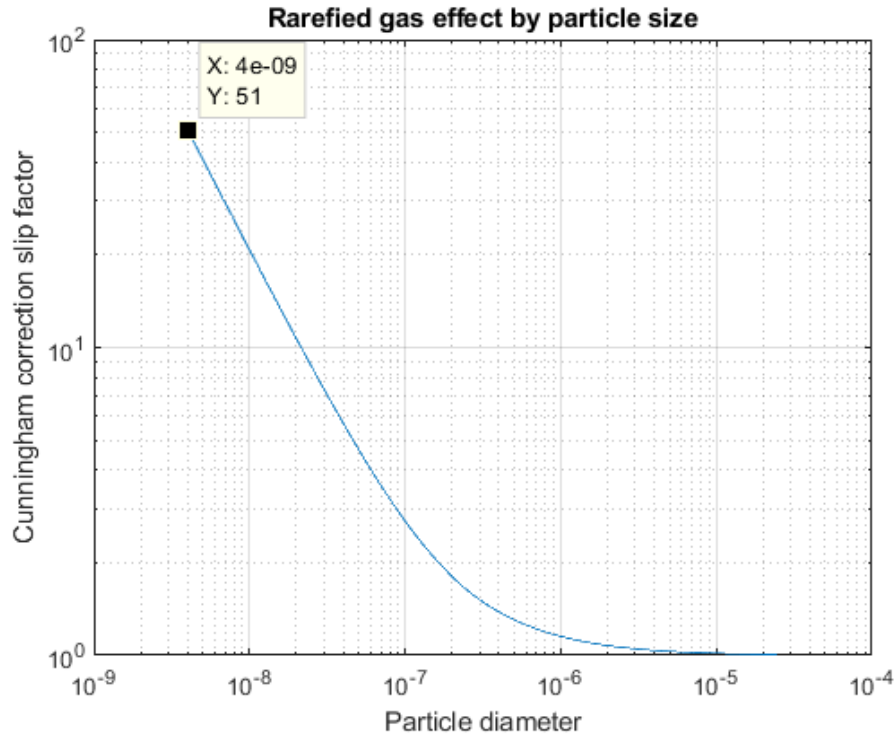


Figure 6.2: Once the particle diameter decreases below $1\ \mu\text{m}$, the Cunningham slip correction factor increases exponentially until it reaches 51 for the smallest tracked particle.

correction factor, which results in only a slight increase in the slip factor when adapted.

The adapted C_c of Tandberg (2017) utilized the mean free path equation 2.19, as only air was utilized in these simulations.

While this is a decent justification for choice of mean free path equation, it should be noted that Crowe (2006) presents a table for Cunningham slip correction factor for standard air condition for particle ranging from $1\ \text{nm}$ to $100\ \mu\text{m}$. The suggested increase from C_c at $D_p = 1\ \mu\text{m}$ is 15 %. The suggested mean free equation utilised by Tandberg (2017) results in $C_c = 1.14$ however.

6.2 Comparison to experimental results of geothermal wells

Figure 5.18 shows that the current model for deposition yields vastly different particle deposition velocities for higher pressure steam flows than that of deposition results for particles suspended in air. The model comes into question due to a relatively low pressure drop between pipe inlet and outlet. Regardless, the drastic change in particle relaxation time and diffusion-driven deposition velocity is noticeable. As the current simulation only achieved a Reynolds number of $2 * 10^4$, higher turbulent diffusion may be present in geothermal flow than detected here. The diffusion of sub-micron particles is however partly hindered by the

high pressure found in the geothermal flow. As figure 6.3 shows, the rarefied gas effect becomes almost negligible for particles larger than $0.1\ \mu\text{m}$. As the Schmidt number increases, dependency upon viscous dissipation increases for geothermal flows, and figure 5.19 show a clear increase in Schmidt numbers for geothermal conditions.

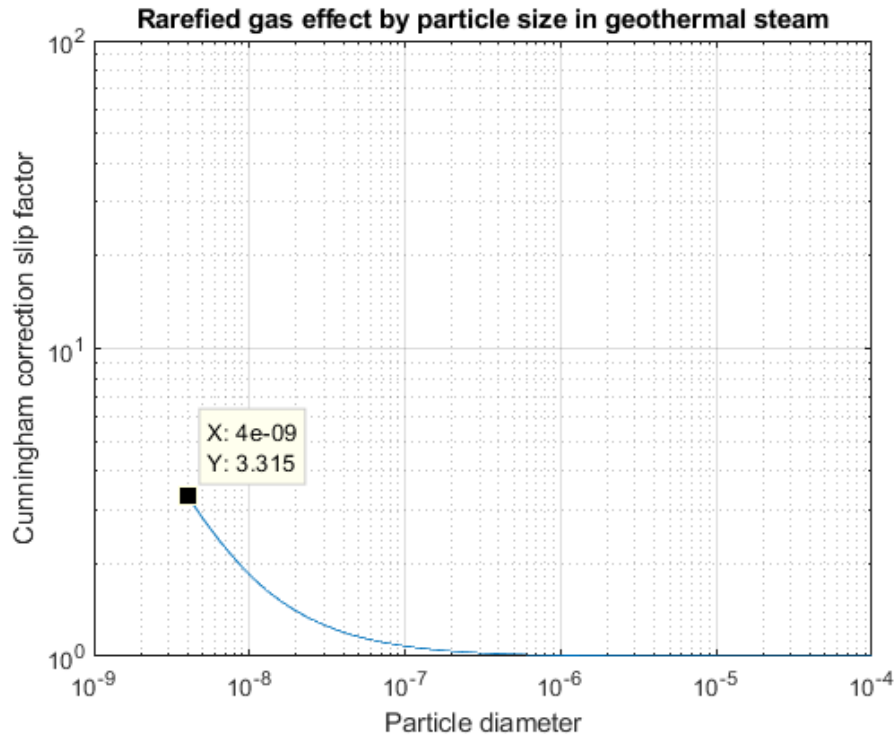


Figure 6.3: The plot is from the simulation of superheated gas at 350 bar pressure. The Cunningham slip correction factor is dependent on the mean free path, which is lowered drastically for high pressure.

Karlsdottir et al. (2014) presents an experiment in silica deposition based on measurements from the IDDP-1 project. In these experiments, inner pipe diameters of about 26 mm and fluid velocities of about $100\ \text{m s}^{-1}$ were primarily used to simulate geothermal flow. Such high velocities will only further decrease the particle relaxation time of particles.

6.3 Thermophoresis

While particles of lower relaxation times are initially shifted towards the wall due to turbulent diffusion, once the particles are small enough for the impact of turbulence to lose its effect, there is little chance for the sub-micron particles to penetrate the viscous sublayer by aid of brownian diffusion. Once the force of thermophoresis is taken into account, such sub-micron particles will much easier be driven into the surface wall. As Fridriksson et al. (2015) and Karlsdottir et al. (2014) points out, geothermal pipes can have severe temperature gradients, nearly raising the deposition velocity to the maximum of inertial particle effects.

6.3.1 Deceleration of pipe bends

The section of deceleration which can be found in sharp bends is a well known phenomenon in fluid dynamics (Karlsdottir et al., 2014), along with erosion from particles colliding with the pipe wall (as can be seen in figure 6.4). The dependency of flow depth and Reynolds number on the shear tension and separation point for the fluid flow in such bends makes deceleration a relevant issue for high velocity steam flows, as bends can usually be found in geothermal plants.



Figure 6.4: Erosion caused in the exit region of an outer bend retrieved from the geothermal flow experiment performed by Karlsdottir et al. (2014).

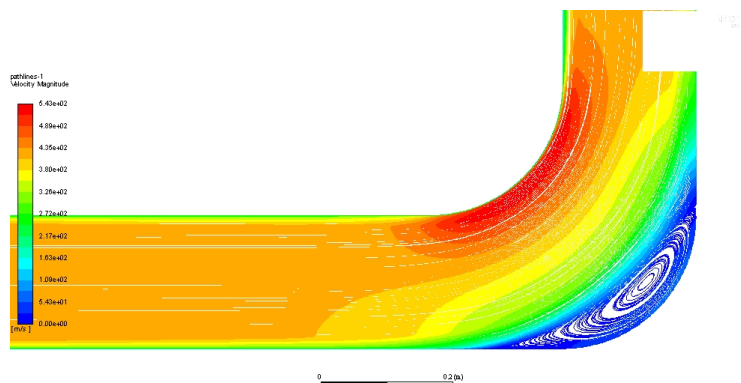


Figure 6.5: Outer wall deceleration with flow separation observed for high velocity flow in a sharp bend.

6.4 Aging and scaling

It is suggested by Daniela B. van den Heuvel (2018) that silica film from deposition will continue to agglomerate with continuous well operation, the aging being similar to that used by Kokhanenko (2014) and Chauhan (2019) in order to produce certain sizes of colloidal silica for their experiments. This continuous agglomeration of the film has previously been

discussed as a vital factor for further particle deposition, but may also yield opportunities for re-suspension, as larger particles experiences larger lift forces and greater impaction from collision of incident particles normal to deposited layer. The restitution and re-suspension of particles is beyond the scope of this study, but such effects should be investigated as possible solutions to silica fouling.

7. Conclusion & further work

7.1 Conclusion

In this study, formation and deposition of colloidal silica was discussed, and computational models for particle deposition with the conditions of colloidal silica were formed and evaluated.

Colloidal silica formation in deep geothermal wells is dependent mainly on the fluid temperature, pressure and pH-levels. For a geothermal fluid composition as predicted in Fridriksson et al. (2015), Plyasunov (2012) argues for a size distribution of ~ 4 nm. It is recommended to form a more realistic size distribution model of particles. This should be based on the findings in Kemia and Landsvirkjun (2019).

From the theory on deposition of particles it is revealed that certain mechanisms like particle surface charge, particle re-entrainment and condensation onto particles will affect the sticking probability of colloidal silica, but these mechanisms have not been accounted for in previous studies. The mechanisms with highest impact on particulate deposition is turbophoresis, thermophoresis and brownian diffusion.

Two previous papers of particle deposition simulation were presented, that of Chauhan (2019) and Tandberg (2017). The papers utilized different CFD tools in order to simulate fluid flow and deposition. Evaluations of the results and methods of each paper lead to the conclusion that the Tandberg (2017) thesis presents a more detailed and user-friendly method of simulation. This lead to ANSYS FLUENT being elected as CFD tool for this study.

On the recommendations of ANSYS (2014) and Tandberg (2017), the turbulence models $\kappa-\omega$ SST and RSM were elected for simulation of fluid flow. The turbulence models were compared for their behaviour close the the surface wall, and no major differences were observed, which hinders the choice of one model over the other. Particle deposition was therefore analyzed for simulations with both models.

The first simulations were performed with fluid properties and velocity parameters similar to those used in Tandberg (2017). The deposition velocity results show a clear correlation between $\kappa-\omega$ SST and RSM turbulence models. However, the results deviate from empirical formulae in the diffusion-driven region. The suspected reason for the inaccuracy is different for each turbulence model. For the RSM model it is suspected that the velocity fluctuations close to the wall becomes overrated due to quadratic variation of turbulence. The SST model is suspected of being unable to predict dissipation of turbulent energy onto the surface wall with sufficient accuracy.

The following simulations were performed for similar fluid properties, but with higher inlet velocities so as to evaluate the robustness of the turbulence models for higher Reynolds numbers and smaller particles. Particles with properties like that of colloidal silica were also introduced in the DPM in order to simulate deposition of nanoparticles similar to those

discovered on Iceland Kemia and Landsvirkjun (2019). The results show higher spread of between each turbulence model and empirical formulae in the diffusion-driven region. The RSM model shows higher deposition velocities than the SST model. The measured deposition rates for the smaller particles showed an increase along the pipe length.

A lower velocity simulation with identical properties was performed so as to investigate the effect of Reynolds numbers on smaller, diffusion driven particles. The results show higher agreement with empirical formulae, which shows the lack of robustness from the turbulence models when compared to the higher Reynolds number simulations. Thermophoresis was also shown to have a large impact on diffusion-driven particle deposition.

Another high velocity simulation was made with identical parameters for an elongated pipe in order to investigate the increase in deposition rate from the previous simulations. The deposition rates are shown to straighten after ~ 12 m. The resulting deposition velocity has a slightly lower value to that of the shorter pipe simulation, which is the result of the increase in deposition rates for smaller particles.

Upward flow simulations show that the deposition velocity profile in the inertial-driven region are lower than empirical formulae at the 2nd region. This is suspected to be due to the gravitational acceleration affecting lift forces on larger particles. FLUENTs treatment of particle deposition criteria is suspected to further decrease deposition rates for medium-sized particles, as particles are lifted away from the wall that should otherwise have been registered as deposited.

A simulation of a sharp pipe bend shows a high concentration of depositions happening in the very middle of the pipe bend. When tracking single particles, the particle is shown to reverse the free stream before exiting the bend before depositing onto the outer bend wall. The particle is suspected of being influenced by the decelerated zone which appears out the outer bend, as shown in figure 5.21.

The final simulation under geothermal conditions shows a high deposition velocity for all sub-micron particles. The increased pressure lowers the particle relaxation time drastically and lowers the dependency of brownian diffusion for particle deposition.

The DPM method of particle tracking appears to show weakness for gravitational acceleration. The method is suspected of underrating particle deposition for medium-sized particles in upward flows due to its criteria for particle deposition.

The results show a continuous inaccuracy of deposition velocity predictions for smaller particles in turbulent flows. It is concluded that the $\kappa - \omega$ SST model is inadequate for predicting diffusion-driven deposition of particles in proximity to the wall.

7.2 Further work

This model for predicting silica deposition uses several assumptions which should be thoroughly investigated in order to simulate for a most realistic scenario. And while the method of deposition modeling in this study takes into account some key features of deposition me-

chanics, there are several factors that can be added to improve the model. Three points of interest should therefore be addressed in further studies:

- Investigation into colloidal silica formation in geothermal steam
- Improvements upon deposition models at wall surfaces
- Improvements / extensions of fouling mechanisms onto wall surfaces

The precipitation and deposition kinetics of colloidal silica are not perfectly understood for conditions like those found in a deep geothermal well. With a thorough analysis of the composition of the geothermal fluid in the reservoir, it should be possible to validate the size distribution as suggested by Plyasunov (2012).

The discrete phase model FLUENT uses to track particles also suffers weaknesses, as was observed in its registration of particle deposition for larger particles. Further investigation of the method for deposition of medium sized particles is recommended as further work.

A new model for updating the surface with a deposition layer should be introduced, possibly with a transient flow method. A continuously updated surface layer will require a fairly complex simulation method, but this should be the most accurate manner of predicting continued fouling in pipe flow.

Certain factors deemed important to deposition rates in chapter 2 should be introduced:

- Surface roughness for conventional well pipes should be introduced.
- Electrostatic surface charge should be introduced as a computed sticking probability for particle-film interaction.

An improvement to the turbulence model is suggested. For the RSM model, correction for the quadratic turbulence fluctuation variation may increase accuracy, and so this is recommended for further work.

Bibliography

- Ahmadi, G. (1994). Analysis of particle motion in the near-wall shear layer vortices - application to the turbulent deposition process, *Journal of colloid and interface science*, vol 172, pp. 263-277. DOI: 10.1006/jcis.1995.1252. Fetched 16-09-2019.
- ANSYS, I. (2014). Lecture 7: Turbulence modeling. Fetched 14.10.2019.
- ANSYS ® (2019). Fluent users's guide. Available at: https://www.afs.enea.it/project/neptunius/docs/fluent/html/ug/main_pre.htm. Accessed 09-10-19.
- Ayse Altunbas, Gudret Kelbaliyev, K. C. (2002). Eddy diffusivity of particles in turbulent flow in rough channels *Journal of Aerosol Science*, vol. 7, pp. 1075-1086. DOI: [https://doi.org/10.1016/S0021-8502\(02\)00054-X](https://doi.org/10.1016/S0021-8502(02)00054-X). Fetched 27-09-2019.
- Bahadori, A. and Vuthaluru, H. B. (2009). Prediction of silica carry-over and solubility in steam of boilers using simple correlation *Applied Thermal Engineering*, vol. 30, pp 250-253. DOI: 10.1016/j.applthermaleng.2009.07.010. Fetched 01-10-2019.
- Bordvik, S. (2020). Comparative analysis of energy extraction systems for high temperature, high pressure geothermal steam considering silica precipitation, *Proceedings World Geothermal Congress 2020*. Fetched 07-12-2019.
- Bowen, B. D. and Epstein, N. (1978). Fine particle deposition in smooth parallel-plate channels *Journal of Colloid and Interface Science*, vol. 72, pp 81-97. DOI: [https://doi.org/10.1016/0021-9797\(79\)90184-X](https://doi.org/10.1016/0021-9797(79)90184-X). Fetched 08-10-2019.
- Brown, K. (2011). Thermodynamics and kinetics of silica scaling, *Proceedings International Workshop on Mineral Scaling 2011*. Available at: <https://pdfs.semanticscholar.org/68bd/0b19d3166756ebe3e3eaaebc3233a9257afe.pdf>. Fetched 06-09-19.
- Chauhan, V. (2019). Superheated steam scrubbing and utilization for power generation. Fetched 10-09-19.
- Crowe, C. T. (2006). *Multiphase Flow Handbook*. Taylor & Francis.
- Daniela B. van den Heuvel, Liane G. Benning, T. M. S. (2018). Understanding amorphous silica scaling under well-constrained conditions inside geothermal pipelines, *Geothermics* 76, pp. 231-241. DOI: 10.1016/j.geothermics.2018.07.006. Accessed 19-11-2019.
- Esptein, N. (1983). Thinking about heat transfer fouling: A 5×5 matrix *Heat Transfer Engineering*, vol. 4, pp. 43-56. DOI: <https://doi.org/10.1080/01457638108939594>. Fetched 06-12-2018.
- Fleming, B. A. (1986). Kinetics of reaction between silicic acid and amorphous silica surfaces in nacl solutions, *Journal of Colloid and Interface Science*. 1986, vol. 110, pp. pp. 40-64. Available at: [https://doi.org/10.1016/0021-9797\(86\)90351-6](https://doi.org/10.1016/0021-9797(86)90351-6). Fetched 09-09-2019.

- Franziska Greifzu, Christoph Kratzsch, T. F. F. L. R. S. (2015). Assessment of particle-tracking models for dispersed particle-laden flows implemented in openfoam and ansys fluent, *Engineering Applications of Computational Fluid Mechanics*, 10:1, 30-43. DOI:10.1080/19942060.2015.1104266. Fetched 15-09-19.
- Fridriksson, T., Stefansson, A., Oskarsson, F., Eyjolfsdottir, E., and Sigurdsson, O. (2015). Fluid chemistry scenarios anticipated for iddp-2 to be drilled in reykjanes, iceland, *Proceedings World Geothermal Congress 2015, Melbourne, Australia, 19-25*. Available at: https://www.researchgate.net/publication/303284072_Fluid_chemistry_scenarios_anticipated_for_IDDP-2_to_be_drilled_in_Reykjanes_Iceland/references. Fetched 29-10-2019.
- Gao, T. and Jelle, B. P. (2019). Thermal conductivity of amorphous silica nanoparticles. DOI: 10.1007/s11051-019-4556-8. Fetched 12-11-2019.
- Guerrero, J. (2019). A crash introduction to turbulence modeling in openfoam. Accessed 14-09-2019.
- Guha, A. (1997). A unified eulerian theory of turbulent deposition to smooth and rough surfaces, *J. Aerosol Sci.*, vol. 28, no. 8. Fetched 15-09-19.
- Guha, A. (2008). Transport and deposition of particles in turbulent and laminar flow, *The Annual Review of Fluid Mechanics*, 40:311–41. DOI:10.1146/annurev.fluid.40.111406.102220. Fetched 15-09-19.
- Helden, L., Eichhorn, R., and Bechinger, C. (2015). Direct measurement of thermophoretic forces. Available at: <https://doi.org/10.1039/C4SM02833C>. Fetched 03-09-2019.
- Hesketh, H. E. (1977). *Fine particles in gaseous media*. Ann Arbor Science. Accessed 26-11-2019.
- Hewett, J. N. and Sellier, M. (2015). Transient simulation of accumulating particle deposition on a cylinder in cross-flow, *Int. Conf. on CFD in the Minerals and process industries*. Available at: http://www.cfd.com.au/cfd_conf15/PDFs/064HEW.pdf. Fetched 24-12-2019.
- IDDP (2019). Available at: <http://iddp.is/>. Accessed 05-09-2019.
- Im, K. H. and Chung, P. M. (1983). Particulate deposition from turbulent parallel streams *AIChE Journal*, vol. 29. DOI: <https://doi.org/10.1002/aic.690290321>. Fetched 08-12-2018.
- Kallio, G. A. and Reeks, M. W. (1989). A numerical simulation of particle deposition in turbulent boundary layers *Int. J. Multiphase Flow* vol 15(3), pp. 433-446. DOI: 0301-9322/89. Fetched 08-09-2019.
- Karlsdottir, S., Ragnarsdottir, K., Thorbjornsson, I., and Einarsson, A. (2014). *On-site erosion-corrosion testing in superheated geothermal steam*. Available at: <https://www.sciencedirect.com/science/article/pii/S037565051400008X>. Fetched 03-09-2019.

- Kemia, T. H. and Landsvirkjun, S. M. (2019). Silica in superheated steam of the iddp-1 exploratory geothermal well in krafla.
- Koebel, M. and Rigacci, A. (2011). Aerogels for superinsulation: A synoptic view. DOI: 10.1007/978-1-4419-7589-8-26. Fetched 28-11-2019.
- Kokhanenko, P. (2014). *Hydrodynamics and Chemistry of Silica scale formation in Hydro-geothermal systems*. Available at: . Fetched 03-09-19.
- Liu, B. Y. and Agarwal, J. K. (1974). Experimental observation of aerosol deposition in turbulent flow, *Aerosol Science*. 1974. Vol. 5, pp. 145-155. Available at: [https://doi.org/10.1016/0021-8502\(74\)90046-9](https://doi.org/10.1016/0021-8502(74)90046-9). Fetched 14-10-2019.
- Manning, C. E. (1994). The solubility of quartz in h₂o in the lower crust and upper mantle *Geochimica et Cosmochimica Acta*, vol. 58, pp. 4831-4839. DOI: [https://doi.org/10.1016/0016-7037\(94\)90214-3](https://doi.org/10.1016/0016-7037(94)90214-3). Fetched 08-11-2019.
- Mills, A. F. (2001). *Mass Transfer*. Prentice Hall.
- Nancy Møller, J. P. G. and Weare, J. H. (1998). Computer modeling for geothermal systems: Predicting carbonate and silica scale formation, co₂ breakout and h₂s exchange, *Transport in Porous Media*, vol 33, pp. 173-204. DOI: 10.1023/A:1006501927827. Fetched 09-10-2019.
- NTNU (2019). Available at: <https://www.ntnu.edu/ept>. Accessed 05-09-2019.
- Orkustofnun (2018). <https://nea.is/geothermal/the-iceland-deep-drilling-project/>. Accessed 20-12-2019.
- Orzag, S. A. (1970). Analytical theories of turbulence, *Journal of Fluid Mechanics*, vol. 41 (2), pp. 363-386. DOI: 10.1017/S0022112070000642. Fetched 20-11-2019.
- Papavergos, P. G. and Hedley, A. B. (1984). Particle deposition behaviour from turbulent flows *Institution of Chemical Engineering*, vol 62, pp. 275-295. Printed copy available at Oria.no.
- Paulsen, V. (2018). Silica polymerization & deposition in trubulent flows, *NTNU, dept. Enegy & Process Engineering*. Fetched 05-09-19.
- Pavel Karasek, Barbora Hohnová, M. R. (2013). Solubility of fused silica in sub- and super-critical water: Estimation from a thermodynamic model, *Journal of Supercritical Fluids*, vol 83, pp. 72-77. DOI:10.1016/j.supflu.2013.08.012. Fetched 04-09-2019.
- Philibert, J. (2005). One and a half century of diffusion: Fick, einstein, before and beyond, *Journal for the Basic Principles of Diffusion Theory*. Available at: [https://web.archive.org/web/20090205030323/http://www.uni-leipzig.de/diffusion/journal/pdf/volume2/diff_fund_2\(2005\)1.pdf](https://web.archive.org/web/20090205030323/http://www.uni-leipzig.de/diffusion/journal/pdf/volume2/diff_fund_2(2005)1.pdf). Fetched 18-10-2019.

- Plyasunov, A. V. (2012). Thermodynamics of $\text{Si}(\text{OH})_4$ in the vapor phase of water: Henry's and vapor-liquid distribution constants, fugacity and cross virial coefficients *Geochimica et Cosmochimica Acta*, vol. 77, pp 215-231. DOI: 10.1016/j.gca.2011.04.016. Fetched 04-10-2019.
- Robert O. Fournier and Jack J. Rowe (1977). The solubility of amorphous silica in water at high temperatures and high pressure *American Mineralogist*, vol 62, pp. 1052-1056. Available at: http://www.minsocam.org/ammin/AM62/AM62_1052.pdf. Fetched 19-09-2019.
- S. Elghobashi (1994). On predicting particle laden turbulent flows *Applied Scientific Research*, vol 52, pp. 309-329. Fetched 24-11-2019.
- Saffman, P. (1964). The lift on a small sphere in a slow shear flow *J. Fluid Mech*, vol 22(2), pp. 385-400. https://webpace.clarkson.edu/projects/crcd/public_html/me437/downloads/1_4Lift.pdf. Accessed 29-10-2019.
- Schlichting, H. (1968). *Boundary-layer theory*. McGraw-Hill Book Co.
- Shimada, M. and Okuyama, K. (1993). Deposition of submicron aerosol particles in turbulent and transitional flow, *AIChE Journal*, vol. 39, pp. 17-36. DOI: 10.1002/aic.690390104. Fetched 24-12-2019.
- Talbot, J., Cheng, R., Schefer, R., and Willis, D. (1980). Thermophoresis of particles in a heated boundary layer *Journal of Fluid Mechanics*, vol 101(4), pp. 737-758. Available at: <https://doi.org/10.1017/S0022112080001905>. Fetched 26-09-2019.
- Tandberg, A. R. (2017). Gas-side fouling of heat exchanger surfaces.
- Temu, A. K. (1998). Experimental and theoretical study of particle deposition onto a cylinder in cross flow, *PhD. Thesis, NTNU*, pp. 27-32. Available at: https://www.begellhouse.com/ebook_platform/6a90e726486b49f2,3a3414742ec1fd7b,5a3e68721483a1e7.html?msg=access_denied. Fetched 12-01-2020.
- Tian, L. and Ahmadi, G. (2006). Particle deposition in turbulent duct flows—comparisons of different model predictions, *Journal of Aerosol Science*. DOI:10.1016/j.jaerosci.2006.12.003. Fetched 15-09-19.
- Toolbox, E. (2018). Properties of saturated steam - pressure in bar. Available at: https://www.engineeringtoolbox.com/saturated-steam-properties-d_457.html. Accessed 20-12-2019.
- U.S. Kleinhans, M. Barfersoi, S. B. C. W. H. S. (2015). The role of thermophoresis during deposit build-up on a superheater tube *Proc. of International Conference on Heat Exchanger fouling and cleaning - 2015*. Available at www.heatexchanger-fouling.com. Accessed 25-11-2019.
- Wells, A. C. and Chamberlain, A. C. (1967). Transport of small particles to vertical surfaces *British Journal of Applied Physics*, vol. 18. DOI: 10.1088/0508-3443/18/12/317.

Young, J. B. (2011). Thermophoresis of a spherical particle: Reassessment, clarification, and new analysis *Aerosol Science and Technology*, vol 45, pp. 927-948. DOI: 10.1080/02786826.2011.569777. Fetched 28-11-2019.

Zheng, X. and Silber-Li, Z. (2009). The influence of saffman lift force on nanoparticle concentration distribution near a wall *Appl. Phys. Lett.* 95. DOI: 10.1063/1.3237159. Accessed 25-11-2019.

Appendix

.1 Additional simulation results

.1.1 Velocity profile

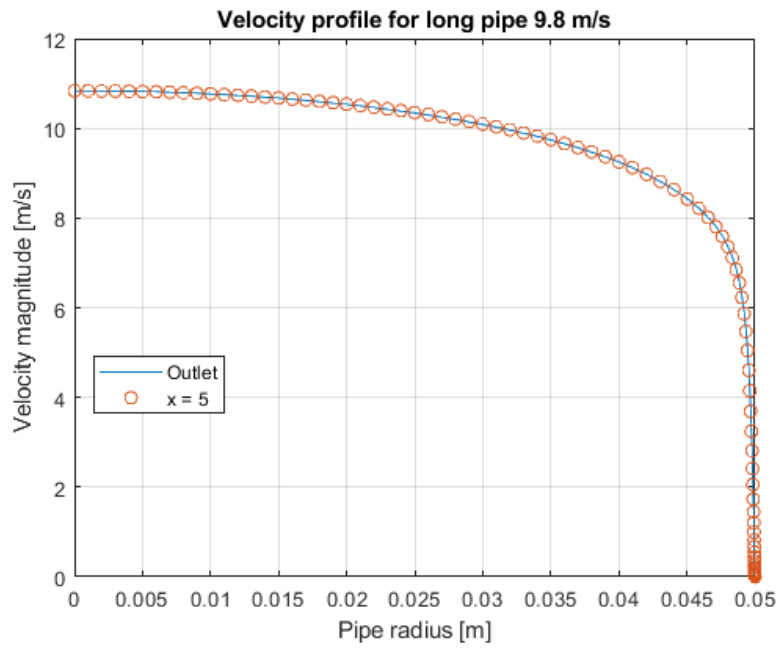


Figure 1: Velocity profile for low velocity pipe simulation

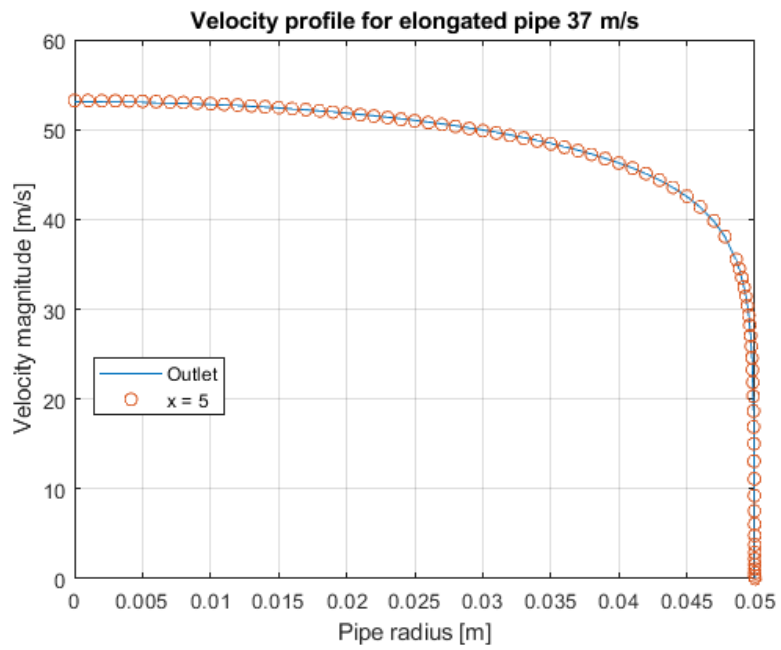


Figure 2: Velocity profile for elongated pipe simulation

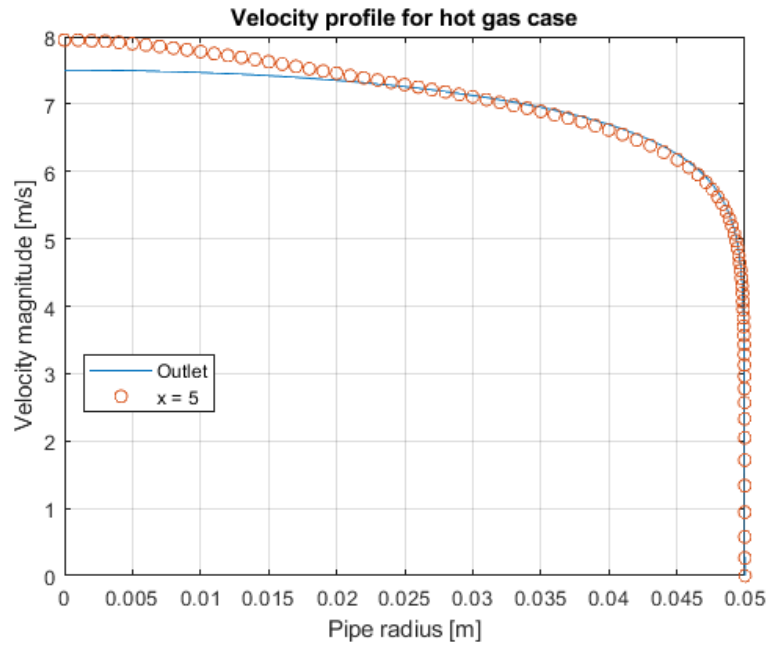


Figure 3: Velocity profile for geothermal steam simulation

.1.2 Dim. less velocity profile

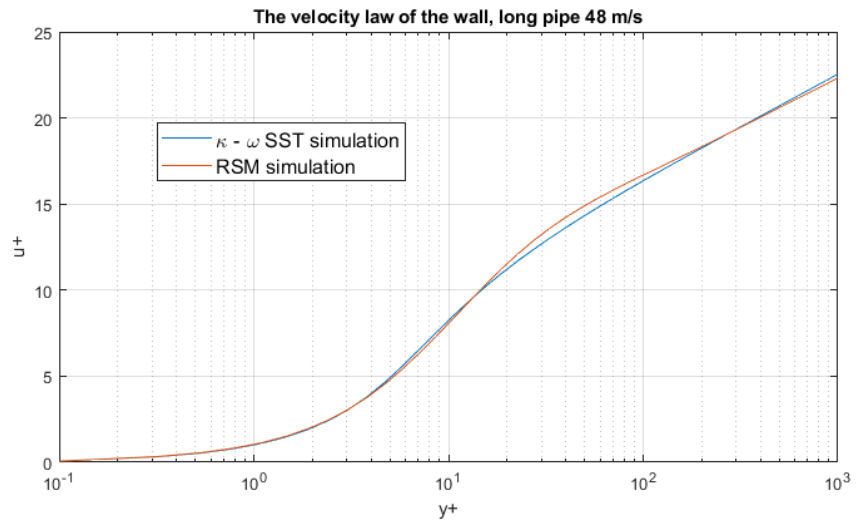


Figure 4: Dimensionless velocity profile for long pipe, high velocity simulation

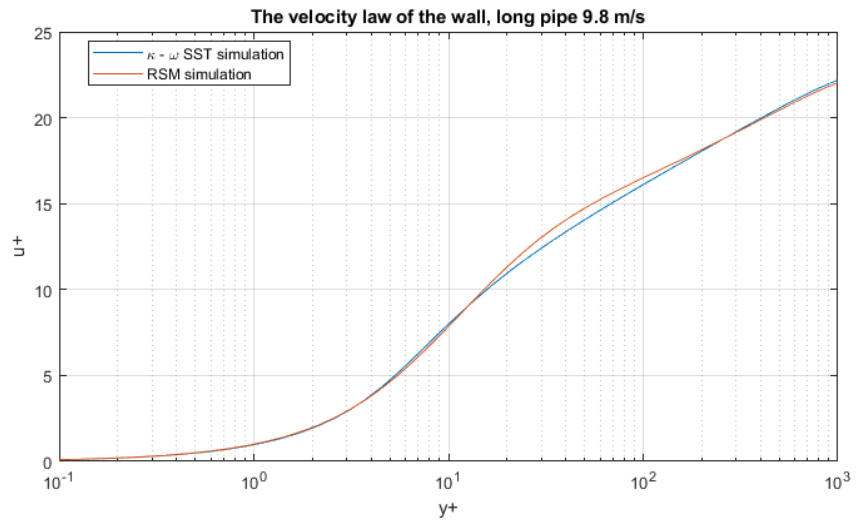


Figure 5: Dimensionless velocity profile for long pipe, low velocity simulation

.1.3 Deposition rate comparisons

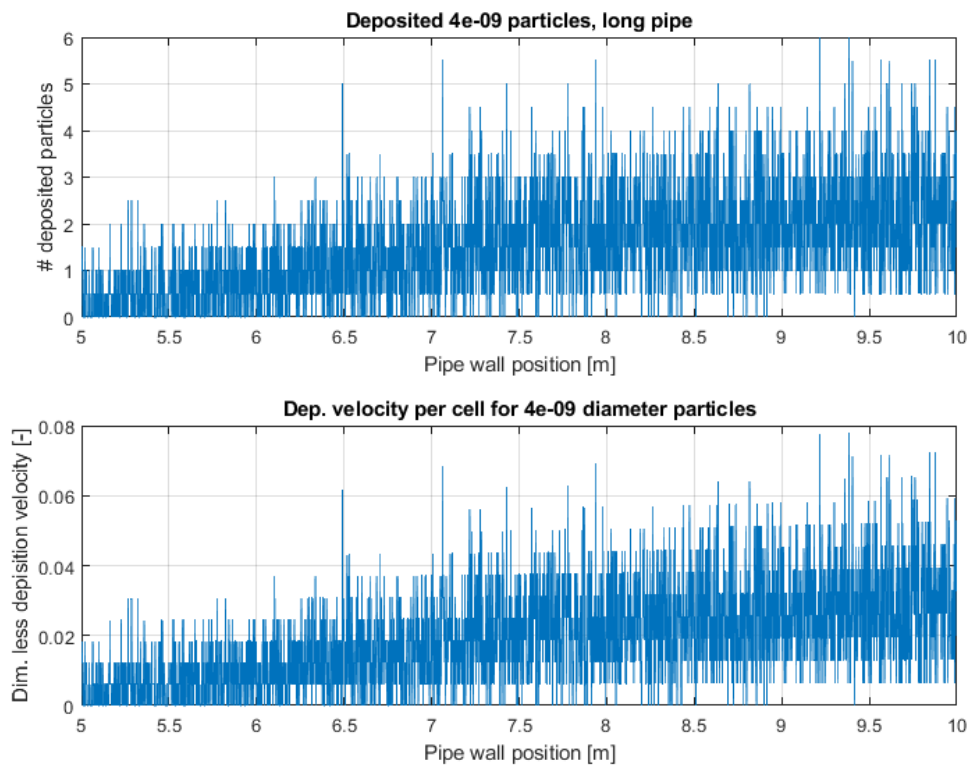


Figure 6: Deposition rate and velocity for 4 nm particles in high velocity simulation.

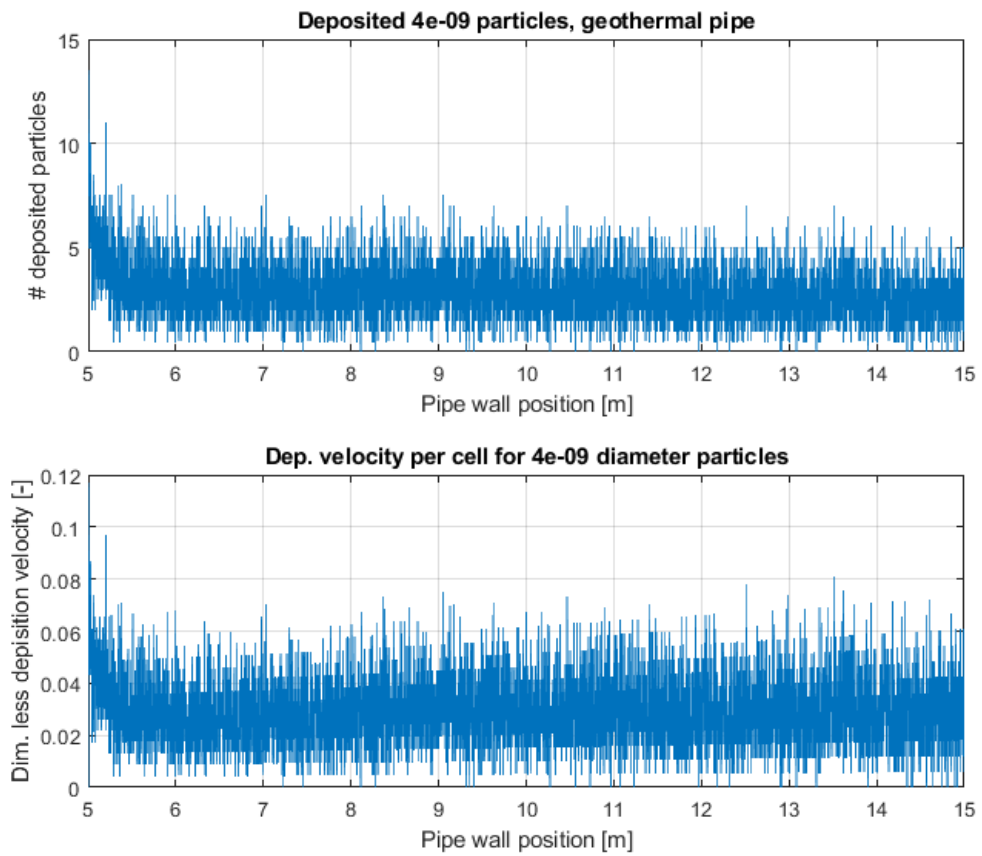


Figure 7: Deposition rate and velocity for 4 nm particles in geothermal simulation.

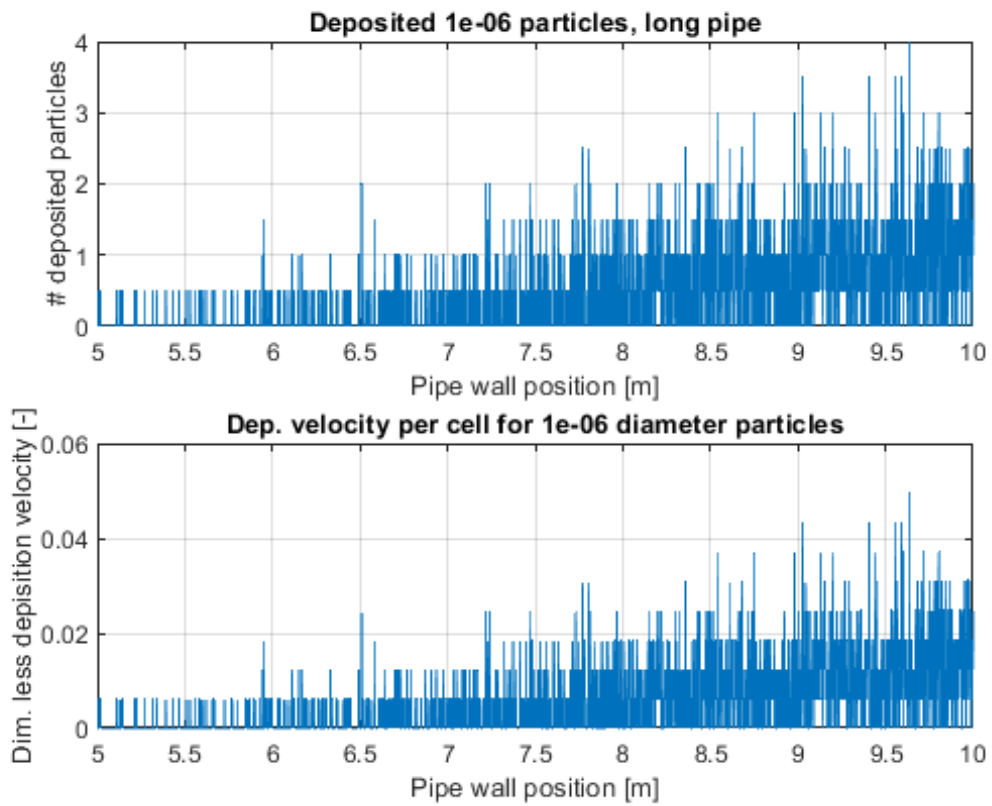


Figure 8: Deposition rate and velocity for for $1\ \mu\text{m}$ particles in high velocity simulation.

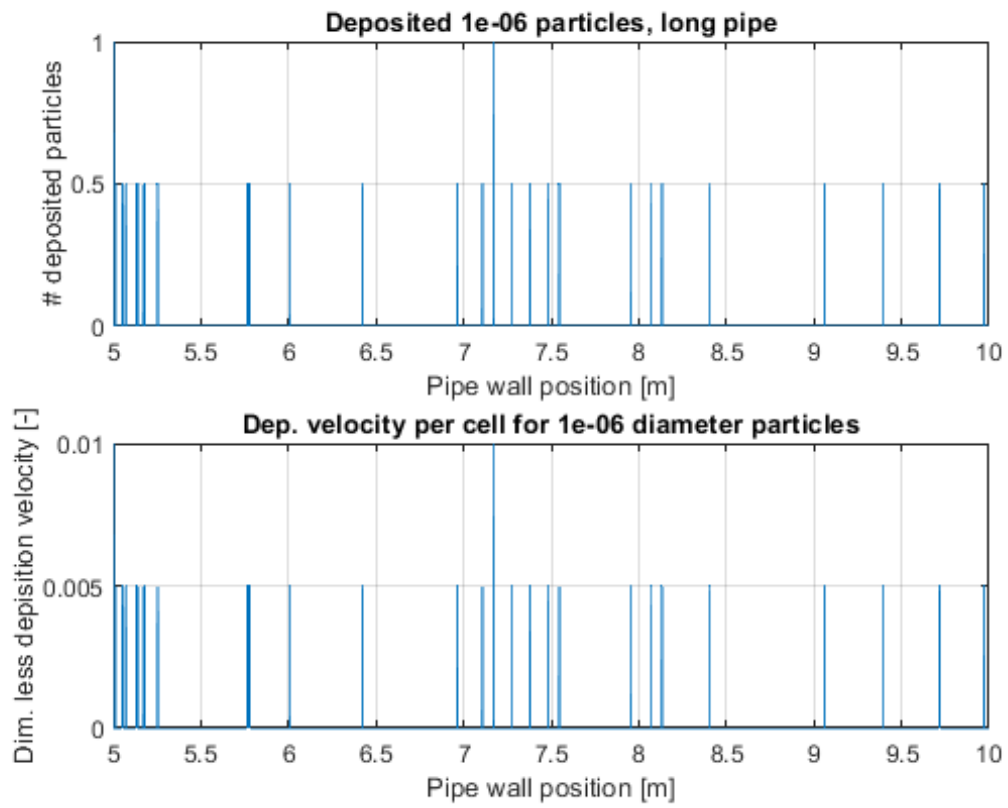


Figure 9: Deposition rate and velocity for for 1 μm particles in low velocity simulation.

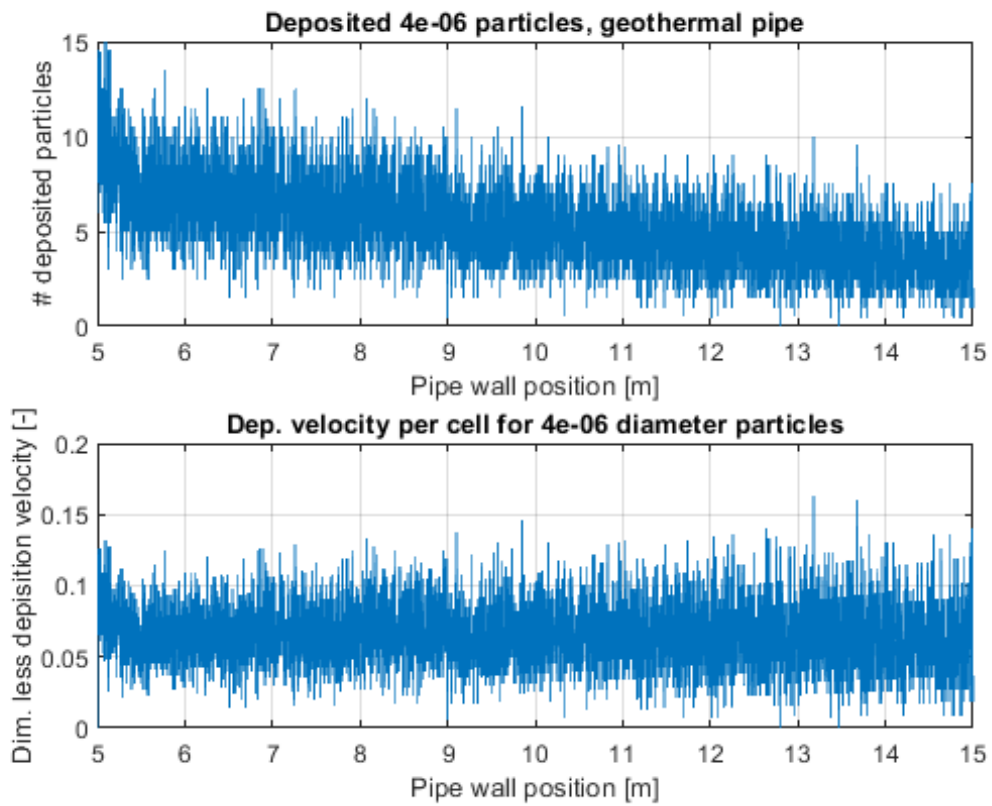


Figure 10: Deposition rate and velocity for $4\ \mu\text{m}$ particles in geothermal simulation.

.2 Matlab code

This appendix provides the Matlab files used for discretization in order to find particle deposition velocity and comparison to empirical formulae. Also provided are the computations for deciding initial wall distance of mesh cells, and measuring the dimensionless velocity profile close to wall.

Table of Contents

Estimation of first cell distance to wall	1
Computation of deposition velocity	1
Plotting deposition velocity	3
Integration of deposition rate along pipe wall	5
Dimensionless velocity profile	6

Estimation of first cell distance to wall

The wall cell distance is crucial for accurate predictions of the RSM method in simulation of turbulent flow, so the distance is estimated using suggested formulas of ANSYS Fluent

```
% Pipe dimensions and fluid properties are first determined.
prompt = 'Enter fluid density (kg/m^3): ' ;
rho_f = input(prompt);

prompt = 'Enter dynamic viscosity (m^2/s): ' ;
mu = input(prompt);

prompt = 'Enter velocity (m/s): ' ;
U = input(prompt);

prompt = 'Enter pipe length (m): ' ;
L = input(prompt);

prompt = 'Enter pipe diameter (m): ' ;
d = input(prompt);

Re_p = rho_f * U * d / mu;
% Re_p = rho * U * L / mu;

Cf = 0.079 * Re_f^(-0.25);
tau_w = 0.5 * Cf * rho_f * U^2;
U_tau = sqrt(tau_w/rho_f);

% Choice of y_plus is made on recommendation by ANSYS. For RSM method,
% y_plus should not be higher than 1
prompt = 'Select y_plus from 1 to 200: ' ;
y_plus = input(prompt);

y = (mu * y_plus)/(rho_f * U_tau);

Y = sprintf('Cell distance should be %d meters away from the
wall.',y);
disp(Y)
```

Computation of deposition velocity

The dimensionless deposition velocity is computed based on number of inlet particles and total registered outlet particles. The relaxation time is set manually and is used to plot the deposition velocity later on.

```

% clear all
close all
% clc

% Fluid properties and pipe dimensions

M = 28.97; % Molecular weight of air [kg/kmol]
rho_f = 1.16; % fluid density [kg/m^3]
% rho_p = 3750; % aluminium oxide density
rho_p = 2000; % silica colloid density
nu = 1.589*10^-5; % Kinematic visc(v)
mu = nu * rho_f; % Dynamic visc (u)
R = 8314; % Universal gas constant [J/kmolK]
x = 5; % Dynamic shape factor
T = 373; % Fluid temp [Kelvin]
g = 0;

d = 0.1; % Channel diameter / height [metre]
L = 10; % Length of pipe [m]
dx = 5; % Length in which particles travel (minus the initial meter)
S = rho_p/rho_f; % Particle-fluid-ratio

% u = 5; % Avg. velocity, Tandberg
u = 48.0701; % Avg velocity 50 m/s inlet sim
% u = 9.8015; % Avg velocity 10 m/s inlet sim

% Particle diameter
d_p = 5*10^-8; % Particle diameter [metre]
d_p_micro = d_p * 10^6; % Particle diameter [micrometre]

% Development of particle relaxation time

Re_f = (rho_f * u * d)/(mu); % Reynolds number
l = nu * ((pi*M)/(2*R*T))^0.5; % Mean free path
% l = 0.0664 * 10^-6 * (101/101)*(373/293)*((1+(110)/(293))/(1+(110)/(373))); % Crowe
Kn = l ./ d_p; % Knudsen number
Cc = 1 + Kn.*(2.514 + 0.8 .* exp(-0.55./Kn)); % Cunningham slip
correction factor
% Cc = 1 + Kn.*(2.34 + 1.05 .* exp(-0.39./Kn)); % Tandberg, uses
0.5*Kn
Cd = (24/Re_f) * (1+0.15*Re_f^0.687); % Drag coefficient
f = (3*pi*mu.*d_p.*x)./(Cc); % Friction coefficient
k = 1.38054 * 10^-23; % Boltzmann constant
D_b = (k*T*Cc)./(3*pi*mu.*d_p); % Stokes-Einstein equation diffusion
coeff.

g_plus = g*nu/(u_fric^3); % Dimensionless gravitational acceleration
L_1_plus = 3.08*rho_f./(rho_p.*d_p_plus); % Dim. less constant of
Ahmadi
k_plus = 0; % Surface roughness, 0 for smooth surface

```

```

% Cf = 0.0791 * Re_f^(-0.25);
Cf = 2 * (2.236*log(Re_f) - 4.639)^(-2); % friction factor
tau_w = Cf * 0.5 * rho_f * u^2; % Wall shear stress
u_fric = sqrt(tau_w / rho_f); % Friction velocity
d_p_plus = d_p .* u_fric/mu; % Dimensionless particle diameter

tau_p = (rho_p * d_p^2) / (18*mu); % Particle inertia relaxation time
tau_p = tau_p * Cc; % Accounting for rarefied gas effects
tau_plus = tau_p * u_fric^2 / nu % Dimensionless particle relaxation
time

% Computation of dimensionless deposition velocity

Ninn = 100000; % Particles at inlet
Nout = 100000-611; % Particles at outlet

v_dpp = (d*u)/(2*u_fric*dx) * log(Ninn/Nout) % Dim. less deposition
vel.

```

Plotting deposition velocity

The following script is fed the deposition velocities extracted from FLUENT and computed by the previous script. The deposition velocities are plotted over a parameter of particle relaxation times set by the fluid flow properties and particle sizes. Lastly, the empirical formulae of Papavergos & Hadley (1984) and Ahmadi (1994) are computed for the same particle size range and compared.

```

d_p = linspace(4*10^-9,2.5*10^-5,1000000); % Particle diameter [m]
parameter

% Papavergos & Hadley (1984)

Vd_p = zeros(1,length(tau_p_plus));

for i = 1:length(tau_p_plus)

    j = tau_p_plus(i);

    if j < 0.2
        Vd_p(i) = 0.065*(Sc_p(i))^-2/3);
    elseif 0.2 < j && j <= 20.0
        Vd_p(i) = 3.5 * 10^-4 * j^2;
    elseif j > 20
        Vd_p(i) = 0.18;
    end
end

% Ahmadi (1994)
Vd_p_a = zeros(1,length(tau_p_plus));

```

```

for i = 1:length(tau_p_plus)

    j = tau_p_plus(i);

    if i == 1

        a = 0.084 * Sc_p(i)^(-2/3);
        b = ((0.64*k_plus+0.5*d_p_plus(i))^2 ...
            + (tau_p_plus(i)^2*g_plus*L_1_plus(i))/(0.01085*...
            (1+tau_p_plus(i)^2*L_1_plus(i))))/
        (3.42+((tau_p_plus(i)^2*...
            g_plus*L_1_plus(i))/
        (0.01085*(1+tau_p_plus(i)^2*L_1_plus(i)))));
        c = (1/(1+tau_p_plus(i)^2*L_1_plus(i)));
        e = (1+8*exp(-(tau_p_plus(i)-10)^2/(32)));
        f = (0.037)/(1-tau_p_plus(i)^2*L_1_plus(i)*(1+(g_plus)/
        (0.037)));

        Vd_p_a(i) = a + 0.5*b^c * e * f;

    elseif Vd_p_a(i-1) < 0.14

        a = 0.084 * Sc_p(i)^(-2/3);
        b = ((0.64*k_plus+0.5*d_p_plus(i))^2 ...
            + (tau_p_plus(i)^2*g_plus*L_1_plus(i))/(0.01085*...
            (1+tau_p_plus(i)^2*L_1_plus(i))))/
        (3.42+((tau_p_plus(i)^2*...
            g_plus*L_1_plus(i))/
        (0.01085*(1+tau_p_plus(i)^2*L_1_plus(i)))));
        c = (1/(1+tau_p_plus(i)^2*L_1_plus(i)));
        e = (1+8*exp(-(tau_p_plus(i)-10)^2/(32)));
        f = (0.037)/(1-tau_p_plus(i)^2*L_1_plus(i)*(1+(g_plus)/
        (0.037)));

        Vd_p_a(i) = a + 0.5*b^c * e * f;

    else
        Vd_p_a(i) = 0.14;
    end
end

% Dim. less relaxation times and deposition velocities computed from
% results provided by FLUENT DPM for listed particle sizes.

d_p_match_sst = [4e-9, 6e-9, 2.6e-8, 8e-8, 2e-7, 6e-7, 8e-7, 1e-6,...
    2e-6, 3e-6, 6e-6, 3e-5];
tau_p_match_sst = [0.0012, 0.0018, 0.0084, 0.0304, 0.1067, 0.6681,...
    1.1271, 1.7045, 6.3656, 13.9833, 54.5758, 1000];
v_d_p_match_sst = [0.0099, 0.0095, 0.0091, 0.0093, 0.0078, 0.0048,...
    0.0045, 0.0051, 0.0298, 0.2150, 0.2005, 0.1940];

```

```

v_d_p_rsm = [0.0190, 0.0185, 0.0184, 0.0185, 0.0180, 0.0140,
0.0139,...
0.0152, 0.0292, 0.1392, 0.1774, 0.1855];

% Dim. less deposition velocity plotted against dim. less relaxation
time
figure(1)
loglog(tau_p_plus, Vd_p, '-', tau_p_plus, Vd_p_a, '-',
tau_p_match_sst,...
v_d_p_match_sst, 'go', tau_p_match_sst, v_d_p_rsm, 'ro')
grid on
xlabel('Dim. less relaxation rate')
ylabel('Dim. less deposition velocity')
title('Dim. less deposition velocity for a 10 m pipe at 48 m/s')
legend('Papavergos & Hedley (1984)', 'Ahmadi (1993)', ...
'k-\omega SST simulation', 'RSM simulation', 'location', 'best')
axis([10^-3 10^3 10^-5 10^0])

% Plot of Cunningham slip correction factor
figure(2)
loglog(d_p, Cc)
grid on
title('Rarefied gas effect by particle size, 48 m/s')
xlabel('Particle diameter')
ylabel('Cunningham correction slip factor')

% Plot of particle Schmidt number
figure(3)
loglog(d_p, Sc_p)
grid on
title('Schmidt number by particle size, 48 m/s')
xlabel('Particle diameter')
ylabel('Particle schmidt number')

```

Integration of deposition rate along pipe wall

Having recieved deposition rates from MATLAB using the UDF in FLUENT, the deposited particles are plotted against pipe length to reveal the concentration of deposited particles. The deposition rates are then integrated across each cell, revealing the deposition velocity of all cells.

```

figure(4)

subplot(1,2,1)
plot(pipe_length, deposited)
grid on
xlabel('Pipe wall position [m]')
ylabel('# deposited particles')
title(['Deposited ', num2str(d_p), ' particles, long pipe'])

Ninn = 100000; % Particles at inlet

for i = 1:length(pipe_length)

```

```

    if i == 1

        Nout = Ninn - deposited(i);
        v_dep_p(i) = (d*u)/(2*u_fric*pipe_length(i)) * log(Ninn/Nout);
        Ninn = Nout;

    elseif pipe_length(i) == pipe_length(i-1)

        v_dep_p(i) = v_dep_p(i-1);

    else

        Nout = Ninn - deposited(i);
        v_dep_p(i) = (d*u)/(2*u_fric*(pipe_length(i)-
pipe_length(i-1))) * log(Ninn/Nout);
        Ninn = Nout;

    end

end

% The integration of dep. velocit over all cells should provide an
average
% deposition velocity equal to that computed in previous script.

correlation = sum(v_dep_p)/(length(pipe_length)); % Check result

plot(pipe_length, v_dep_p)
grid on
xlabel('pipe length [m]')
ylabel('Dim. less deposition velocity [-]')
title(['Dep. velocity per cell for ', num2str(d_p), ' diameter
particles'])

```

Dimensionless velocity profile

Dimensionless velocity profile is plotted close to wall to evaluate the different turbulence models.

```

% The wall shear stress is retrieved at the beginning of deposition
region
% tau_w = 0.27; % wall shear stress for long pipe vel 9.8 RSM (0.26
SST)
tau_w_sst = 4.63; % long pipe wel 48 SST
tau_w_rsm = 4.8; % long pipe wel 48 RSM

% Friction velocities are computed
u_fric_sst = sqrt(tau_w_sst / rho_f);
u_fric_rsm = sqrt(tau_w_rsm / rho_f);

% The number of cells from the wall to  $y^+ = 10^3$  are measured, with
the
% data provided for by FLUENT results.

```

```

for i = 1:length(wall_distance_)

    if i == 1

        y(i) = wall_distance_(i);
        y_plus_sst(i) = (u_fric_sst * y(i)) / nu;
        y_plus_rsm(i) = (u_fric_rsm * y(i)) / nu;

        elseif y_plus_sst(i-1) < 10^3 % Not necessary to measure for hiher
val.

            y(i) = wall_distance_(i);
            y_plus_sst(i) = (u_fric_sst * y(i)) / nu;
            y_plus_rsm(i) = (u_fric_rsm * y(i)) / nu;

        else
            % Velocity is fetched for the measured cells.
            u_plus_rsm = vel_rsm(1:i-1)./u_fric_rsm;
            u_plus_sst = vel_sst(1:i-1)./u_fric_sst;

            break

        end

    end

end

figure(4)
% plot(y_plus, u_plus_sst, y_plus, u_plus_rsm)
semilogx(y_plus_sst, u_plus_sst, y_plus_sst, u_plus_rsm)
axis([10^-1 10^3 0 25])
grid on
title('The velocity law of the wall, long pipe 48 m/s')
xlabel('y+')
ylabel('u+')
legend('\kappa - \omega SST simulation', 'RSM
simulation', 'location', 'best')

```

Published with MATLAB® R2018a

.3 C code / FLUENT macros

The provided codes were utilized either in flow simulations as initial values for desired parameters, or in stochastic particle tracking.

Table of Contents

Initial values	1
Capture boundary condition	4
UDM reset	4
Brownian force	5
Initial particles	6

Initial values

The following code shows five different udfs for inlet velocity, temperature, turbulent kinematic energy, turbulent dissipation and turbulent diffusion.

```
#include "udf.h"

DEFINE_PROFILE(inlet_vel_10, thread, position)
{
    real p[ND_ND]; /* this will hold the position vector */
    real y, w;
    face_t f;

    w = 0.1; /* inlet width in m */

    begin_f_loop(f,thread)
    {
        F_CENTROID(p, f, thread);
        y = p[1]; /* coordinate, here p[one] means y-position, as in
0,1,2...
is x,y,z */

        F_PROFILE(f, thread, position) = (8. * 10. / 7.) * pow(((0.5 * w - ...
y) / (0.5 * w)), 1. / 7.);
    }
    end_f_loop(f, thread)
}

#include "udf.h"

DEFINE_PROFILE(inlet_x_e, thread, position)
{
    real p[ND_ND]; /* this will hold the position vector */
    real y, w, cl, a, re, lu, le, vt, mu, k, o;
    face_t f;

    w = 0.1; /* inlet width in m */
    mu = 1.84324 * pow(10., -5.); /* dynamic viscosity */
```

```

begin_f_loop(f,thread)
{
    F_CENTROID(p, f, thread);
y = p[1] - 0.5 * w; /* non-dimensional x coordinate */

k = 0.002*pow(5.,2.)-(y/(0.5*w))*0.04913523734);
cl = k * pow(0.09,-3./4.);
a = 2.*cl;
re = (1.16*y*sqrt(k))/mu;
le = y * cl * (1-exp(-re/a));
    lu = y * cl * (1-exp(-re/70.));
vt = 0.09 * lu * sqrt(k);
    o = k/vt;

F_PROFILE(f, thread, position) = pow(k,3./2.)/le;
}
end_f_loop(f, thread)
}

/* k_profile_test*/

#include "udf.h"

DEFINE_PROFILE(inlet_x_k, thread, position)
{

    real p[ND_ND]; /* this will hold the position vector */
    real y, w, m, r, d;
    face_t f;

    w = 0.1; /* inlet width in m */
    m = 1.84324 * pow(10., -5.); /* dynamic viscosity */
    r = 1.16; /* fluid density */
    d = 16.32654493;

    begin_f_loop(f,thread)
    {
        F_CENTROID(p, f, thread);
y = p[1]; /* non-dimensional x coordinate */

F_PROFILE(f, thread, position) = 0.002*pow(5.,2.)-(y/(0.5*w))*...
    0.04913523734;
    }
    end_f_loop(f, thread)
}

#include "udf.h"

DEFINE_PROFILE(inlet_x_o, thread, position)
{

    real p[ND_ND]; /* this will hold the position vector */
    real y, w, cl, a, re, lu, le, vt, mu, k, e;
    face_t f;

```

```

w = 0.1; /* inlet width in m */
mu = 1.84324 * pow(10., -5.); /* dynamic viscosity */

begin_f_loop(f,thread)
{
    F_CENTROID(p, f, thread);
y = p[1] - 0.5 * w; /* non-dimensional x coordinate */

k = 0.002*pow(5.,2.)-((y/(0.5*w))*0.04913523734);
cl = k * pow(0.09,-3./4.);
a = 2.*cl;
re = (1.16*y*sqrt(k))/mu;
le = y * cl * (1-exp(-re/a));
    lu = y * cl * (1-exp(-re/70.));
vt = 0.09 * lu * sqrt(k);
    e = pow(k,3./2.)/le;

F_PROFILE(f, thread, position) = k / vt;

}
end_f_loop(f, thread)
}

/* Tandberg temperature profile*/

#include "udf.h"

DEFINE_PROFILE(inlet_x_temperature, thread, position)
{

real p[ND_ND]; /* this will hold the position vector */
real y, w;
face_t f;

w = 0.1; /* inlet width in m */

begin_f_loop(f, thread)
{
    F_CENTROID(p, f, thread);
y = p[1]; /* non-dimensional x coordinate, here x[one] means...
            y-position, as in 0,1,2 is x,y,z */

F_PROFILE(f, thread, position) = (8. * (100 - 50) / 7.) *...
    pow(((0.5 * w - y) / (0.5 * w)), 1. / 7.) + 323.;
/*Message("hei, a= %f", 0.002 * (8. * (100 - 50) / 7.) *...
    pow(((0.5 * w - y) / (0.5 * w)), 1. / 7.) + 323.);*/

}
end_f_loop(f, thread)
}

```

Capture boundary condition

The UDF introduces a memory variable for storing detected trapped particles onto wall cells along the chosen boundary.

```
/* Capture boundary condition for DPM with UDM location*/

#include "udf.h"
#include "mem.h"
#define NUM_UDM 1; /* number of UDMs */
DEFINE_DPM_BC(bc_capture, p, t, f, f_normal, dim)
{
    int hit=0;
    if (p->type==DPM_TYPE_INERT)
    {
        if (((NNLLP(t)) && (THREAD_TYPE(t) == THREAD_F_WALL)))
        {
            Thread * tread_cell=P_CELL_THREAD(p);
            cell_t c=P_CELL(p);
            C_UDMI(c,tread_cell,0) += 1.0;

            return PATH_ABORT;
        }
    }
}
```

UDM reset

This UDF resets data stored in the user defined memory location when activated.

```
#include "udf.h"
#include "mem.h"
#define NUM_UDM 1; /* number of UDMs*/

DEFINE_ON_DEMAND(udm_reset)
{
    int i = 0;
    Domain *d;
    Thread *t;
    cell_t c;

    d=Get_Domain(1);

    Message("Setting all UDM on the domain equal to zero\n");

    thread_loop_c(t,d) /* Loop over all threads in the domain*/
    {
        /*Loop over all cells in the thread*/
        begin_c_loop(c,t)
        {
            C_UDMI(c,t,i) = 0.0;
        }
    }
}
```

```

        end_c_loop(c,t)
    }
    Message("All UDM are reset. DONE\n");
}

```

Brownian force

The following code computes a body force representing brownian diffusion on particles as an extension of the discrete phase model (DPM).

```

#include "udf.h"
#include "mem.h"
#include "dpm.h"
#include "surf.h"
#include "random.h"
#define Kb 1.38e-23 /*Stephan-Boltzmann constant*/
#define pi 3.1415926

DEFINE_DPM_BODY_FORCE(brownian_force, p , i)
{
    real T,Dp,labda,Cd,P,Cc,a,b,d,labda_ref;
    real z,mu_f,rho_f,rho_p,p_dt,ABS_U_V,Re,ueff,udiff,F;
    cell_t c=P_CELL(p);
    Thread *t=P_CELL_THREAD(p);

    /* Extract needed variables from Fluent*/
    labda_ref=0.0664*pow(10.0,-6.0);
    T=C_T(c,t);
    P=C_P(c,t);
    Dp=P_DIAM(p);
    mu_f=C_MU_L(c,t);
    rho_f = C_R(c,t);
    rho_p=P_RHO(p);
    p_dt=P_DT(p);

    ABS_U_V = sqrt(pow(C_U(c,t)-P_VEL(p)[0],2)+pow(C_V(c,t)-...
    P_VEL(p)[1],2)+pow(C_W(c,t)-P_VEL(p)[3],2));

    /* |U-V|, changed [] for x and y */

    Re = rho_f*Dp*ABS_U_V/mu_f;

    a=(101.0e3)/(P+101.0e3);
    b=T/293.0;
    d=(1.0+110.0/293.0)/(1.0+110.0/T);
    labda=labda_ref*a*b*d;
    Cc=1.0+labda/Dp*(2.34+1.05*exp(-0.39*Dp/labda));

    /*Shiller and Neumann correlation from Crowe et al. 2012*/

    Cd=24.0/(Cc*Re)*(1.0+0.15*pow(Re,0.687));

```

```

    /* Implementation of Brownian diffusion model */

    z = cheap_gauss_random(); /* generates random number*/

    a = 2.0*Kb*T*Cc;
    b = 3.0*mu_f*pi*Dp*p_dt;
    ueff = sqrt(a/b);
    udiff = z*ueff;

    a = 3.0*Cd*rho_f*ABS_U_V*udiff;
    b = 4*Dp*rho_p*Cc;
    F = a/b;

    return(F); /* Return variable into DPM model*/
}

```

Initial particles

This UDF imparts the particles injected with DPM with the velocity vectors equal to that of the fluid at which cell the particles are injected from.

```

#include "udf.h"
#include "surf.h"
#include "mem.h"

DEFINE_DPM_INJECTION_INIT(init_particles, I)
{
    Particle *p;
    loop (p,I->p)
    {
        cell_t c=P_CELL(p);
        Thread *t=P_CELL_THREAD(p);
        P_VEL(p)[0]=C_U(c,t); /* Velocity in x direction [0]*/
        P_VEL(p)[1]=C_V(c,t); /* Vel. in y dir. */
        P_VEL(p)[2]=C_W(c,t); /* Vel. in z dir. */
    }
}

```

Published with MATLAB® R2018a